

*IN-32*  
*368350*

# **AN ACOUSTIC CHARGE TRANSPORT IMAGER FOR HIGH DEFINITION TELEVISION APPLICATIONS**

**NASA Grant #NAGW-2753**

**W.D. Hunt and K.F. Brennan  
School of Electrical and Computer Engineering**

**and**

**C.J. Summers  
Georgia Tech Research Institute**

**Georgia Institute of Technology  
Atlanta, Georgia 30332-0250**

**Annual Report for FY 1996**



## SUMMARY

This thesis addresses the acoustoelectric issues concerning the amplification of surface acoustic waves (SAWs) and the reflection of SAWs from slanted reflector gratings on GaAs, with application to a novel acoustic charge transport (ACT) device architecture. First a simple model of the SAWAMP was developed, which was subsequently used to define the epitaxially grown material structure necessary to provide simultaneously high resistance and high electron mobility. In addition, a segmented SAWAMP structure was explored with line widths on the order of an acoustic wavelength. This resulted in the demonstration of SAWAMPS with an order of magnitude less voltage and power requirements than previously reported devices. A two-dimensional model was developed to explain the performance of devices with charge confinement layers less than 0.5  $\mu\text{m}$ , which was experimentally verified. This model was extended to predict a greatly increased gain from the addition of a ZnO overlay. These overlays were experimentally attempted, but no working devices were reported due to process incompatibilities. In addition to the SAWAMP research, the reflection of SAWs from slanted gratings on GaAs was also studied and experimentally determined reflection coefficients for both  $45^\circ$  grooves and Al stripes on GaAs have been reported for the first time. The SAWAMP and reflector gratings were combined to investigate the integrated ring oscillator for application to the proposed ACT device and design parameters for this device have been provided.



# **LOW-VOLTAGE SAW AMPLIFIERS ON MULTILAYER GaAs / ZnO SUBSTRATES**

A THESIS

Presented to

The Faculty of the Division of Graduate Studies

By

Thomas P. Cameron

In Partial Fulfillment

of the Requirements for the Degree

Doctor of Philosophy in Electrical Engineering

Georgia Institute of Technology

May 1996



# **LOW-VOLTAGE SAW AMPLIFIERS ON MULTILAYER GaAs / ZnO SUBSTRATES**

Approved:

---

William D. Hunt

---

Kevin F. Brennan

---

David R. Hertling

Date Approved \_\_\_\_\_





## ACKNOWLEDGMENT

This thesis would not have been possible without the support of many people. I wish first to express my appreciation to Robert Bloedon and Deborah Stokes, formerly of External Research at Bell-Northern Research (BNR) for instigating this career move. I would also express my deep appreciation to Dr. Al Javed for supporting my pursuit of my doctorate and my long time friend and colleague Dr. John Saw for support along the way.

I am grateful to my advisor Dr. William Hunt for his encouragement and friendship and Dr. Kevin Brennan, Dr. David Hertling and Dr. Gary May for serving on my committee as I progressed through the stages of my degree at Georgia Tech. I am also indebted to Dr. Rudy Benz and Dr. Bob Bicknell-Tassius of GTRI for advice on materials and processing, to Mike "Torch" Woodberry for teaching me everything I know about semiconductor fabrication and to Stan Halpern of GTRI for packaging my devices. I would express appreciation to my colleagues, Dr. Steve Kenney, Dr. Mike Sleva, Houston Irby and Bolaji Olutade for their friendship and technical discussions during my stay at Georgia Tech.

Finally I express my deep gratitude to my wife Mary Lou and children Thomas, Alicia and Amanda for their patience, understanding and love throughout our stay in Georgia.



## **TABLE OF CONTENTS**

<b>ACKNOWLEDGEMENTS</b>	<b>iii</b>
<b>LIST OF FIGURES</b>	<b>vii</b>
<b>LIST OF TABLES</b>	<b>xii</b>
<b>SUMMARY</b>	<b>xiii</b>
<b>1. INTRODUCTION</b>	<b>1</b>
Objectives	1
<b>2. BACKGROUND</b>	<b>7</b>
Origin and History	7
SAWAMP Device Description	7
Theory of Operation	9
<b>3. MATERIAL STRUCTURE</b>	<b>19</b>
History	19
Multilayer GaAs Material Structure	22
<b>4. SEGMENTED SAWAMP STRUCTURE</b>	<b>31</b>
Background	33
SAWAMP Testing	37
Test Structure	37
Test Setup	37
Reflections in Ohmic Grating	39
Experimental Gain Measurements	43
SAWAMP Gain Measured for Devices on Thick Layers	43



SAWAMP Gain Measured for Devices on Thin Layers	46
Two-Dimensional Analysis of a Segmented SAWAMP	48
Electric Field Formulation	50
SAW Potential Profile	53
Gain Formulation	55
Comparison to Experiment	57
Power Reduction Techniques	69
Addition of a Piezoelectrically Active Layer	72
Segmented SAWAMP Summary	83
<b>5. SLANTED REFLECTION GRATINGS ON GaAs</b>	<b>85</b>
Theory of Slanted Reflectors	86
Experimental Determination of the Impedance Mismatch from Stripes and Grooves on GaAs	92
Test Structure	92
Experimental Measurements of the Grating Reflection Coefficient for Al Stripes	94
Multiple Reflections	99
Calculation of the First Order Mechanical Reflection Coefficient for Al Stripes	100
Calculation of the First Order Mechanical Reflection Coefficient for Grooves	105
Summary of Grating Measurements	110
<b>6. INVESTIGATION OF THE INTEGRATED SAW OSCILLATOR</b>	<b>112</b>
Investigation of the Loop Delay Line	113
Experimental Characterization of the Loop	113
Integration of the SAWAMP into the Loop	121
Ring Oscillator Performance Prediction with a ZnO Overlay	127
Summary	128
<b>7. SUMMARY AND CONCLUSIONS</b>	<b>131</b>
Summary of Results	131



## Recommended Future Work

134

**REFERENCES****136**





## LIST OF FIGURES

Figure		Page
1.1	Conventional ACT device and ACT device with on-chip clock created by amplifier-reflector loop.	5
2.1	Schematic illustration of a SAW amplifier.	8
2.2	Transmission line models of acoustic propagation (a) on a piezoelectric and (b) on a piezoelectric/semiconductor composite.	11
2.3	Gain per wavelength versus free carrier concentration for a 1000 Å layer of n-type GaAs with no applied voltage.	13
2.4	SAW velocity versus free carrier concentration for a 1000 Å layer of n-type GaAs with no applied voltage.	15
2.5	Gain versus applied drift field for a 1000 Å layer of n-type GaAs with a free carrier concentration of $1 \times 10^{14} \text{ cm}^{-3}$	17
3.1	SAW Amplifier structures: (a) piezoelectric semiconductor, (b) separated medium, (c,d) monolithic mediums.	21
3.2	Gain curves for a 1 cm long SAWAMP on a 1000 Å layer of GaAs with the following free carrier concentrations: $1 \times 10^{13} \text{ cm}^{-3}$ (—), $5 \times 10^{13} \text{ cm}^{-3}$ (--), $1 \times 10^{14} \text{ cm}^{-3}$ (ooo), $5 \times 10^{14} \text{ cm}^{-3}$ (++) .	24
3.3	Free carrier density profile for a 1.1 μm layer of GaAs doped at $5 \times 10^{15} \text{ cm}^{-3}$ on semi-insulating GaAs.	26
3.4	Free carrier density profile for a 0.45 μm layer of GaAs doped at $5 \times 10^{15} \text{ cm}^{-3}$ on semi-insulating GaAs.	27



3.5	Experimental sheet resistance compared to theoretical predictions using HETMOD (—) assuming no interface depletion, (----) assuming 0.5 $\mu\text{m}$ of interface depletion.	29
4.1	Operation of a segmented amplifier structure.	32
4.2	Gain curves for a segmented SAWAMP on a 3500 Å layer of GaAs doped at $1 \times 10^{14} \text{ cm}^{-3}$ with $L_1 = 50 \mu\text{m}$ , $L_2 = 10 \mu\text{m}$ and $N = 100$ .	34
4.3	Amplifier test schematic.	36
4.4	Frequency responses of (a) Two IDTs, (b) $\lambda/8$ ohmics, (c) $\lambda/2$ ohmics, (d) $5/8\lambda$ ohmics.	42
4.5	Measured gain (+++) compared to theory (solid) for device AE05 on the 1.1 $\mu\text{m}$ layer doped at $5 \times 10^{15} \text{ cm}^{-3}$ .	44
4.6	Measured gain (+++) compared with theory (solid) for device AE06 on the 1.1 $\mu\text{m}$ layer doped at $5 \times 10^{15} \text{ cm}^{-3}$ .	45
4.7	Measured gain (+++) compared with simple theory (solid) and thin layer theory (---) for device AE207 on the 0.8 $\mu\text{m}$ layer doped at $5 \times 10^{15} \text{ cm}^{-3}$ .	47
4.8	Simplified diagram illustrating how dividing a segment into 2-D sections accounts for the variation of the electric field and charge distribution on the SAWAMP gain.	49
4.9	Two-dimensional plots of the amplitude of $E_z$ in segments with 3 $\mu\text{m}$ wide ohmics and segment lengths of (a) 3 $\mu\text{m}$ , (b) 6 $\mu\text{m}$ , (c) 12 $\mu\text{m}$ and (d) 60 $\mu\text{m}$ .	52
4.10	SAW potential profile into the depth of a {001}-cut GaAs substrate with SAW propagation in the $\langle 110 \rangle$ direction as predicted by ASIMM.	54



<b>4.11</b>	Gain per $\Delta z$ over the length of a 10 $\mu\text{m}$ long segment on a GaAs substrate uniformly doped at $5 \times 10^{13} \text{ cm}^{-3}$ with unity applied voltage.	56
<b>4.12</b>	Change in SAW amplitude over the length of a 10 $\mu\text{m}$ long segment on GaAs uniformly doped at $5 \times 10^{13} \text{ cm}^{-3}$ with applied voltage ranging from 0.2 to 1.0 V.	58
<b>4.13</b>	Comparison of the two-dimensional model (solid line) to the measured data (+) for device AE05.	59
<b>4.14</b>	Comparison of the two-dimensional model (solid line) to the measured data (+) for device AE207.	60
<b>4.15</b>	Test setup for layer thickness versus gain measurement.	62
<b>4.16</b>	Experimental gain measurement (+++) compared to the two-dimensional model (solid) for $R=400 \Omega$ .	64
<b>4.17</b>	Experimental gain measurement (+++) compared to the two-dimensional model (solid) for $R=200 \Omega$ .	65
<b>4.18</b>	Experimental gain measurement (+++) compared to the two-dimensional model (solid) for $R=40 \Omega$ .	66
<b>4.19</b>	Experimental gain measurement (+++) compared to the two-dimensional model (solid) for $R=15 \Omega$ .	67
<b>4.20</b>	An etch is used to isolate the active regions.	70
<b>4.21</b>	Two configurations for IDT position on GaAs/ZnO device: (a) IDT at interface and (b) IDT on top of ZnO.	73
<b>4.22</b>	SAW potential into the depth of the substrate for ZnO layer ranging from 0 to 6 $\mu\text{m}$ thick.	75
<b>4.23</b>	Predicted gain curve for the device of Figure 4.16 with a 1 $\mu\text{m}$ ZnO overlay	76



<b>4.24</b>	Predicted gain curve for the device of Figure 4.19 with a 1 $\mu\text{m}$ ZnO overlay.	77
<b>4.25</b>	Peak normalized gain for device for the devices of Figure 4.16 (lower) and 4.19 (upper) versus ZnO thickness.	79
<b>4.26</b>	Measured velocities calculated from center frequency measurements compared to the velocity for an open ZnO/GaAs surface from ASIMM.	82
<b>5.1</b>	Schematic illustration of a two slanted reflective arrays.	87
<b>5.2</b>	Reflection of a SAW from a single groove.	90
<b>5.3</b>	Reflection test structure.	93
<b>5.4</b>	S21 measurements of (a) IDT-IDT response, (b) T21, (c) T21.	96
<b>5.5</b>	Sketch of the effects of multiple reflections on the time response of T21.	101
<b>5.6</b>	Time response of T21 for a 600 stripe open grating with an Al thickness of 3800 $\text{\AA}$ .	102
<b>5.7</b>	Reflection coefficient of a single step, $ r $ , calculated from measured data for 200 Al stripes versus $h/\lambda$ (+) and the fit curve used to calculate C (solid).	103
<b>5.8</b>	SEM photographs of the 4300 $\text{\AA}$ grooves.	106
<b>5.9</b>	Normalized SAW amplitude versus depth into the grating as measured using the laser probe.	109
<b>5.10</b>	Reflection coefficient of a single step, $ r $ , calculated from measured data for 200 grooves versus $h/\lambda$ (+) and the fit curve used to calculate C (solid).	111





<b>6.1</b>	Schematic illustration of delay line loop with multiple paths between IDTs.	114
<b>6.2</b>	Measured frequency response between the two IDTs .	116
<b>6.3</b>	Time domain response between the two IDTs	116
<b>6.4</b>	Measured frequency response between IDTs with MAR-1 amplifiers in cascade.	118
<b>6.5</b>	Oscillator test circuit with external amplifiers.	119
<b>6.6</b>	Oscillation frequency measured on spectrum analyzer.	120
<b>6.7</b>	Multiple oscillations due to excess gain in the loop.	120
<b>6.8</b>	Ring oscillator layout.	123
<b>6.9</b>	Profile of ring resonator structure.	125
<b>6.10</b>	Time domain response between the two IDTs of AE426	129
<b>6.11</b>	Time domain response demonstrating gain on the direct path of AE430	130
<b>6.12</b>	Time domain response demonstrating gain on the double bounce of AE430	130



## LIST OF TABLES

Table	Page
4.1 SAWAMP test devices on mask AE1	38
4.2 SAWAMP test structure parameters on mask AE2	40
4.3 Resistance measurements for device AE213 for 2 etch depths	70
4.4 Value of $K^2$ for ZnO Layers	80
5.1 Reflector test structure parameters for Mask AE3	95
5.2 Values of $ \Gamma_{\text{grat}} $ calculated for Al stripes from measured data.	98
5.3 Values of $ \Gamma_{\text{grat}} $ calculated for grooves from measured data	108
6.1 Ring Resonator Design Parameters	122



# CHAPTER 1

## INTRODUCTION

### Objectives

The objective of this research is to study surface acoustic wave (SAW) amplification on thin epitaxial layers of GaAs and to explore the feasibility of a novel acoustic charge transport (ACT) device architecture based on this technology.

Acoustoelectric amplification was first demonstrated by Hutson et.al. [1] in 1961 using bulk acoustic waves (BAW) on CdS samples. Subsequent investigations revealed that amplification could also be achieved using a surface acoustic wave (SAW) [2]. SAW amplifier (SAWAMP) technology was well understood theoretically, but it never achieved widespread application because of difficulties in the implementation. The biggest impediments to this technology were material related, the most predominant being the inability to achieve high carrier mobility ( $> 200 \text{ cm}^2/\text{V}\cdot\text{s}$ ). As a result, a large voltage ( $> 1 \text{ kV}$ ) had to be applied in order to achieve a carrier drift velocity larger than the SAW velocity, which is the physical essence of the gain mechanism. Another impediment of SAWAMPs was the excessive power dissipation (typically  $> 1 \text{ W}$ ) resulting from the relatively low sheet resistance of the films that could be produced at that time. In many

cases, the amplifiers could be operated only in the pulsed mode to maintain an acceptable power dissipation.

It is the purpose of this dissertation to re-examine this technology in light of the many advances in the field of semiconductor materials in recent years so that a practically realizable device suitable for application in telecommunications systems may be developed. Here, it is proposed that the SAWAMP be implemented on a multilayer GaAs substrate. Fabricating the device on a thin, lightly doped epitaxial GaAs layer on SI GaAs makes it possible to attain the required sheet resistance while taking advantage of the high electron mobility of GaAs. The piezoelectric coupling coefficient ( $K^2$ ) of GaAs is small, but this may be overcome by using a piezoelectric overlay such as ZnO. The advantages of this choice of material over previously reported structures are the low voltage and low power operation which will be achieved, and the compatibility with standard GaAs IC processing.

In addition, it is proposed that an interdigital ohmic contact structure with line widths on the order of an acoustic wavelength be used to reduce the applied voltage necessary to achieve the necessary high drift field. The combination of high mobility and short gain segments defined by a pair of interdigital ohmic contacts, enables the use of a small applied voltage ( $< 5$  V), which is required for practical applications.

The SAW amplifier was initially viewed as a miniature replacement for the traveling wave tube, and efforts were directed toward producing good-quality SAW amplifiers that could compete with solid state electronic devices. The inability to achieve

this goal contributed somewhat to the failure of the technology. In this study, it is proposed that the amplifier be combined with reflector banks to create a single-chip SAW oscillator for use in an ACT device. Such an application does not require large bandwidth or high linearity and is exactly the type of application in which a SAW amplifier can be leveraged to give a cost or performance advantage in a telecommunications system.

The proposed ACT device is illustrated along with a conventional ACT device in Figure 1.1. In the conventional ACT device shown in Figure 1.1.a, the clock is provided by the propagating SAW, which is launched by an interdigital transducer (IDT) at one end of the device and dissipated in the acoustic absorber at the other end to eliminate unwanted reflections from the edge of the chip. It is common practice to add a reflector between the IDT and the end of the substrate to double the efficiency of the IDT. Because of the low coupling coefficient of GaAs, the IDT must have many electrodes, and will hence occupy a large die area. The reflector, although reducing the drive level of the external frequency source, also occupies an equivalent amount of real estate and makes the bandwidth of the IDT very small.

The center frequency of this narrow band IDT is temperature sensitive ( $-35$  PPM/ $^{\circ}\text{C}$ ), and the frequency source must track the peak of the conductance of the IDT to ensure maximum power transfer. One technique to alleviate this problem would be to add another IDT to the other end of the device and create an oscillator loop with an external amplifier and phase shifter.

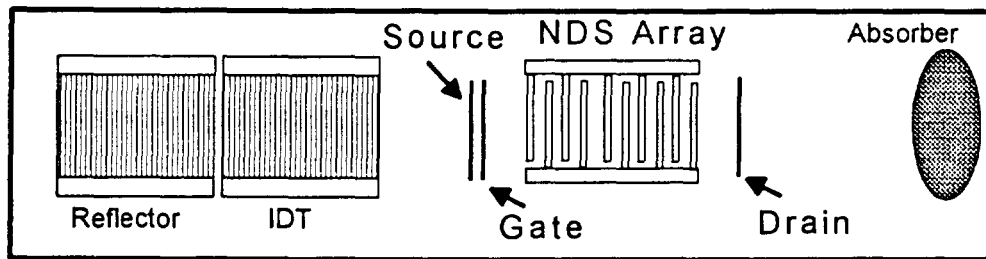
Alternatively, an on-chip oscillator could be created with a SAW amplifier, eliminating the need for IDTs as illustrated in Figure 1.1b. Such an oscillator, consisting of an amplifier embedded in between two IDTs with an external feedback cable has been reported [3]. The same technique will be used here, but the feedback will be via the pairs of slanted reflectors at the ends of the substrate, allowing the entire device to be contained on one chip.

The SAWAMP for this application need not be wideband, low noise, or highly linear. The oscillation will grow until the SAWAMP saturates, and it is in this nonlinear region that acoustic charge transport occurs. This on-chip clock will enable the development of a new class of self-contained ACT devices with much lower power dissipation than conventional devices. Not only does the device not need an external frequency source, but the power dissipation is predicted to be less than 100 mW as compared to 1 to 2 W dissipated by conventional ACT devices with the associated RF amplifier and frequency source.

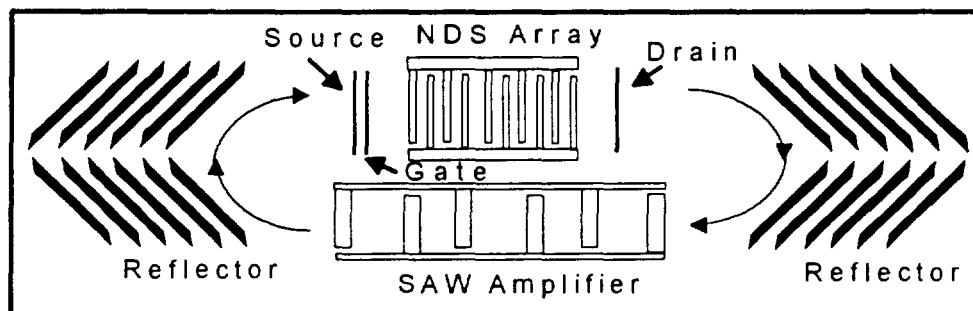
This thesis addresses the acoustoelectric issues which will enable the creation of the envisioned ACT device, namely the feasibility of a practical SAWAMP and the possibility of obtaining efficient reflector banks.

Chapter 2 presents a brief history of the SAWAMP and a simple theory of operation. In Chapter 3, the material structure consisting of a thick epi-layer on





(a) Conventional ACT device



(b) ACT device with on-chip clock

**Figure 1.1:** Conventional ACT device and ACT device with on-chip clock created by amplifier-reflector loop.

semi-insulating GaAs will be developed. The sheet resistance of this structure has been modeled and experimentally verified using several samples of varied thickness. Chapter 4 discusses the operation of a segmented SAWAMP on GaAs and presents the experiments carried out on this structure. The studies conducted include the wave propagation through the grating, the amplification achieved with very short segment length, power reduction using an etch , and the prediction of gain enhancement which would result from the addition of a piezoelectric film such as ZnO. In addition, some second order effects are considered to account for the performance of the device on very thin epi-layers.

An introductory theory of slanted reflectors has been presented in Chapter 5 along with a summary of the experiments which were conducted using both metal stripes and grooves on GaAs. It has been found experimentally that the grooves developed in this research provide a high reflection coefficient which will enable the development of efficient  $90^\circ$  reflector gratings. In Chapter 6 the integration of SAWAMP and reflectors will be discussed and experimental findings presented. Finally, in Chapter 7 a summary of the research will be presented along with conclusions.

## **CHAPTER 2**

### **BACKGROUND**

#### Origin and History

The interaction of acoustic waves with free carriers in semiconductors, which was first reported by Parmentor [4], gives rise to three characteristic effects: the attenuation or amplification of the waves, the change in the wave velocity resulting from the electron screening effects, and the generation of an acoustoelectric field. These effects may either be a nuisance or very interesting, depending on the ultrasonic frequency of operation of the device and the conductivity of the semiconductor on which it is fabricated. Many studies have been done in this area and the various mechanisms of interaction have been well described in two review papers [5,6].

#### SAWAMP Device Description

The basic SAW amplifier is shown schematically in Figure 2.1. The device consists of a piezoelectric semiconductor with launching and receiving transducers on either end and ohmic contacts in between. A drift voltage may be applied to the ohmic contacts to move electrons in the direction of the SAW propagation.

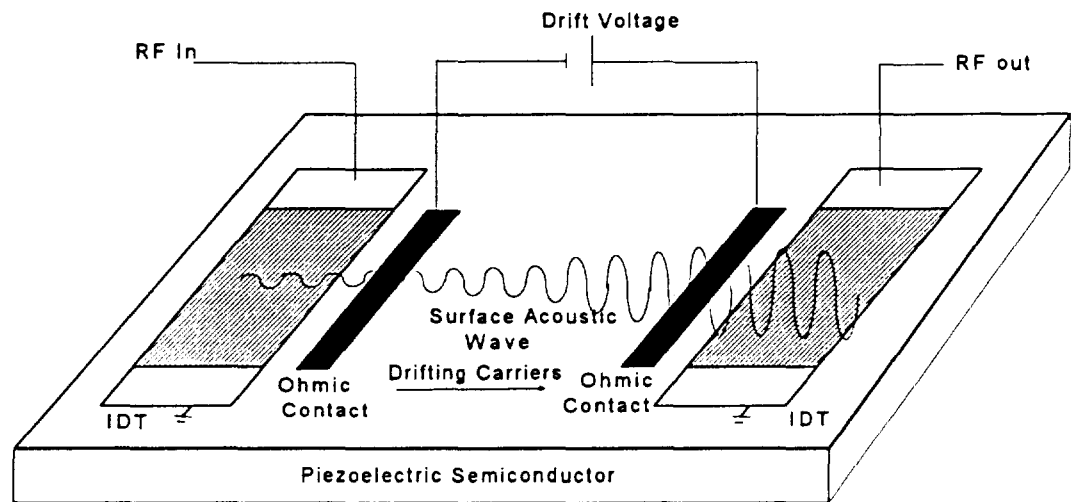


**Figure 2.1:** Schematic illustration of a SAW amplifier.

As illustrated, the RF signal generates a SAW via the transducer. When the velocity of the carriers accelerated by the drift field exceeds the SAW velocity, the wave is amplified.

### Theory of Operation

Many computational-intensive models based on tensors numerical have been derived to accurately describe the interaction of the SAW and free carriers in a piezoelectric semiconductor or a combination of piezoelectric and semiconductor materials [5,6]. A simple model has been adopted here based on the analytical theory of Adler [7]. This model, based on an equivalent circuit derivation, compares very closely with the more complex models and with experimental data. Because of its simplicity and accuracy, it lends more insight into the operation of the amplifier than the more mathematically complex description and runs in only a few seconds a PC, so it may be used as a design tool.

To begin, consider an elastic transmission line having a width of  $\lambda/2\pi$ . It is known that such a line without loss or dispersion may be modeled by a series inductance  $L_p$  and shunt capacitance  $C_p$  per unit length as shown in Figure 2.2a.  $L_p$  and  $C_p$  have been defined as [8]

$$L_p = \frac{K^2}{\epsilon_p v_o^2} \text{ and } C_p = \frac{\epsilon_p}{K^2} , \quad (2.1)$$

where  $\epsilon_p$  is the dielectric constant of the aggregate material and  $v_o$  is the velocity of the SAW on a free surface.

To account for the loss resulting from the free carriers in the substrate, an impedance  $Z$  is added to the circuit as in Figure 2.2b. This impedance is expressed as [8]

$$Z = \rho + \frac{1}{j\omega\epsilon_p} = \frac{1}{j\omega\epsilon_p}(1 + j\omega\tau) \quad , \quad (2.2)$$

where  $\rho$  is the resistivity of the semiconductor,  $\omega$  is the angular frequency of the SAW, and  $\tau = \epsilon_p \rho$  is defined as the relaxation time constant of the material.

In the presence of an electric field the impedance formula remains the same, but  $\omega$  is replaced by the Doppler shifted frequency of the wave  $\omega_D$  as observed by the electrons [7]

$$\omega_D = \omega \left( 1 - \frac{v_d}{v_o} \right) \quad , \quad (2.3)$$

where  $v_d = \mu V/L$  is the velocity of the drifting electrons,  $\mu$  is the electron mobility,  $V$  is the applied voltage, and  $L$  is the length over which the voltage is applied.

The time constant  $\tau$  is only equal to  $\epsilon_p \rho$  for a semi-infinite semiconductor layer. For a thin layer, as used in this thesis, it has been shown that [7]

$$\omega_D \tau = \omega \left( 1 - \frac{v_d}{v_o} \right) \epsilon_p \rho \frac{\lambda}{2\pi d} = \left( 1 - \frac{v_d}{v_o} \right) \frac{\epsilon_p \rho V_o}{d} \quad (2.4)$$

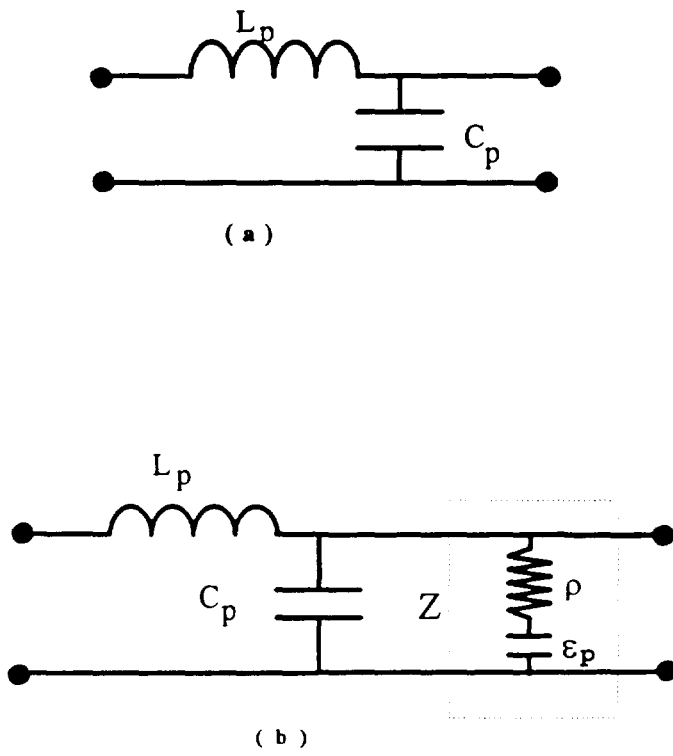


**Figure 2.2:** Transmission line models of acoustic propagation (a) on a piezoelectric and (b) on a piezoelectric/semiconductor composite.

where  $d$  is the thickness of the semiconducting layer and  $\lambda$  is the acoustic wavelength.

The propagation constant of the transmission line of Figure 2.2 (b) is characterized by [8]

$$\begin{aligned} k &= \sqrt{\omega L_p (j\omega C_p + Z^{-1})} = \sqrt{\frac{K^2 \omega}{\epsilon_p v_o^2} \left( j \frac{\epsilon_p \omega}{K^2} + \frac{j\omega \epsilon_p}{1 + j\chi} \right)} \\ &= \frac{\omega}{v_o} \left( 1 + \frac{K^2}{1 + j\chi} \right)^{\frac{1}{2}} \end{aligned} \quad (2.5)$$

where  $\chi$  is defined as

$$\chi = \omega_D \tau \quad (2.6)$$

For small  $K^2 (< 0.1)$ , as is the usual case,  $k$  may be approximated by a truncated binomial expansion:

$$k \cong \frac{\omega}{v_o} \left( 1 + \frac{K^2}{2} \frac{1}{1 + j\chi} \right) \quad (2.7)$$

and  $\alpha$ , the gain (in nepers per unit length) is the imaginary part of  $k$ :

$$\alpha = -\frac{\omega}{v_o} \frac{K^2}{2} \frac{\chi}{1 + \chi^2} \quad (2.8)$$

From this simple equation, the gain mechanism may be easily understood.

First of all, consider the case where there is no applied voltage, that is  $v_o = 0$ . The the  $\chi$  term becomes



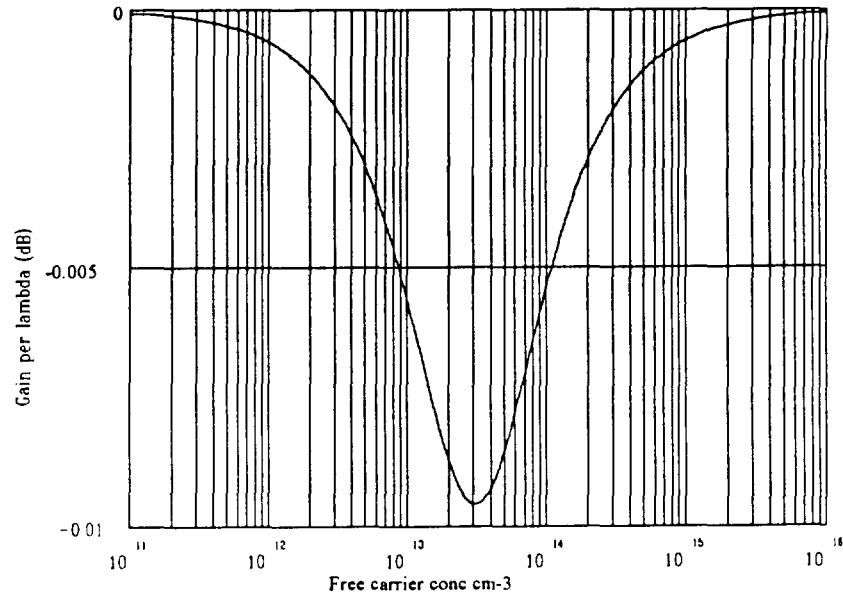


**Figure 2.3:** Gain per wavelength versus free carrier concentration for a 1000 Å layer of n-type GaAs with no applied voltage.

$$\chi = \frac{\epsilon_p \rho v_o}{d} \quad (2.9)$$

which for a given material (with fixed  $K^2$ ,  $v_o$  and  $\epsilon$ ) makes  $\alpha$  dependent only on the sheet resistance  $\rho/d$  and the SAW frequency of operation. The gain is presented for a SAW propagating on a 1000 Å layer of doped GaAs at 240 MHz in Figure 2.3. This plot of the gain per wavelength versus the free carrier concentration of the layer illustrates the range of doping over which the SAW will interact with the free carriers. At the lower limit, the time constant of the material is large and the carriers do not respond fast enough to cause any screening of the SAW potential. At the upper limit the carriers react quickly to the SAW field, and appear as a shorted surface to the SAW so again, no attenuation occurs. The maximum charge screening occurs at a free carrier concentration of  $3 \times 10^{13} \text{ cm}^{-3}$ , which is where the relaxation frequency of the carriers is equal to the angular frequency of the SAW.

This interaction is clearly illustrated by considering the effect of the free carrier concentration on the SAW velocity. The velocity may be obtained as the real part of  $k$ , where  $v = \frac{\omega}{\text{Re}(k)}$ , which from (2.7) gives

$$v = \frac{\omega}{\frac{\omega}{v_o} \left( 1 + \frac{k^2}{2} \frac{1}{1 + \chi^2} \right)} = \frac{v_o}{\left( 1 + \frac{k^2}{2} \frac{1}{1 + \chi^2} \right)} \quad (2.10)$$

This relationship is plotted in Figure 2.3. It may be seen that at low carrier concentrations, the velocity is that of a SAW propagating on a free {100}-cut, <110>

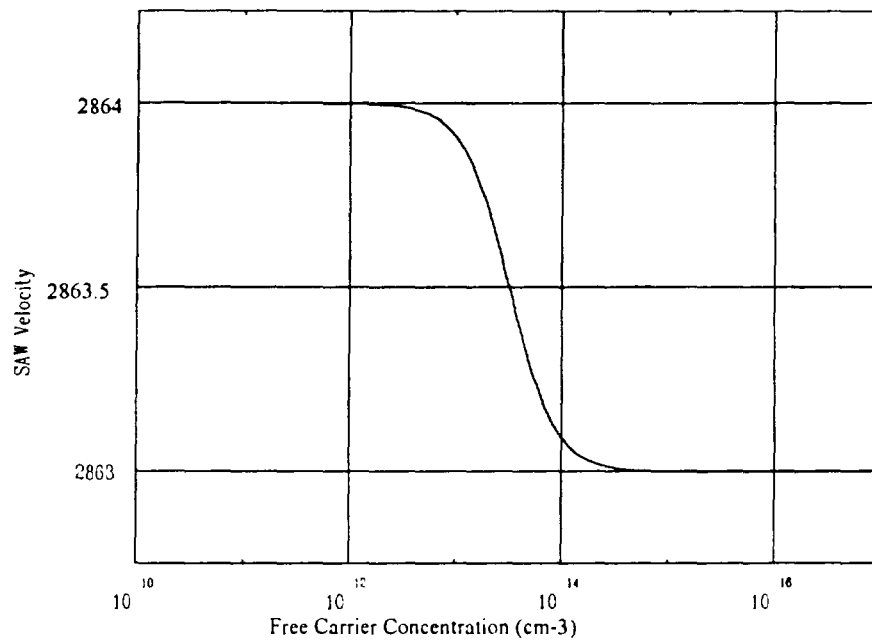


**Figure 2.4:** SAW velocity versus free carrier concentration for a 1000 Å layer of n-type GaAs with no applied voltage.

propagating GaAs surface ( $v_o=2864$  m/s). At about  $10^{12}$ , the velocity begins to decrease, and at about  $10^{15}$ , the velocity becomes that of a SAW propagating on the same GaAs surface coated with an infinitesimally thin sheet of metal ( $v_s = 2863$  m/s).

The relationship

$$K^2 = 2 \frac{(v_o - v_s)}{v_o} \quad (2.11)$$

is the standard approach used to calculate the piezoelectric coupling coefficient  $K^2$ . As such, the maximum fractional SAW velocity shift which may be achieved on a piezoelectric semiconductor is  $K^2/2$ . This effect has been utilized by Grudkowski to develop variable SAW delay lines by varying the free carrier concentration in a thick epi-layer of GaAs [9].

Now when a voltage is applied, the  $\chi$  term is no longer zero, and the attenuation will be changed as follows. For  $v_d < v_o$ , the  $\chi$  term is positive so that  $\alpha$  is negative, indicating a propagation loss. When  $v_d > v_o$ , the  $\chi$  term become negative and consequently  $\alpha$  becomes positive, indicating that a gain is now realized.

For illustration purposes, the gain (in dB/cm) has been plotted against an electric field in Figure 2.5 for a 1 cm long amplifier on a 1000 Å layer of n-type GaAs, with a free carrier concentration of  $1 \times 10^{14} \text{ cm}^{-3}$  and an assumed mobility of  $6500 \text{ cm}^2/\text{Vs}$ . It is interesting to point out that the curve is not symmetric about the zero voltage point, but rather is symmetric about the point where  $(1 - v_d/v_o) = 0$ . Note that the maximum gain is equal to that of the maximum loss as one would expect.

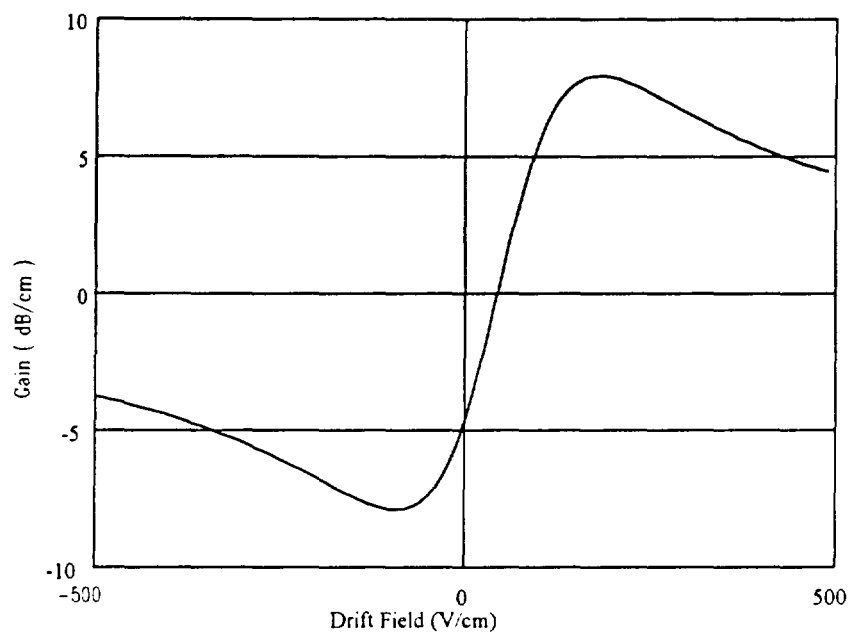


**Figure 2.5:** Gain versus applied drift field for a 1000 Å layer of n-type GaAs with a free carrier concentration of  $1 \times 10^{14} \text{ cm}^{-3}$

This model was used on a widespread basis in many of the early publications and provided a relatively good prediction of device performance particularly the monolithic devices. It is only a first order model , but has been used to gain an understanding of the device and to establish a basis on which to devise experiments. As will be shown in Chapter 4, the model does not account for the reduced gain experimentally measured for devices fabricated on very thin films. Further consideration of second order effects which affect the performance of the device are presented in Chapter 4.

## CHAPTER 3

# MATERIAL STRUCTURE

### History

There were several material structures in which it was possible to create an interaction between the SAW and the free carriers as illustrated in Figure 2.4. The simplest approach was to use a piezoelectric semiconductor such as CdS or GaAs. Unfortunately, there is no material yet found to simultaneously have good semiconducting and piezoelectric properties. An improved approach was to place a semiconductor either directly on, or in close proximity to, a piezoelectric substrate, allowing the separate optimization of both materials. Devices have been demonstrated with both the separated medium structure [10] and the monolithic structure [11]. The separate medium amplifier allowed the greatest degree of freedom in the choice of materials as the two substrates were separated by small pillars as shown in Figure 2.1 (b). Because the electric field decayed across the air gap, the separation had to be small and uniform across the entire device. The structure was mechanically cumbersome and the device performance was sensitive to the air gap thickness, making a monolithic approach more attractive.

The monolithic structure is illustrated in Figure 2.1 (c) and (d) consists of two materials mechanically bonded in some fashion. This technique was more manufacturable but it was difficult to obtain compatible materials. The most widely used monolithic structure was comprised of an InSb film on a LiNbO<sub>3</sub> substrate, chosen because of the relatively large piezoelectric coupling coefficient of LiNbO<sub>3</sub> and the theoretically high carrier mobility of bulk InSb ( 80,000 cm<sup>2</sup>/V·s). In practice, this high electron mobility has never been realized in such structures. Because of the small bandgap of InSb (0.17 eV), the room temperature resistivity was high. In order to achieve a high sheet resistance, it was necessary to grow the InSb films on the order of 500 Å thick, but in such thin films, the electron mobility was degraded. Mobilities in low hundreds were common in early publications, resulting in the need for a high drift voltage. The high drift fields and low resistance resulted in high power dissipation, and in most cases these devices were limited to pulsed-mode operation to prevent overheating.

A recent publication using this structure has reported mobility on the order of 1000 cm<sup>2</sup>/V·s [3] by inserting a SiO<sub>2</sub> layer between the substrate and the film and post processing the film after deposition. The resistivity of the film was only on the order of 20 kΩ/sq , but a narrow aperture (25 μm) amplifier was reported with a continuous mode peak gain of 35 dB and power dissipation of 500 mW. Although the power dissipation was relatively low, the applied voltage (~1.2 kV) was unacceptable for a



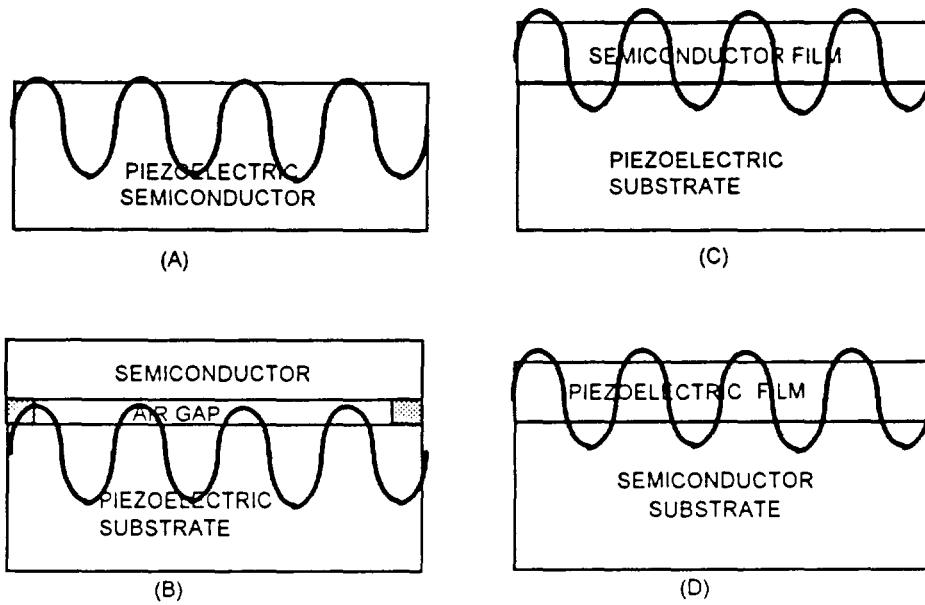


**Figure 3.1:** SAW Amplifier structures: (a) piezoelectric semiconductor, (b) separated medium, (c,d) monolithic mediums.

practical device. This technique could be the most desirable approach given the ability to attach a thin high resistivity, high mobility semiconductor structure such as GaAs to a  $\text{LiNbO}_3$  substrate. It has been shown in [12] that it is possible to attach a thin GaAs layer to  $\text{LiNbO}_3$  using epitaxial liftoff, but this has not been explored here.

The final technique to be discussed is the deposition of a piezoelectric film on a doped semiconductor substrate. Taracki and White [13] demonstrated a device consisting of a ZnO film on Si, yielding a gain of 21 dB/cm at 440 MHz at an applied voltage of 3000 V. This device was limited to pulsed mode at voltages over 1000 V because of the high power dissipation. However, this publication demonstrated that a piezoelectric overlay on a non-piezoelectric substrate was a feasible implementation. This technique could be improved greatly using modern semiconductor materials and processing techniques. In this thesis a ZnO/GaAs composite has been considered by the author because of the relatively good acoustic match between ZnO and GaAs. The addition of a piezoelectric overlay will be discussed further in Chapter 4.

### Multilayer GaAs Material Structure

The biggest limitation of the previous SAWAMP research is the inability to acquire a suitable material. As put by Suppyro Datta [14], "for best results, what is needed is a thin layer with high mobility and few carriers." As mentioned above, the schemes that were used were limited by the material technology available at the time.

In [15], it was concluded theoretically that given the ability to grow thin layers of n-type GaAs with carrier concentrations on the order of  $1 \times 10^{14} \text{ cm}^{-3}$ , a continuous mode acoustoelectric amplifier utilizing a longitudinally polarized wave on GaAs could be realized. With molecular beam epitaxy (MBE) [16], it is now possible to create this type of structure. This material scheme has been chosen in this proposal as it is the simplest to work with in a development laboratory environment and given the low doping, a sufficiently high mobility ( $4000 - 8000 \text{ cm}^2/\text{V}\cdot\text{s}$ ) may be achieved at room temperature.

The GaAs epilayer must be lightly doped and very thin in order to maximize the gain at a minimum power dissipation. Using the model of simple model described in Chapter 2, the structure was optimized to give maximum gain at the highest possible sheet resistance. Figure 3.2 displays the gain curves for a 1 cm long SAWAMP on a  $1000 \text{ \AA}$  layer of GaAs at free carrier concentrations ranging from  $1 \times 10^{13} \text{ cm}^{-3}$  to  $5 \times 10^{14} \text{ cm}^{-3}$ . At the lowest doping the gain curve peaks at a low voltage but the peak of the curve is very narrow indicating that the device would be voltage sensitive. As the carrier concentration increases, the peak gain becomes slightly higher and the curves become flatter, but the peak gain occurs at higher drift voltage resulting in much higher power dissipation. From this exercise, it was decided that the target free carrier concentration should be between  $5 \times 10^{13}$  and  $1 \times 10^{14} \text{ cm}^{-3}$ , which translates into a sheet resistance of approximately  $1 \text{ M}\Omega/\text{sq}$ .

Because the surface states deplete a thin, lightly doped layer completely, it was not possible to directly grow the desired layer. However, it was possible to grow a

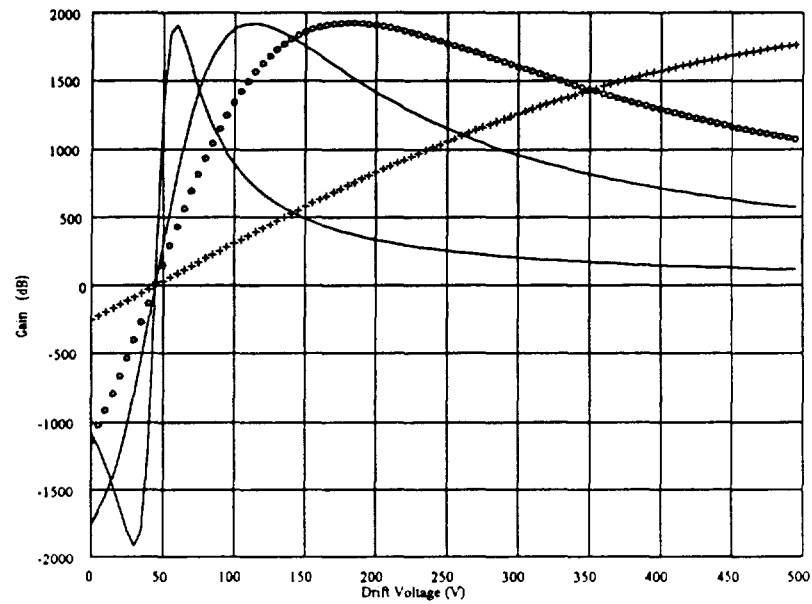
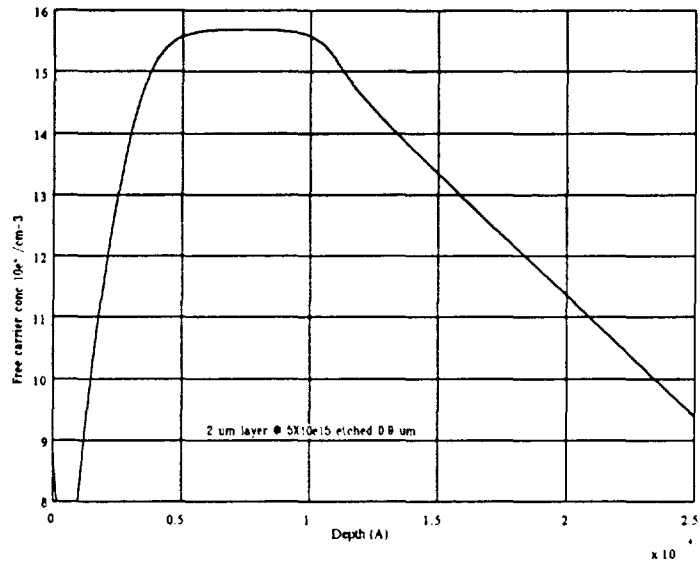


**Figure 3.2** Gain curves for a 1 cm long SAWAMP on a 1000 Å layer of GaAs with the following free carrier concentrations:  $1 \times 10^{13} \text{ cm}^{-3}$  (—),  $5 \times 10^{13} \text{ cm}^{-3}$  (---),  $1 \times 10^{14} \text{ cm}^{-3}$  (ooo),  $5 \times 10^{14} \text{ cm}^{-3}$  (++).

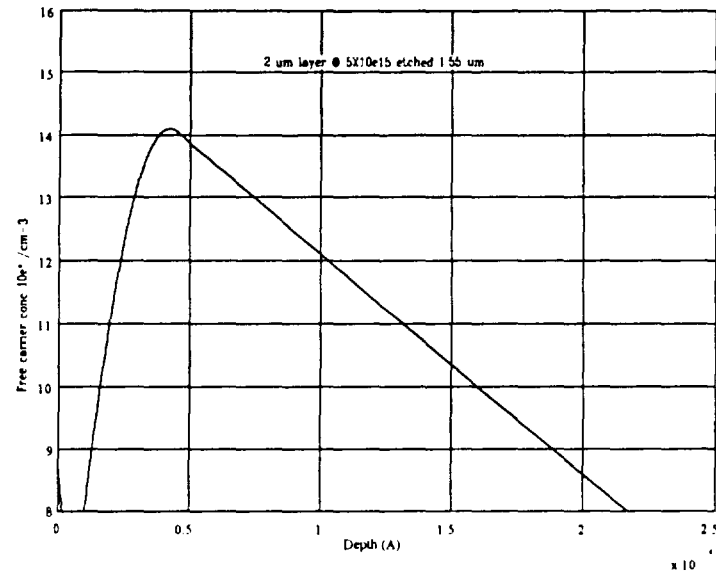
thicker layer at a higher doping level. This thick layer had a much lower sheet resistance than desired but was etched down to provide the necessary high resistance. As the layer was etched, not only did the layer become thinner but the surface state recombination also lowered the carrier density. Figure 3.3 shows the carrier density profile for a 1.1  $\mu\text{m}$  layer as predicted using the HETMOD simulator [17]. This plot illustrates that there was approximately 0.5  $\mu\text{m}$  of depletion at the surface resulting from the surface state recombination. Below the 0.5  $\mu\text{m}$  depletion layer there was a 0.6  $\mu\text{m}$  layer of reasonably well defined charge with a free carrier concentration of about  $5 \times 10^{15} \text{ cm}^{-3}$ .

Figure 3.4 shows the theoretical profile for a 0.45  $\mu\text{m}$  layer. As may be observed, the charge confinement layer becomes thinner and less defined, and the peak charge concentration decreases as the layer is thinned. As such, the relationship between layer thickness and sheet resistance is not linear for GaAs but rather an exponential sort of curve as plotted in Figure 3.4. From the original assumptions the model was based on, this 0.45  $\mu\text{m}$  layer appeared to be the desired thickness. These plots clearly illustrates why the desired 1000  $\text{\AA}$  thick layer could not be directly grown at a very light doping. If it were possible to grow a 1000  $\text{\AA}$  layer doped at  $5 \times 10^{13} \text{ cm}^{-3}$ , there would be no free carriers in the layer as it would be completely depleted by the surface states.

An experiment was conducted by the author to determine the layer thickness which would yield the desired sheet resistance in practice using the HETMOD curve as a guide.



**Figure 3.3:** Free carrier density profile for a  $1.1 \mu\text{m}$  layer of GaAs doped at,  $5 \times 10^{15} \text{ cm}^{-3}$  on semi-insulating GaAs.



**Figure 3.4:** Free carrier density profile for a  $0.45 \mu\text{m}$  layer of GaAs doped at  $5 \times 10^{15} \text{ cm}^{-3}$  on semi-insulating GaAs.

This experiment consisted of a number of samples being etched to different thicknesses to verify the theoretical predictions. The data is compared to the HETMOD predictions in Figure 3.5. The data point at the 2  $\mu\text{m}$  thickness was performed using an m-gauge on the received wafers. The other data points were obtained by etching the samples using a  $\text{H}_3\text{PO}_4 / \text{H}_2\text{O}_2 / \text{H}_2\text{O}$  solution at a ratio of 3:1:50 and then fabricating ohmic contacts on the resulting surface. The ohmic contacts consisted of 800  $\text{\AA}$  of AuGe, 100  $\text{\AA}$  of Ni and 1000  $\text{\AA}$  of Au deposited in a CVC filament evaporator. As a final step, the ohmics were annealed at 365  $^\circ\text{C}$  in a CVC rapid thermal processor.

As may be observed from Figure 3.5, the data points differ greatly from the original HETMOD prediction. An explanation for this disparity may be found in the method used to grow the material. The epi-layer was grown directly onto a GaAs wafer. Normally a buffer layer of nonintentionally doped (NID) GaAs is grown first to provide a very smooth surface on which to grow the doped layer, which is the condition assumed in the HETMOD program. Because a buffer layer was not used here a significant depletion will result from the interface states at the epi-layer-substrate interface. It was estimated that as much depletion occurred at the interface as at the surface. The dashed curve of Figure 3.5 represents a calculation performed assuming the epi-layer was in fact 0.5  $\mu\text{m}$  thinner than it actually was. This assumption gave a much closer match between the predicted sheet resistance and the experimental data. From this experiment, it appeared that the  $1\text{M}\Omega/\text{sq}$  sheet resistance would be achieved at a layer thickness of approximately 0.95 to 1  $\mu\text{m}$ .



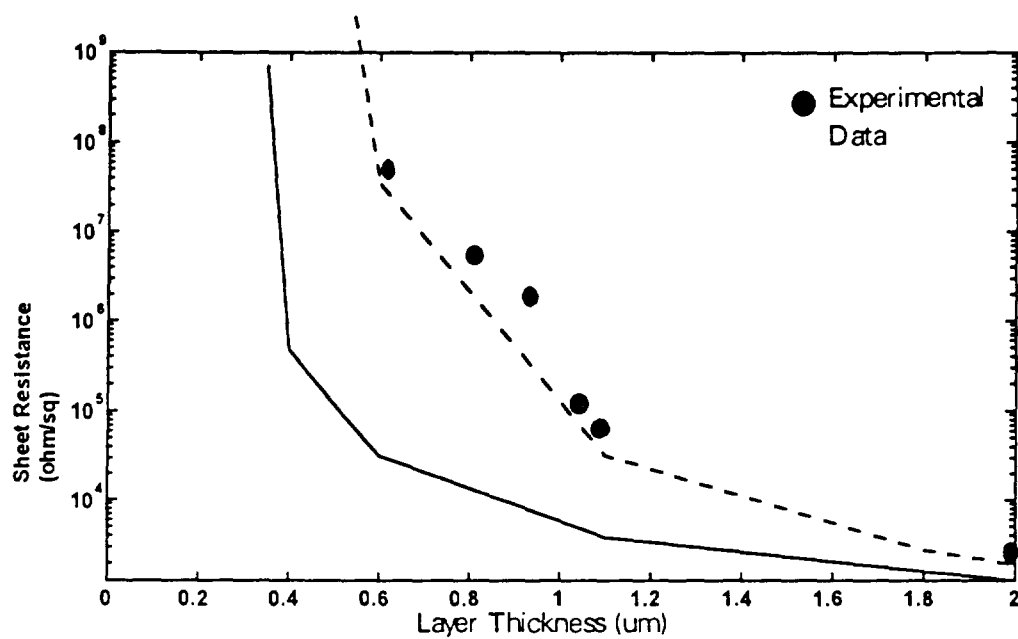


**Figure 3.5:** Experimental sheet resistance compared to theoretical predictions using HETMOD (—) assuming no interface depletion, (---) assuming 0.5  $\mu\text{m}$  of interface depletion.

Although this material seemed to be the right choice from an electrical point of view, some interesting effects were observed by the author when SAWAMPs were fabricated on this thin material. This will be further discussed in Chapter 4.

## CHAPTER 4

### SEGMENTED SAWAMP STRUCTURE

In this chapter, the experiments conducted on segmented SAWAMP structures on epilayers of GaAs have been documented and some explanation for the discrepancies between the experimental data and the simple model of Chapter 2 have been developed using a two-dimensional approach. This chapter starts with a brief history of the segmented SAWAMP followed by a description of the test structures used in this thesis and the test setup. Experimental data has been presented for a number of devices with varied layer thickness fabricated by the author. It was observed early in the experimental process that the reflections in the ohmic grating were a potential problem. Methods of resolving this problem with adjustments to the ohmic widths and spacing have been presented here.

The amplification data gathered from devices fabricated on thick layers gave reasonable agreement with the simple model, however the simple model did not accurately predict the performance of thin layer devices. An extension of the model which includes the non-uniform electric field and free carrier concentration into the depth of the

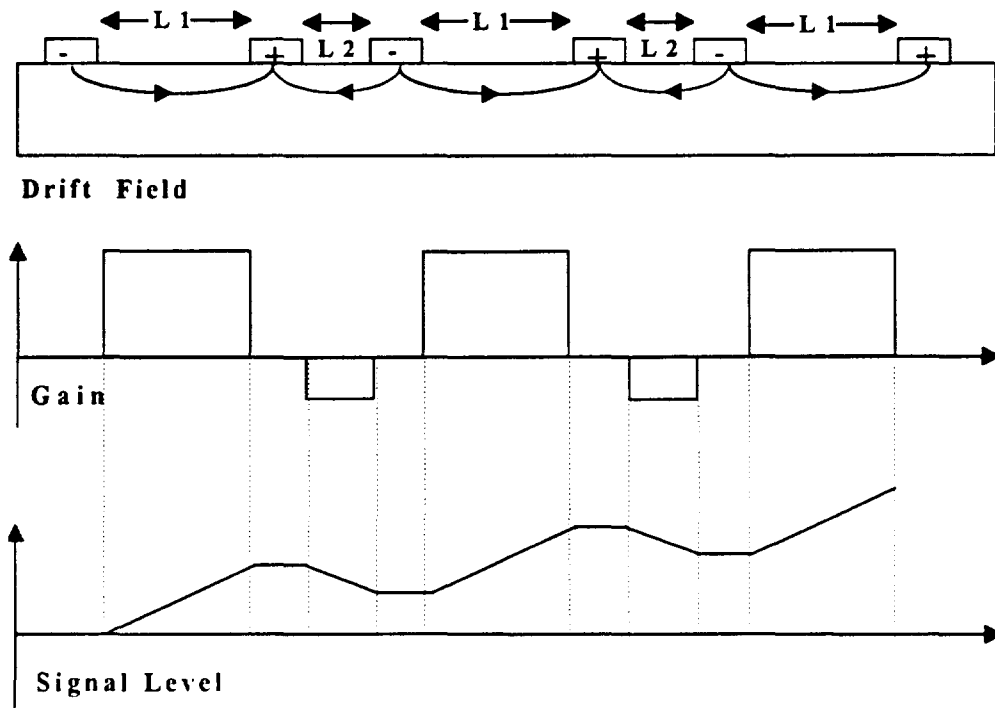


**Figure 4.1** Operation of a segmented amplifier structure.

substrate was developed by the author to provide a better understanding of the device operation, particularly for devices on submicron epilayers. Next some power reduction techniques have been discussed and a simple etching technique which has been developed in this thesis to reduce the power consumption has been documented. Finally the addition of a ZnO overlay to increase  $K^2$  has been considered both experimentally and theoretically by the author in the last section of the chapter, resulting in the predictions of greatly increased gain.

### Background

As discussed in Chapter 1, one of the limiting factors in the practical use of SAWAMPs was the high voltage requirement. This requirement was resolved somewhat by using a segmented structure [18] as illustrated in Figure 4.1. Rather than having two ohmic contacts as in the original device illustrated in Figure 2.1, the amplifier is segmented into many smaller sections over which a much smaller voltage need be applied in order to generate the same high drift field. The length of the segment has been defined as  $L_1$  and the segment separation as  $L_2$ . When the drift field is in the same direction as the SAW propagation, the SAW experiences gain. When the field is counter to the SAW propagation, the SAW experiences loss. A SAW propagating through the segmented amplifier experiences an alternating gain and loss in each period of the structure, and the gain of the overall structure is the sum of the gain in the  $L_1$  sections and the loss in the

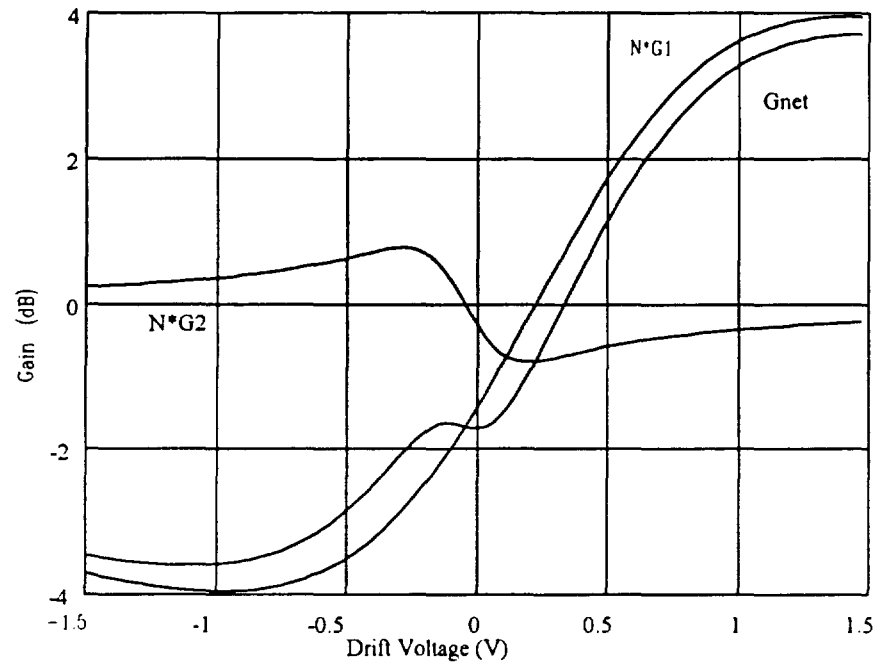


**Figure 4.2:** Gain curves for a segmented SAWAMP on a 3500 Å layer of GaAs doped at  $1 \times 10^{14} \text{ cm}^{-3}$  with  $L1 = 50 \text{ } \mu\text{m}$ ,  $L2 = 10 \text{ } \mu\text{m}$  and  $N = 100$ .

L2 sections. If L1 is longer than L2, then the SAW experiences more gain than loss and a net gain is produced by the segmented amplifier. The gain of this device may be calculated simply as an extension of the model of Chapter 2. The gain is expressed as:

$$G_{\text{net}} = N(G_1 + G_2) \quad (4.1)$$

where  $N$  is the number of sections, and  $G_1$  and  $G_2$  are the gain (or loss) of the  $L_1$  and  $L_2$  sections respectively as calculated using equation 2.8. The gain curves for  $NG_1$ ,  $NG_2$  and  $G_{\text{net}}$  have been plotted for a segmented SAWAMP on a 3500 Å layer of GaAs doped at  $1 \times 10^{14} \text{ cm}^{-3}$  with  $L_1 = 50 \text{ } \mu\text{m}$ ,  $L_2 = 10 \text{ } \mu\text{m}$  and  $N = 100$  in Figure 4.2. As may be observed the net gain  $G_{\text{net}}$  is very similar to  $NG_1$ , with a slight gain reduction due to the loss in the  $L_2$  sections. As one would expect, the larger the  $L_1/L_2$  ratio, the less effect the  $L_2$  sections will have on the net gain. The most noticeable effect the  $L_2$  section has on the net gain is the inflection in the curve near  $V=0$ .

Segmented structures have been demonstrated successfully on CdS with  $L_1 = 500 \text{ } \mu\text{m}$  and  $L_2 = 250 \text{ } \mu\text{m}$  [19]. The voltage for maximum gain for these devices occurred around 120 V. A continuous mode amplifier has been recently reported using a segmented structure on a CdSe film ( $\mu \sim 200 \text{ cm}^2/\text{V}\cdot\text{s}$ ) deposited on  $\text{LiNbO}_3$  operating at 20 V with segments of 126  $\mu\text{m}$  in length [20].

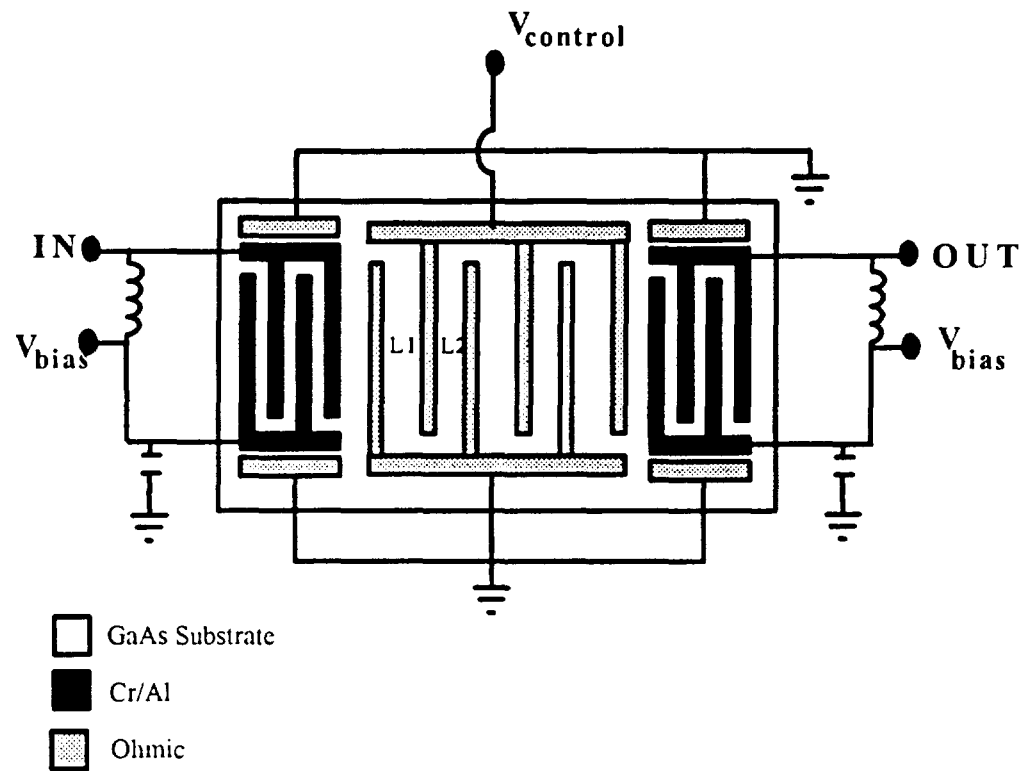


**Figure 4.3:** Amplifier test schematic.

### SAWAMP Testing

#### Test Structure



The segmented amplifier test structure used in this thesis consists of a series of interdigitated ohmic metal amplifier segments in between two IDTs as illustrated in Figure 4.2. The material was prepared using the process described in Chapter 3. The ohmic contacts were a standard alloy consisting of 800 Å of AuGe, 100 Å Ni and 1000 Å of Au. The IDTs were 1000 Å of Al over 100 Å of Cr. The Cr was necessary as an adhesion layer. The ohmic rails running along side the IDT busbars were used for depleting the area under the IDT in order to minimize the shorting effects under the IDT as demonstrated in [ 21]. The dimensions were varied as tabulated in Table 4.1. The ohmic width was kept constant at 3  $\mu\text{m}$  for all devices. Each die was 10 mm x 2.5 mm and there were approximately 40 die per 2" wafer.

### Test Setup

The die were packaged in 16 pin DIPs and tested on a double sided copper clad FR-4 test board. The frequency response of the device was measured on the RF ports using a HP8753C network analyzer. There were two DC power supplies, one used to deplete the regions under the IDTs and the other to apply the drift voltage to the amplifier test structure. Care was taken in adding decoupling components to isolate the

**Table 4.1** SAWAMP test devices on Mask AE1

Device	Center Frequency (MHz)	Number of Rungs	L1 (um)	L2 (um)
AE01	240	350	3	3
AE02	240	300	6	3
AE03	240	200	15	3
AE04	240	120	30	3
AE05	240	200	12	6
AE06	240	120	30	6
AE07	240	70	60	6
AE08	240	150	18	9
AE09	240	90	45	9
AE10	240	50	90	9

IDTs from each other at the RF frequency of operation.

The gain was measured by using the insertion loss of the device with no voltage applied as the zero reference. The marker was fixed at maximum magnitude point, and

this frequency was used to measure the insertion loss of the device while varying the applied voltage.

### Reflections in the Ohmic Grating

Although some reflections were expected from the ohmic gratings, the effect was found to be more pronounced than predicted for 3  $\mu\text{m}$  finger widths. As a result, the insertion was high on some of the devices and the bandwidth very narrow. The insertion loss ranged from 30 dB to over 50 dB, depending on the ohmic finger spacing. The bandwidth was on the order of 200 kHz which was an order of magnitude lower than predicted based on the length of the IDTs.

It is well known that  $1/8$  wavelength fingers in IDTs are reflectionless at the synchronous frequency, but this would limit the ohmic width to 1.5  $\mu\text{m}$ . It is difficult to fabricate such a long, narrow ohmic, but it was felt that investigation of this effect was necessary in order to improve the signal quality of the SAWAMP. A second mask was issued with ohmic widths of  $1/8$ ,  $3/8$ ,  $1/2$  and  $5/8 \lambda$  as documented in Table 4.2. These

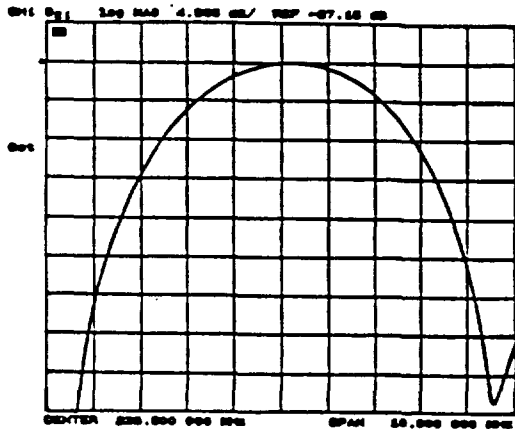
**Table 4.2** SAWAMP test structure parameters on mask AE2

Device	Stripe Width	Number of Rungs	L1 (um)	L2 (um)
AE202	1.5	220	13.5	1.5
AE203	1.5	140	25.5	1.5
AE204	1.5	100	37.5	1.5
AE205	4.5	220	4.5	4.5
AE206	4.5	130	16.5	4.5
AE207	4.5	95	28.5	4.5
AE208	4.5	75	40.5	4.5
AE209	6.0	170	6.0	6.0
AE210	6.0	110	18.0	6.0
AE211	6.0	85	30.0	6.0
AE212	6.0	70	42.0	6.0
AE213	7.5	130	7.5	7.5
AE214	7.5	95	19.5	7.5
AE215	7.5	75	31.5	7.5
AE216	7.5	60	43.5	7.5

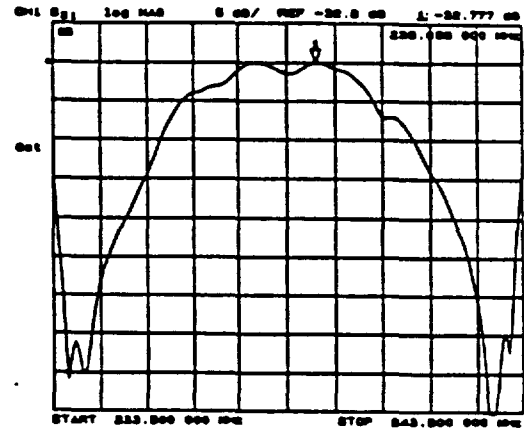
devices were similar to the initial mask set except that the IDTs had 50 split finger pairs so that the measurement would not be affected by the internal IDT reflections. Four frequency responses for different devices are shown in Figure 4.4. The responses

compared between two IDTs with no ohmic grating, and devices AE204, AE212 and AE216. frequency responses It was found that  $\lambda/8$  gratings introduced very little distortion to the S21 measurement but 5.5 dB of loss was observed. The  $\lambda/2$  and  $5/8\lambda$  gratings introduced similar amounts of ripple in the passband and similar loss of approximately 12 dB. The  $3/8\lambda$  gratings were similar to the  $\lambda/4$  case and were not plotted.

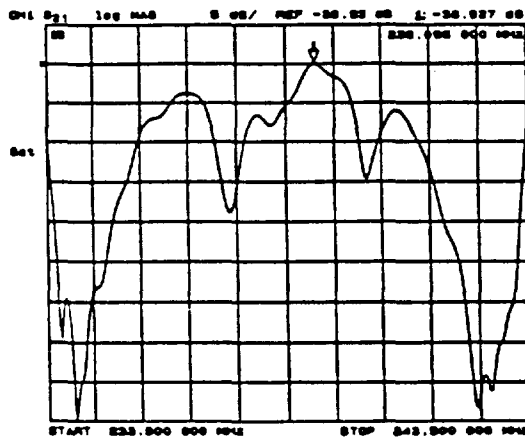
These reflections are only an issue for long SAWAMP structures. It is anticipated by the author, that this will not be as significant an issue for higher coupling materials, as the length of the SAWAMP will scale inversely with the  $K^2$  of the aggregate structure for a constant gain. Also, the height of the step is an issue, particularly at higher frequencies where the height to wavelength ratio will be large. Again, the length of the device will be shorter as the gain per distance increases with decreasing wavelength, so this may not be an issue.



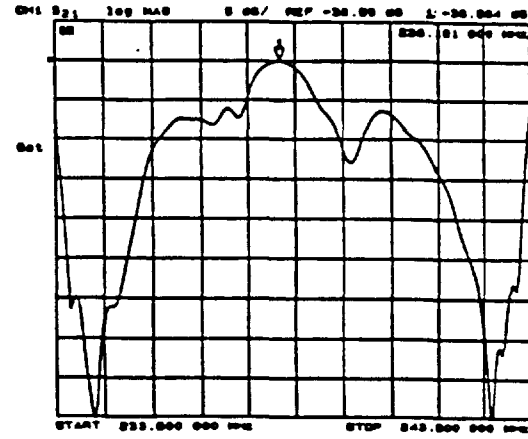
(a)



(b)



(c)



(d)

**Figure 4.4:** Frequency responses of (a) Two IDTs, (b)  $\lambda/8$  ohmics, (c)  $\lambda/2$  ohmics, (d)  $5/8\lambda$  ohmics.

### Experimental Gain Measurements

#### SAWAMP Gain Measured for Devices on Thick Layers

Although the reflections in the ohmic grating affected the shape of the passband of the devices, this did not reduce the ability to observe acoustoelectric gain in these devices. The only limitation was that the high insertion loss in some of the devices made it difficult to take an accurate measurement. Figures 4.5 and 4.6 compare the measured gain difference curves for devices AE05 and AE06 on the 1.1  $\mu\text{m}$  layer to the theoretical prediction based on the model of Section 2.1. Based on the model of Chapter 3, it was assumed that this layer in fact had a charge confinement layer of 0.5  $\mu\text{m}$ .

The zero voltage gain was normalized to the loss of the test device with no applied voltage, which in the case of these two devices was about 36 dB. AE05 had a peak delta gain of approximately 3 dB/cm and the longer segments of AE06 gave an increased delta gain of about 4 dB/cm. Both devices have reasonable agreement with the simple theory in the forward voltage region but deviate somewhat in the reverse direction. The dissipated DC power was approximately 300 mW, which was expected for the low sheet resistance of the thick layer of doped GaAs. It was anticipated by the author, based on the simple model that the use of thinner layers would yield identical gain at a power consumption on the order of 10 mW. In the next section the findings of this experiment have been presented by the author.

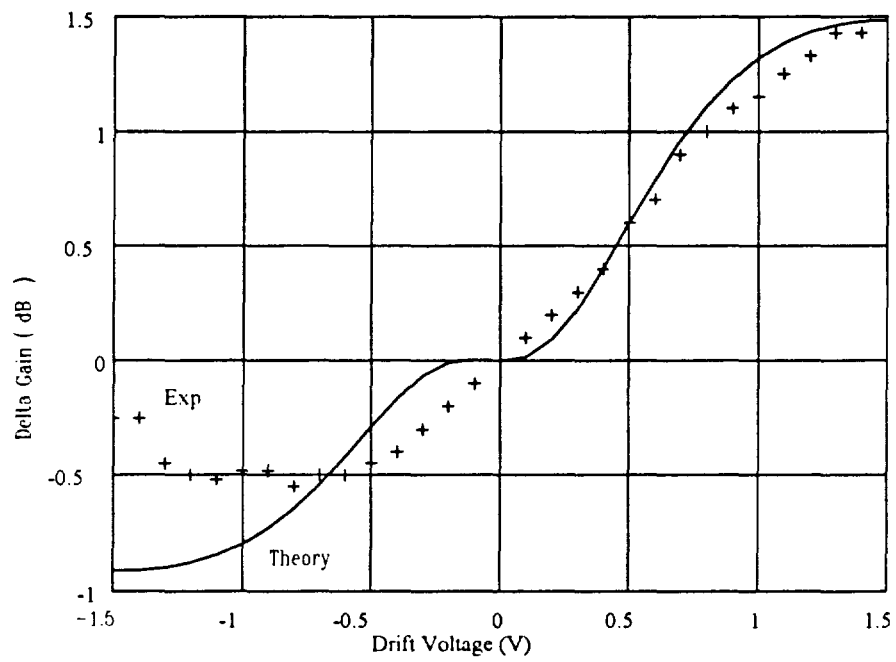


**Figure 4.5:** Measured gain (+++) compared to theory (solid) for device AE05 on the 1.1  $\mu\text{m}$  layer doped at  $5 \times 10^{15} \text{ cm}^{-3}$ .



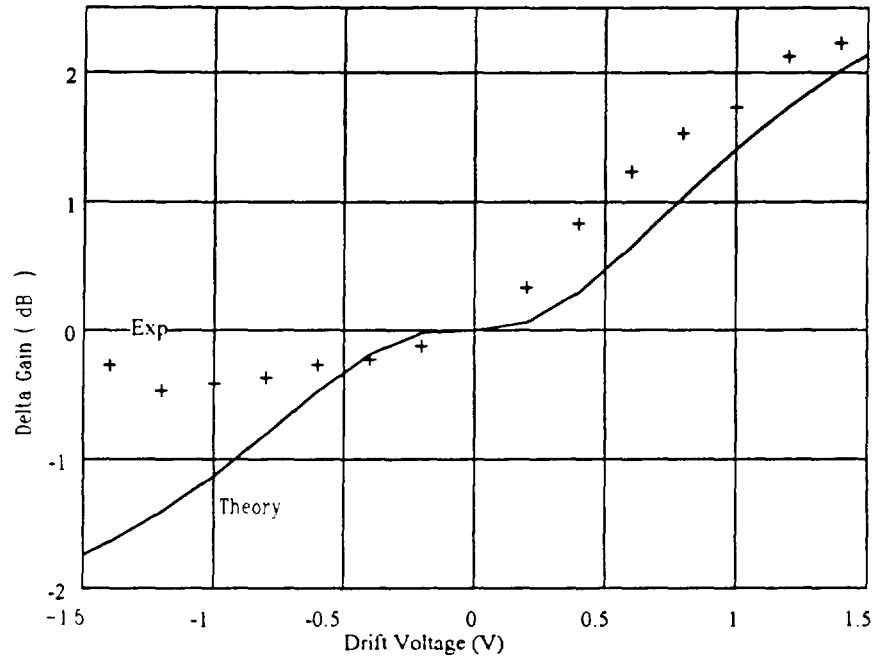


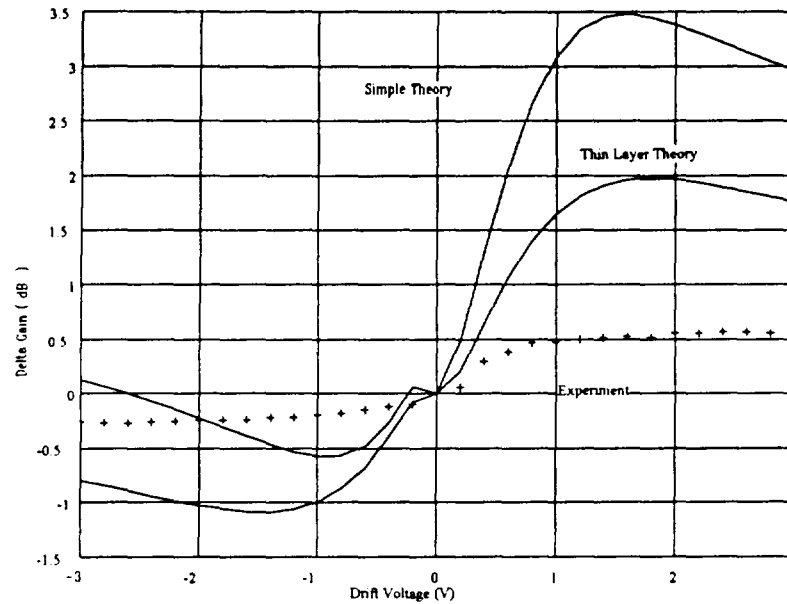
**Figure 4.6:** Measured gain (+++) compared with theory (solid) for device AE06 on the  $1.1 \mu\text{m}$  layer doped at  $5 \times 10^{15} \text{ cm}^{-3}$ .

#### SAWAMP Gain Measured for Devices on Thin Layers

Based on the curves of Figure 3.2, it was anticipated by the author that a  $1000 \text{ \AA}$  charge confinement layer would provide similar gain at lower power dissipation. Devices

were fabricated on a  $0.8\text{ }\mu\text{m}$  layer using mask AE2. Because of the extremely high resistance of this sample, it was necessary to photo-generate carriers. The ambient light of the room was sufficient to bring the resistivity into the  $1\text{M}\Omega/\text{sq}$  range. The gain of device AE207 is compared to theory in Figure 4.7. There were 10 devices on this sample, all of which had a maximum gain within 0.05 dB of this sample. Although the power dissipation was extremely low (15 mW), the gain was far below what was predicted. It was observed that the current saturated at approximately 1 V due to the low free carrier concentration, which accounts for the flatness of the gain curve at high voltage, but this does not explain the reduced gain of these devices. From this experiment, it was postulated that there will exist a layer thickness below which the SAWAMP would not operate properly. Devices with a layer thickness much less than a Debye length have been treated theoretically in [22] and a slight reduction in maximum gain was predicted. This model has been implemented and the curve has been compared to the simple theory and experimental data in Figure 4.7. This theory gives a better approximation for thin layers than the simple theory, but it still does not explain the experimentally observed behavior.

**Figure 4.7:** Measured gain (+++) compared with simple theory (solid) and thin layer theory(---) for device AE207 on the  $0.8\ \mu\text{m}$  layer doped at  $5 \times 10^{15}\ \text{cm}^{-3}$ .



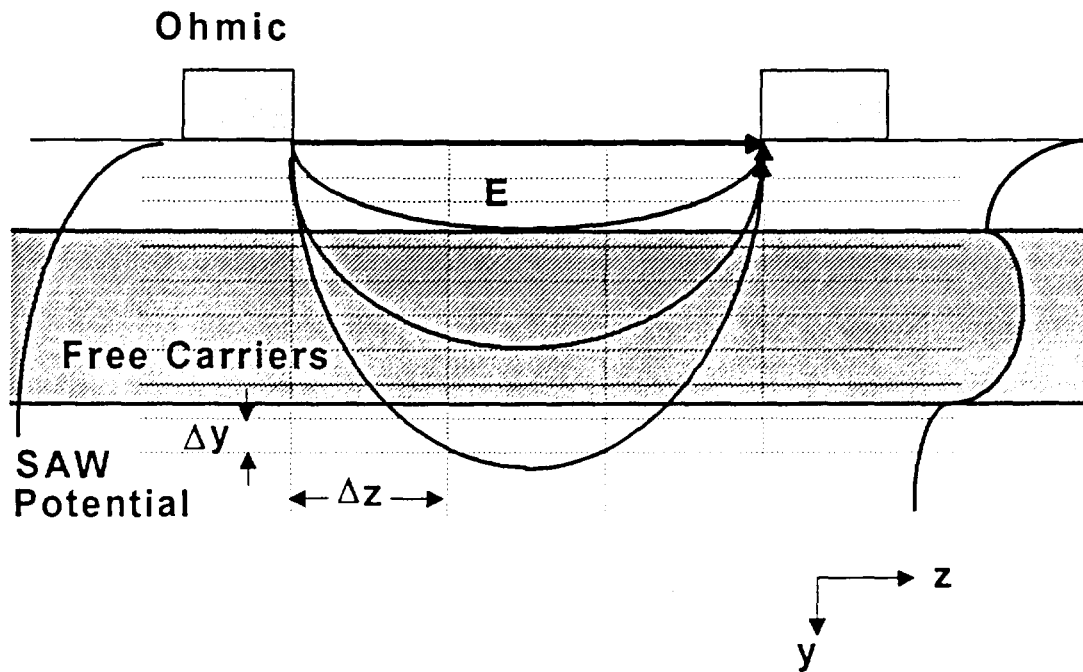
A two-dimensional treatment first reported by Hsu and White [23] has been modified here to give an acceptable explanation of this phenomenon. It has been developed by the author in the next section and compared to experimental findings.

### Two-Dimensional Analysis of a Segmented SAWAMP

The two-dimensional theory for the segmented SAWAMP was developed by Hsu and White [23], assuming a bulk doped substrate with uniform charge distribution and an exponentially decaying SAW potential into the depth of the substrate. Here, this model has been modified by the author, substituting a more accurate SAW potential profile and an approximate charge density profile into the depth of the substrate, which is necessary for the epitaxial material structure.

The operation of the model has been illustrated in Figure 4.8 for a single segment. First of all, consider the variation of the electric field into the depth of the substrate. Because the electrodes are on the surface of the substrate, the field demonstrates fringing behavior in the material. The SAW only interacts with the component of the electric field in the direction of propagation  $E_z$ , (where  $z$  has been defined in the coordinate system illustrated in Figure 4.8) so that the effective interaction length varies into the depth. In addition, the charge in this device is confined in the  $y$  direction as illustrated by the shaded rectangle, limiting the interaction between the SAW and  $E_z$  to this region.

**Figure 4.8:** Simplified diagram illustrating how dividing a segment into 2-D sections accounts for the variation of the electric field and charge distribution on the SAWAMP gain.



electric fields were uniform into the depth, the potential function would merely be scaled according to the amplification factor as it passed through the segment. However, because the charge is laterally confined to a layer, the gain only acts on part of the potential function, immediately explaining the phenomenon of reduced gain for very thin layers of charge. By dividing the segment into a 2-D grid, the gain has been calculated for each

section using the simple model and summed to give the overall gain of the segment as has been shown on the following formulation.

### Electric Field Formulation

The problem of finding the electric field distribution under an array of surface electrodes like an IDT was rigorously treated by Joshi and White in [24]. Their solution was expressed in terms of an infinite series of trigonometric functions, which can in some cases be truncated to the first term. The original derivation was for periodic finite arrays of surface electrodes, but proved to be a good approximation for non-periodic arrays in the work of Hsu and White [23].

Following the formulation of Hsu and White [23], the electric field can be expressed as,

$$E_z(z,y) = \begin{cases} E_o \cos\left(\frac{\pi z}{p}\right) e^{\frac{m\pi y}{p}} & \text{for } -L' \leq z \leq L', y \leq 0 \\ 0 & \text{for } -\frac{p}{2} \leq z < -L', -L' < z \leq \frac{p}{2}, y \leq 0 \end{cases} \quad (4.2)$$

where

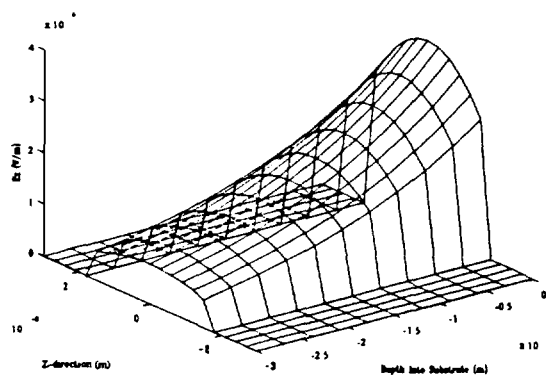
$$E_o = E_z(0,0) = \frac{\pi V_o}{2p} \frac{1}{\sin\left(\frac{\pi L'}{p}\right)}, \quad (4.3)$$

$$m = \left(\frac{\epsilon_{11}}{\epsilon_{33}}\right)^{\frac{1}{2}}, \quad (4.4)$$

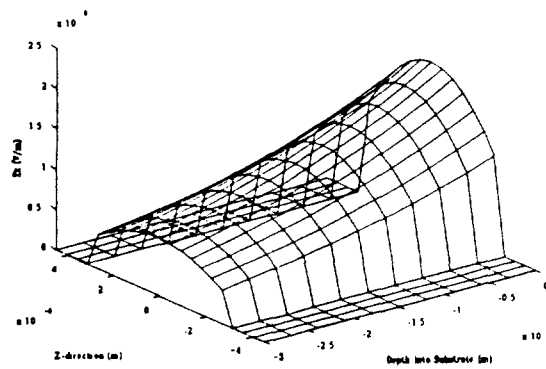
and  $V_o$  is the applied voltage,  $p$  is the period of the electrodes and  $L'$  corresponds to either  $L_1$  or  $L_2$  depending on which segment is being considered.

Plots of the two-dimensional amplitude of  $E_z$  have been compiled in Figure 4.9 for an ohmic width of  $3\text{ }\mu\text{m}$  and four different segments lengths of  $3\text{ }\mu\text{m}$ ,  $6\text{ }\mu\text{m}$ ,  $12\text{ }\mu\text{m}$  and  $60\text{ }\mu\text{m}$  with an applied voltage of  $1\text{ V}$ . The coordinates are such that  $z=0$  is in the center of the segment,  $y=0$  is at the surface with the negative  $y$ -direction into the substrate. As may be observed, the shorter segments have a much larger variation in the profile of  $E_z$  particularly into the depth of the material. For the shortest segment, the amplitude of  $E_z$  drops by almost a full order of magnitude in the first  $3\text{ }\mu\text{m}$  or quarter wavelength into the depth. As illustrated in Figure 4.9 this effect becomes less evident as the segment length increases. For the  $60\text{ }\mu\text{m}$  segment the field appears almost uniform into the depth for the first  $3\text{ }\mu\text{m}$ .

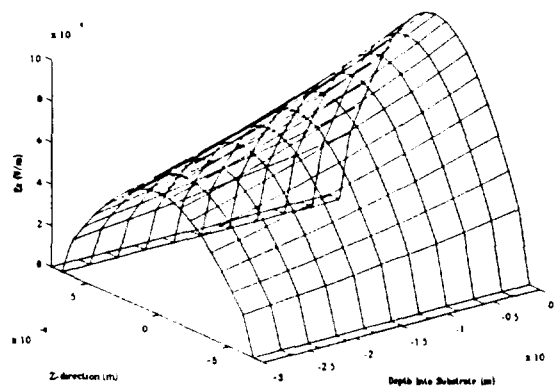
Now, given that the velocity of the drifting carriers is directly proportional to the drift field this shows that the initial assumption of constant drift velocity in the segment is not valid, particularly in short segments. This leads to the observation that even in a substrate with constant carrier concentration, the gain is not constant in a segment due to the variation in drift velocity both with depth and propagation direction.



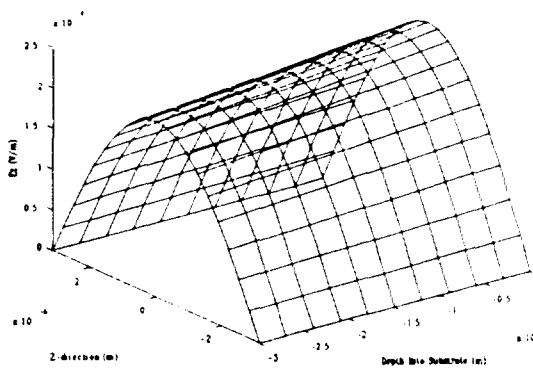
(a)



(b)



(c)



(d)

**Figure 4.9** Two-dimensional plots of the amplitude of  $E_z$  in segments with  $3\ \mu\text{m}$  wide ohmics and segment lengths of (a)  $3\ \mu\text{m}$ , (b)  $6\ \mu\text{m}$ , (c)  $12\ \mu\text{m}$  and (d)  $60\ \mu\text{m}$ .



This exercise of plotting the electric field curves points out that the electric field is maximum on the surface, so it is best to have charge near the surface for maximum gain. In addition, the shorter the segments, the more variation there is in the electric field. From this argument, it appears that long segments with the semiconductor on the surface of the piezoelectric substrate would be the optimum configuration.

### SAW Potential Profile

In [24], it was assumed that the SAW potential could be approximated by an exponentially decaying function for simplicity. Here, a simulation based on the Laguerre polynomial technique has been used by the author to give a more accurate representation of the SAW potential. The Laguerre polynomial was first applied to solve the SAW potential problem by Datta [25] and has recently been extended to multilayer material structures by Kim and Hunt [26]. The advantage of the Laguerre polynomial technique is that the tensor problem may be reduced to a set of linear equations which is readily solved in a non-iterative manner. The SAW potential profiles used here have been computed using Kim's implementation in a program called ASIMM.

The SAW electric potential profile into the depth of a {001}-cut GaAs substrate with SAW propagation in the  $\langle 110 \rangle$  direction on a free surface as predicted by ASIMM has been plotted in Figure 4.10. The SAW potential decays into the depth, approaching zero at approximately one wavelength, but is not a simple exponential function. The

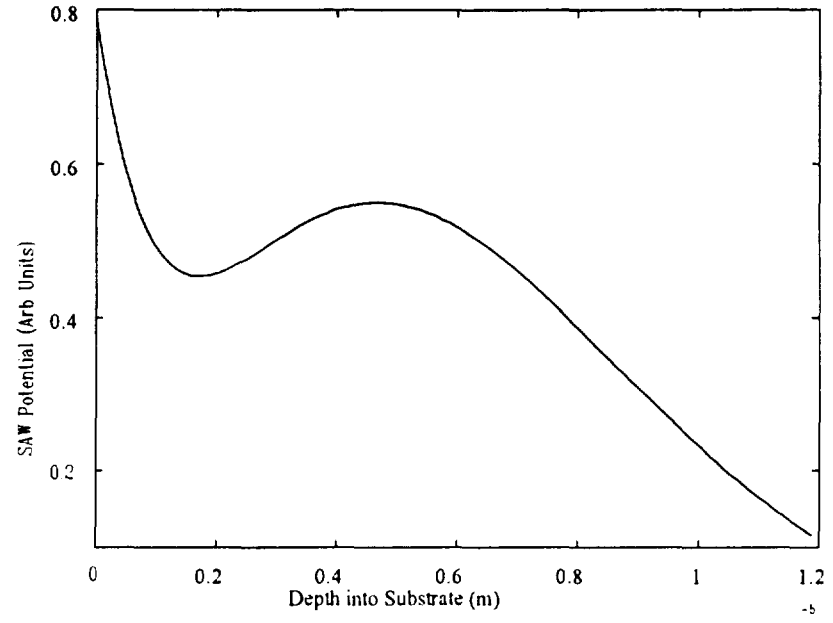


**Figure 4.10:** SAW potential profile into the depth of a {001}-cut GaAs substrate with SAW propagation in the  $\langle 110 \rangle$  direction as predicted by ASIMM.

potential for a shorted surface is very similar but the potential goes to zero on the surface.

### Gain Formulation

Following the treatment of [24], the SAW potential has been labeled  $P(z,y)$ . The profile plotted in Figure 4.10 represents the profile as it enters the SAWAMP segment,  $P(-p/2,y)$ . Now, within each rectangular section, the gain is essentially uniform so the incremental gain may be written:

$$P(z + \Delta z, y_i) = P(z, y_i)e^{-\alpha \Delta z} \quad (4.5)$$

where  $\alpha$  is the attenuation constant of equation (2.8)..

The gain through each column of the  $\Delta z$  sections is calculated iteratively from the preceding column so that the change in the SAW potential through an entire segment is easily calculated. The gain for a segment is then defined as the difference in the SAW potential entering and leaving the segment

$$G = 20 \log_{10} \left[ \frac{\sum_{i=1}^{N_y} P(\frac{p}{2}, y_i)}{\sum_{i=1}^{N_y} P(-\frac{p}{2}, y_i)} \right] \quad (4.6)$$

where  $N_y$  is the number of divisions in the y-direction.

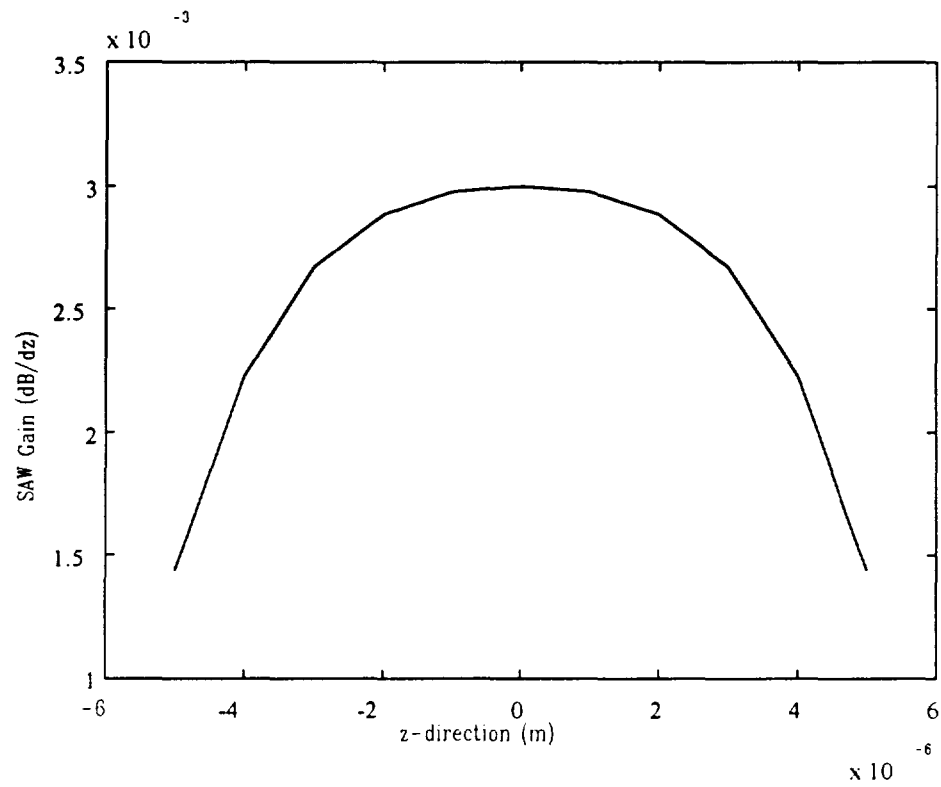


**Figure 4.11:** Gain per  $\Delta z$  over the length of a  $10 \mu\text{m}$  long segment on a GaAs substrate uniformly doped at  $5 \times 10^{13} \text{ cm}^{-3}$  an applied voltage of 1V.

Using this formulation, the gain per unit length for each  $\Delta z$  section over the length of a 10  $\mu\text{m}$  long segment on a GaAs substrate uniformly doped at  $5 \times 10^{13} \text{ cm}^{-3}$  with unity applied voltage is plotted in Figure 4.11. For this case the segment was divided into 10 section in the z-direction and 26 sections in the y-direction. As expected from the electric field plots, the gain is not uniform over the entire segment, but is reduced near the ends of the segment. From this plot it may be deduced that the SAW amplitude does not increase linearly with distance as was originally assumed in the simple formulation. Curves of SAW amplitude change over the length of the segment have been compiled for applied voltage ranging from 0.2 to 1.0 V in Figure 4.12. At the lowest voltage, there is actually loss at some points along the curve where the electric field is at its minimum. As expected the gain increases for applied voltage, but it is more interesting to observe how the linearity of the change in SAW amplitude varies with applied voltage. At high voltage, the curve was nearly linear, making the assumption of constant gain along the length of the segment valid. At lower voltage, this assumption does not hold true.

### Comparison to Experiment

This model was applied to the devices AE05 and AE207 presented in Figures 4.5 and 4.7, assuming a rectangular charge distribution into the depth of the substrate. The model is compared to the data for AE05 in Figure 4.13. The two-dimensional model shows slightly better agreement to the data than the simple model in both the forward and

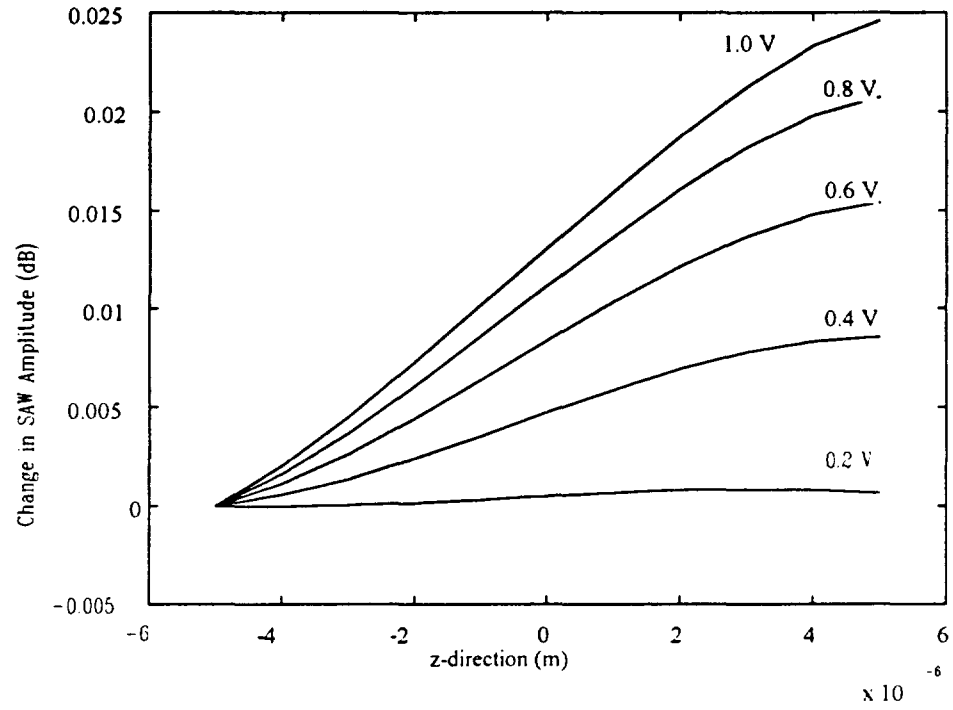


**Figure 4.12:** Change in SAW amplitude over the length of a  $10\ \mu\text{m}$  long segment on GaAs uniformly doped at  $5 \times 10^{13}\ \text{cm}^{-3}$  with applied voltage ranging from 0.2 to 1.0 V.

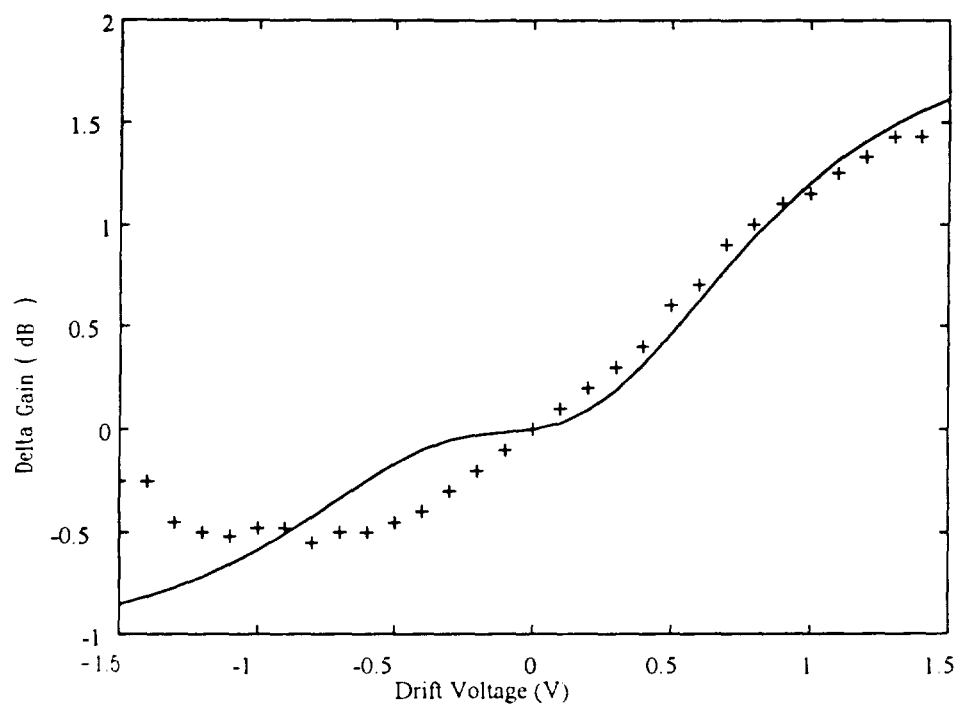


**Figure 4.13:** Comparison of the two-dimensional model (solid line) to the measured data (+) for device AE05.

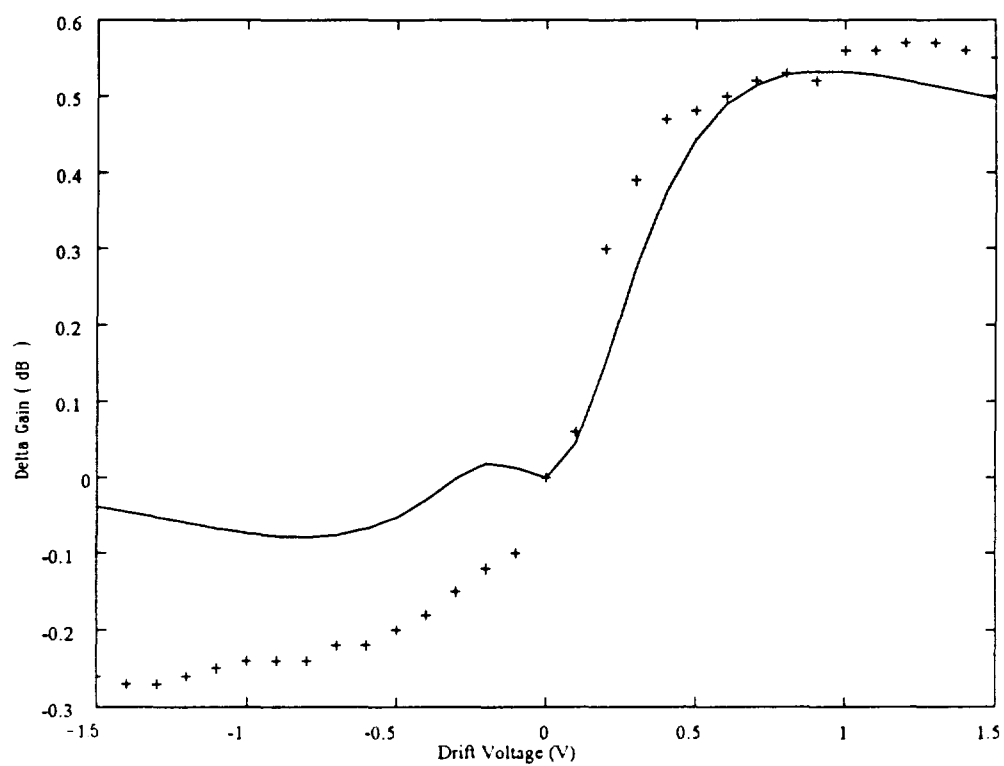


**Figure 4.14:** Comparison of the two-dimensional model (solid line) to the measured data (+) for device AE207.



reverse directions, but still does not account for the reverse direction behavior. It may also be observed that the inflection of the predicted curve is not evident in the data which indicates that the L2 sections may have even less of an effect on the gain of the device than predicted by the two-dimensional model.

The two-dimensional model which has been developed by the author for segmented SAWAMPs on epitaxial material structures, is a great improvement over the simple model for the thin layer device as shown in Figure 4.13. The two-dimensional model matches the experimental data for AE207 much more closely than either the simple model or the thin-layer model displayed in Figure 4.7 in both the forward and reverse directions, even though there is still a large discrepancy in the reverse direction.

The behavior in the reverse direction will not be explored further here. However, this asymmetric gain curve has been observed since the first reported acoustoelectric amplifier was reported and has been studied in previous publications. Several possible explanations have been presented including non-uniform electric fields [27], trapping effects [28] and non-uniformities in the material [29].

A further experiment was carried out to further investigate the effect of the charge layer on the gain of the SAWAMP using a light source to alter the conductivity of the substrate. The experiment was carried out on device AE216 which had been fabricated on a sample with a 9500 Å thick layer. This layer thickness had been determined to be the optimum for power dissipation and maximum gain in Chapter 3. However, similar to the

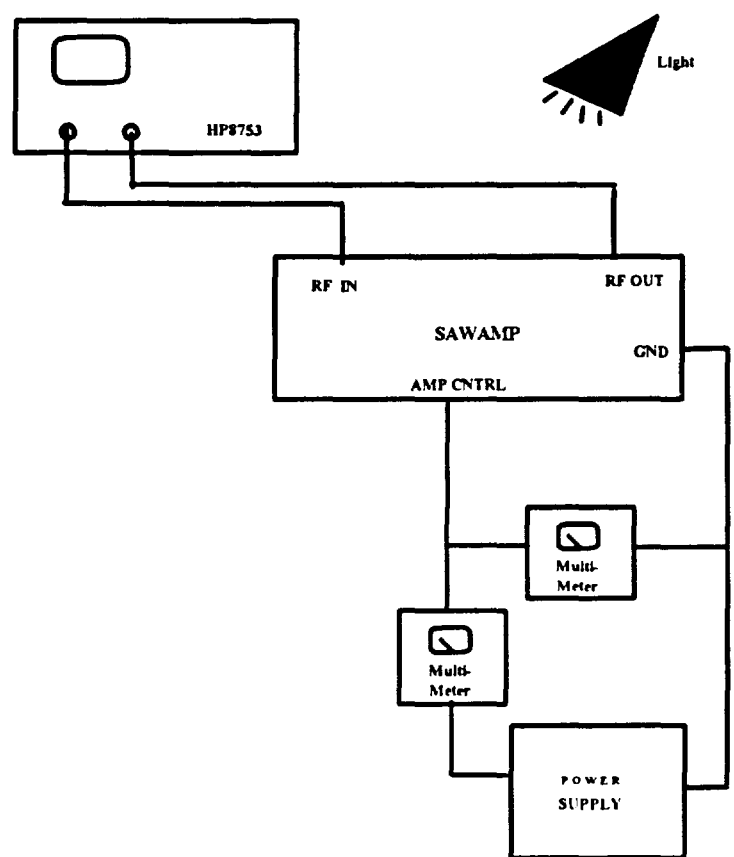
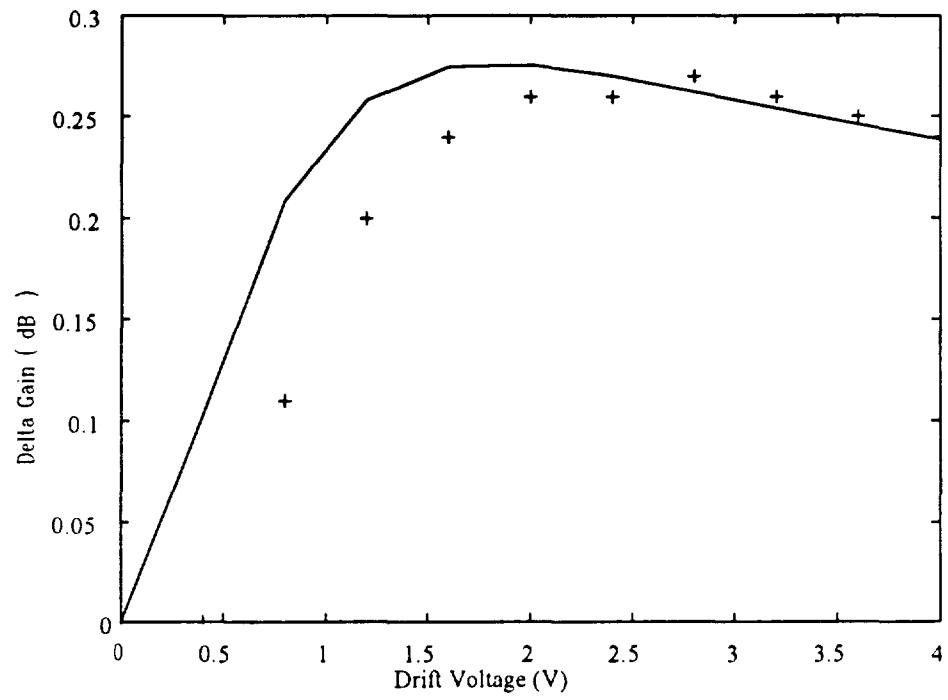


Figure 4.15: Test setup for layer thickness versus gain measurement.

previous experience with thin layers, the measured gain on all of the devices on this sample was lower than expected.

The experimental setup is shown in Figure 4.15.  $S_{21}$  was measured using the HP8753 network analyzer as before. There was a power supply to control the applied voltage to the amplifier and two multimeters. One multimeter was used to measure the resistance on the ohmic contacts for an applied light intensity with the power supply turned off and to measure the applied voltage during the experiment. The other multimeter was used to measure the current through the ohmics during the experiment. Gain measurements taken for four different light intensities are compared to the two-dimensional model in Figures 4.16 through 4.19. Only the forward voltage was considered in this experiment.

The measurements are labeled by the resistance which was measured on the multimeter at the given light intensity as  $R=15, 40, 200$  and  $400\Omega$ . For  $R=400\Omega$ , the device was in the dark and for each of the others the light was intensified to increase the free carrier concentration. Using HETMOD as a guide, the layer thickness and carrier concentration were fitted to the measured resistance. For simplicity, the carrier concentration was assumed to be a rectangular function and these values were plugged into the two-dimensional model. The values of  $n = 1 \times 10^{13} \text{ cm}^{-3}$  and  $d = 1000 \text{ \AA}$  were used for  $R = 400 \Omega$ . For  $R=200 \Omega$ , the value of  $n$  was doubled to  $2000 \text{ \AA}$ . For  $R = 40 \Omega$  and  $15 \Omega$ , values of  $n = 5 \times 10^{13} \text{ cm}^{-3}$  and  $d = 3500 \text{ \AA}$ , and  $n = 1 \times 10^{14} \text{ cm}^{-3}$  and  $d = 5000 \text{ \AA}$  were used respectively. Generally, good agreement was found between the model and the



**Figure 4.16:** Experimental gain measurement (+++) compared to the two-dimensional model (solid) for  $R=400\ \Omega$ .

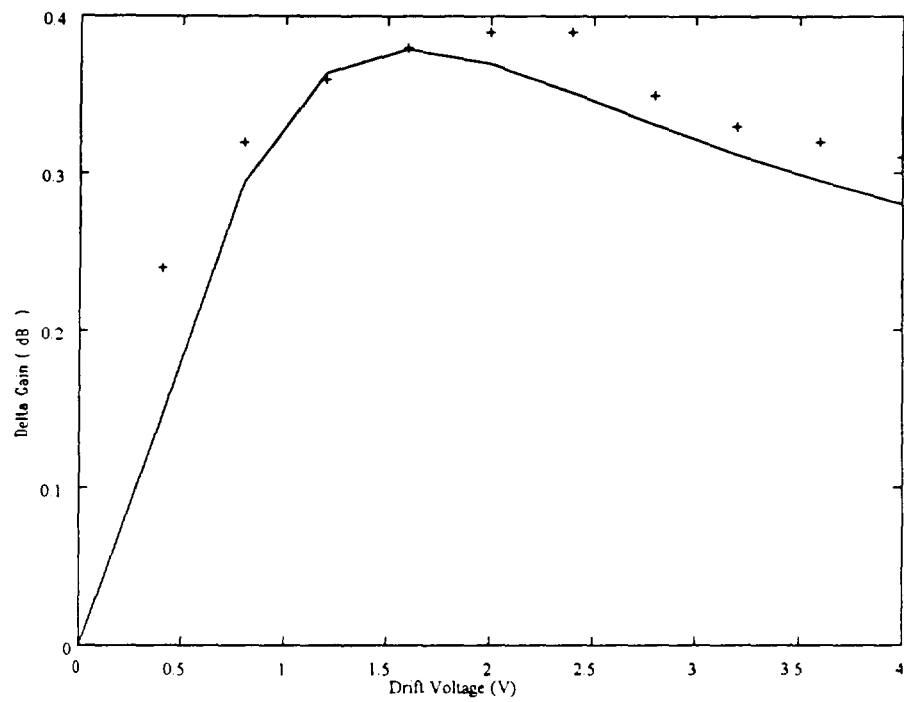


**Figure 4.17:** Experimental gain measurement (+++) compared to the two-dimensional model (solid) for  $R=200\ \Omega$ .

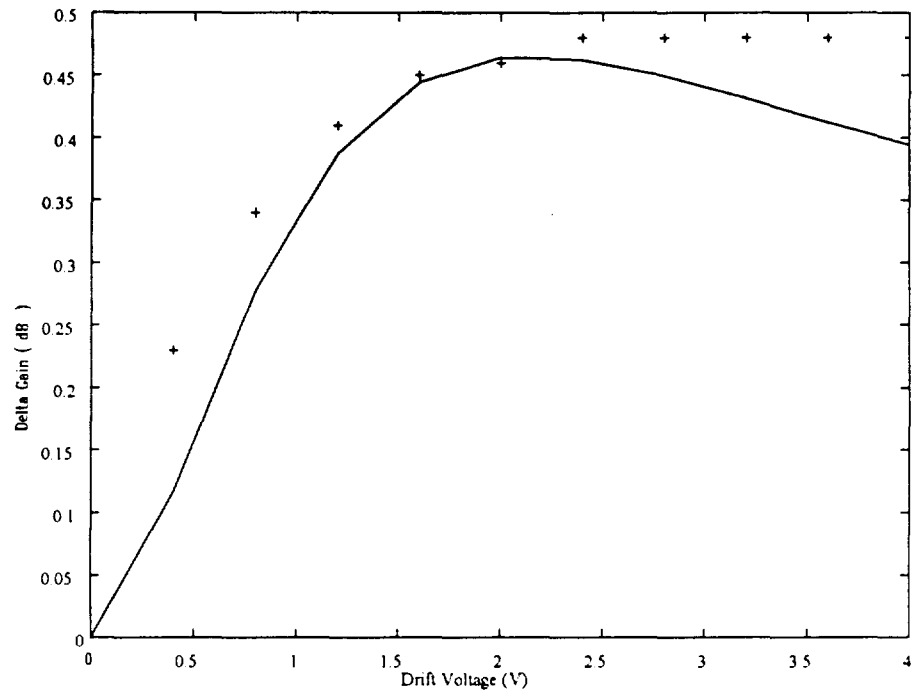


**Figure 4.18:** Experimental gain measurement (+++) compared to the two-dimensional model (solid) for  $R=40 \Omega$ .

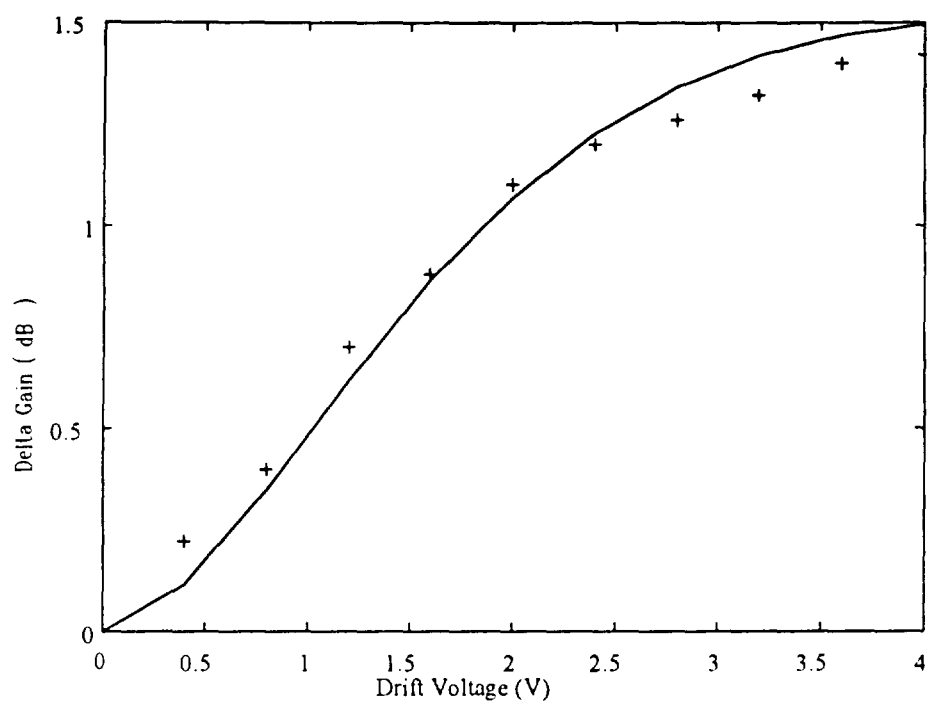


**Figure 4.19:** Experimental gain measurement (+++) compared to the two-dimensional model (solid) for  $R=15\ \Omega$ .

measurement for each case. The model gives good agreement with the data for all four cases, and gives some insight into the operation of the SAWAMP on thin layers.

To summarize, the development of the two-dimensional model and experimental measurements conducted here have shown that the electric field distributions have an appreciable effect on the performance of the device, but what is more important, is the thickness of the interaction layer. As one may intuitively conclude, the thicker the layer, the higher the gain of the amplifier. The material requirements of a thick layer and high resistivity are somewhat at odds. As previously determined, the lowest power dissipation requires a thin, lightly doped layer. To attain the highest gain a thick layer is required doped at approximately  $5 \times 10^{13} \text{ cm}^{-3}$ . This may not be practically realized, as it is difficult to control the growth of material at such a low donor concentration. The approach taken in this thesis to achieve the desired carrier concentration relied on the thinning of the layer to achieve the low carrier concentration. This dilemma will be left for further investigation, but at this time it is the opinion of the author, that the device may still be practical by achieving a balance between the dissipated power and the gain. It may not be necessary to attain maximum gain, but rather optimum gain taking all factors into account, particularly if a gain enhancing piezoelectric film is employed.



### Power Reduction Techniques

As shown above, the layer thickness may be modified with an etch to give a higher resistance resulting in a lower power dissipation. Another technique to reduce power consumption is to reduce the aperture of the amplifier, which will give a linear reduction in power dissipation with narrowing aperture. As demonstrated in the previous section, there is a limit to how thin the layer can be taken. Also the aperture of the device is limited by diffraction effects on the propagating SAW.

An effective method of reducing the excessive power dissipation developed in this thesis was to make the L2 section inactive to both the dc field and the SAW interaction. Recalling the sheet resistance versus layer thickness curve of Figure 3.4, the sheet resistance follows an exponential type of curve and below approximately  $0.5\text{ }\mu\text{m}$ , the layer is fully depleted. This indicates that the entire layer need not be removed to make the L2 sections inactive. It was estimated that as little as  $2000\text{ }\text{\AA}$  was sufficient to produce a significant power reduction.

This was accomplished by using an etch to isolate the active regions of the device as illustrated in Figure 4.20. The L1 regions were masked and the entire wafer etched approximately  $2000\text{ }\text{\AA}$  to make the epi-layer highly resistive everywhere except in the L1 regions.

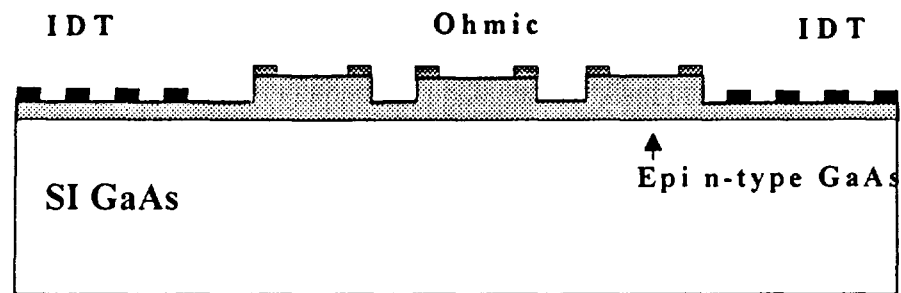


**Figure 4.20:** An etch is used to isolate the active regions.

**Table 4.3** Resistance measurements for device AE213 for 2 etch depths

Etch Depth ( $\text{\AA}$ )	Resistance (ohms)
0	450
1,700	860
2,200	1,060

This experiment was carried out by the author on the 9500 Å sample discussed above. A large sample on which the ohmic contacts had been deposited was cleaved into three pieces, one of which was left unchanged. The other two were etched as described using the  $\text{HP}_4\text{O}_3$  etching solution. The ohmic metal was deposited before the L1 areas were masked to aid alignment, but anneal step was left until after the etch as it was unknown how the diffused gold would affect the etching of the GaAs. The IDTs were added as the final step as per the usual process.

Resistance measurements across the ohmics are compared in Table 4.3 for device AE213 on the three samples in the dark. From these measurements, it would appear that a 2.5 times reduction in power dissipation from the 2200 Å etch. If the L2 sections were completely removed, a 6 times reduction was expected. Measurements on the three devices showed no observable difference in signal quality or in the gain curve. It was anticipated that a higher gain would be achieved by removing the L2 sections, but this supports the hypothesis derived earlier from the two-dimensional model, that the L2 sections have less contribution on the gain curve than is theoretically predicted. This could be attributed to the short length of the L2 sections and that perhaps the field penetration into the depth is even less than predicted for these short sections.

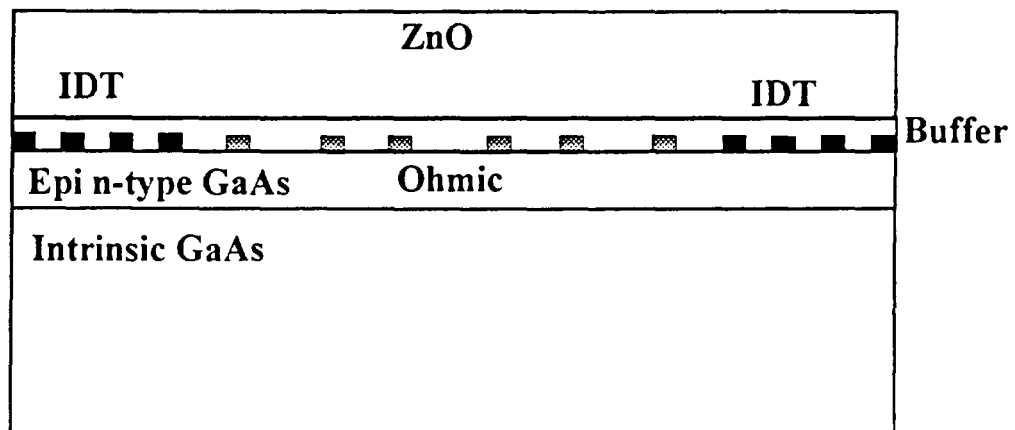
This power reduction technique looks very promising, but requires further investigation into the effects of deeper grooves. It is the opinion of the author, that the use of an ion implant would be a superior technique as all of the current through the L2

section could be eliminated with very little surface perturbation, so there would be no tradeoff between power dissipation and reflections.

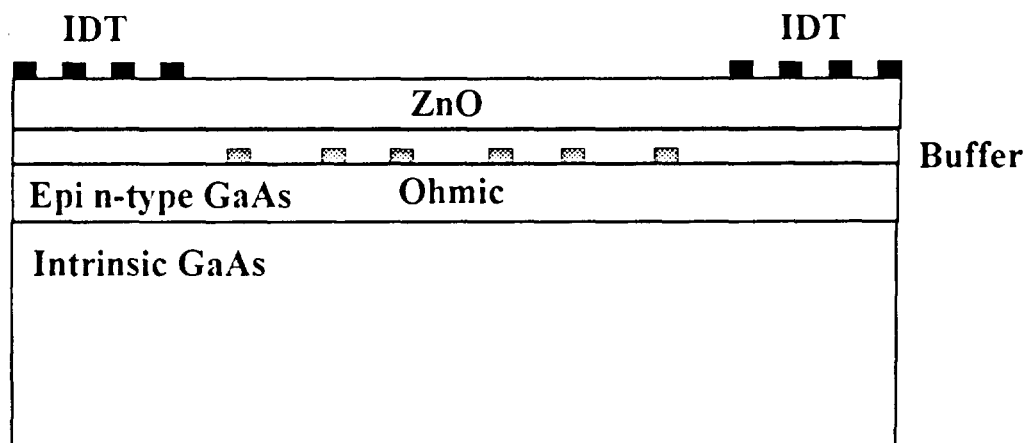
### Addition of a Piezoelectrically Active Layer

From equation (2.8) it was inferred that the gain of a SAWAMP was directly related to  $K^2$ . The SAWAMPs which have been reported in this chapter have had low gain due to the low value of  $K^2$  for GaAs, but these devices could be improved with the addition of a layer with a larger  $K^2$ . There are several materials which could be used as a piezoelectric film but Hickernell [30] has reported that the best acoustic match for GaAs is ZnO. These films have been well studied and it appeared that this would be a simple matter of having films deposited over existing SAWAMP structures.

Using the ASIMM simulator, the SAW potential was modeled for several ZnO thicknesses to determine the best architecture. There are two possible configurations for the IDT as shown in Figure 4.21. In both configurations, there is a buffer layer of  $\text{SiO}_2$  between the GaAs and the ZnO to prevent cross doping of materials. The difference comes in the placement of the IDT. In the thick layer configuration the IDT must be at the interface, but  $K^2$  values as high as 3% are possible [30]. The only disadvantage of this approach is that the peak  $K^2$  value occurs at a ZnO thickness of approximately  $0.5 \lambda$ . In this case the ZnO layer thickness would be  $6 \mu\text{m}$ , which is difficult to achieve in practice, because of problems with the deposition of such thick films. With the IDT on top, a



(a)



(b)

**Figure 4.21:** Two configurations for IDT position on GaAs/ZnO device: (a) IDT at interface and (b) IDT on top of ZnO.

maximum value of  $K^2 = 0.9$  is possible [30], but a thinner  $1.5 \mu\text{m}$  ZnO layer would be sufficient.

Simulations were performed using ASIMM and the two-dimensional model to determine the gain that could be achieved for both configurations. The ASIMM curves for SAW potential into the depth of the substrate have been plotted for film thicknesses ranging from 0 to  $6 \mu\text{m}$  in Figure 4.22. In each case zero depth refers to the top surface of the ZnO and as the layer thickness increases the interface between the ZnO and the GaAs occurs deeper into the depth. The position of the charge confinement layer has been indicated with arrows for each case. For example, for the  $1 \mu\text{m}$  film, the charge layer occurs about  $1.5 \mu\text{m}$  from the surface of the top surface of the ZnO. In the  $2 \mu\text{m}$  film, the charge layer occurs at  $2.5 \mu\text{m}$  from the ZnO top surface and so on. In each case the SAW potential has been normalized to 1mW of acoustic power per 1 mm of acoustic aperture [26].

The first case considered was the device of Figure 4.16 with the addition of a  $1 \mu\text{m}$  overlay of ZnO. A value  $K^2 = 0.3$  was used here based on data from Yamanouchi [31]. The predicted gain increased by approximately a factor of 5 as shown in plotted in Figure 4.23. The case of the thicker conductive layer as in the device of Figure 4.19 with the addition of the  $1 \mu\text{m}$  ZnO overlay was plotted in Figure 4.24. In this case a 3 times improvement was achieved over that on GaAs. This difference in improvement factors was not only related to the width of the charge confinement layer, but also to the overall shape of the

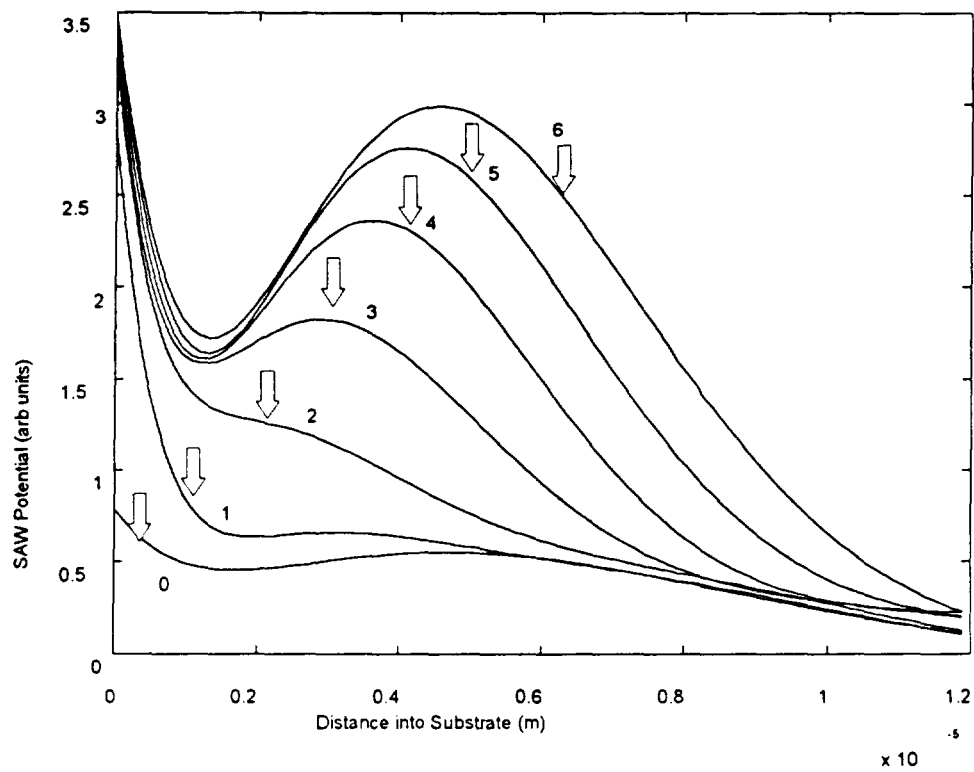


**Figure 4.22:** SAW potential into the depth of the substrate for ZnO layer ranging from 0 to 6  $\mu\text{m}$  thick.

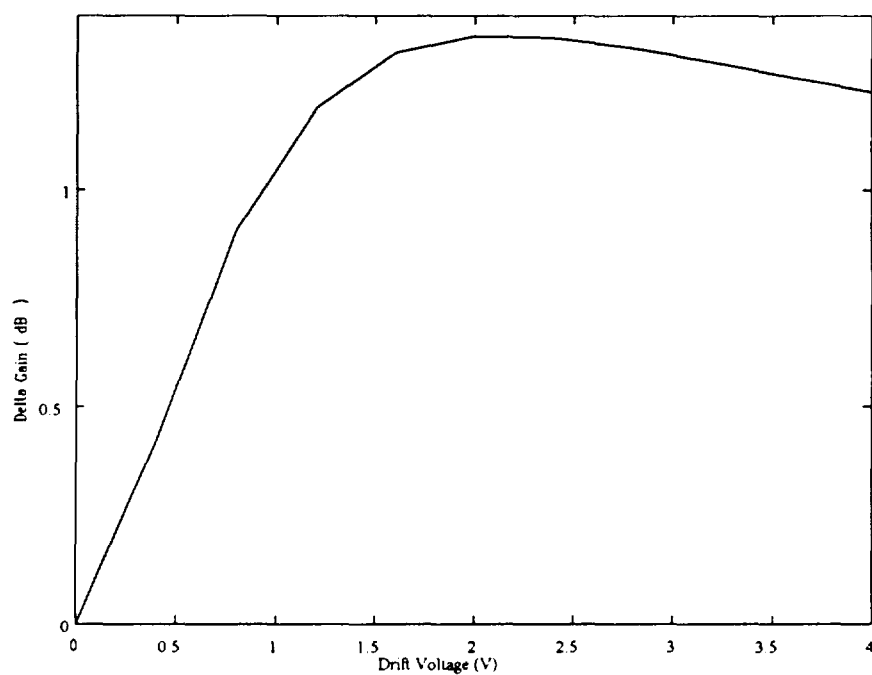


**Figure 4.23:** Predicted gain curve for the device of Figure 4.16 with a 1 μm ZnO overlay



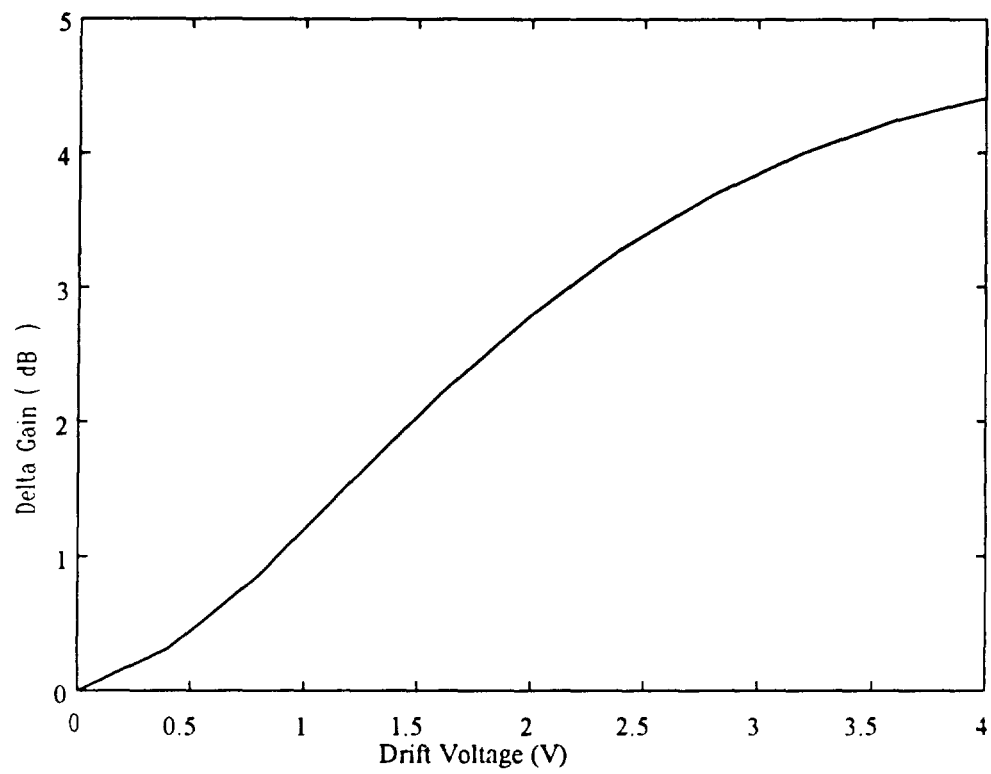


**Figure 4.24:** Predicted gain curve for the device of Figure 4.19 with a 1  $\mu\text{m}$  ZnO overlay.

SAW potential curve. This was further emphasized by conducting the same calculations for ZnO thickness ranging from 0 to 6  $\mu\text{m}$ . The values of  $K^2$  taken from Yamanouchi [31] for each layer have been recorded in Table 4.4. The gain curves did not appear to change significantly for change in the ZnO thickness, but the peak gain values varied greatly as plotted in Figure 4.25. The curves plotted are the peak gains calculated for each case, normalized to dB/cm, which is the metric used to compare SAWAMPs. To determine the peak gain not only does  $K^2$  need to be considered. As demonstrated by the author, the width and position of the charge confinement layer, and the shape of the SAW potential curve must all be considered when determining the gain. It was observed from the plot of Figure 4.25, that the peak gain decreases above the 5  $\mu\text{m}$  ZnO film thickness. Although  $K^2$  is larger for a 6  $\mu\text{m}$  film than a 5  $\mu\text{m}$  film, the peak in the SAW potential curve no longer coincides with the charge confinement layer as shown in Figure 4.22. In this case the impact of the gain is less than that of the thinner ZnO layers.

Overall, this exercise indicated that very high gain may be achieved with the ZnO overlay. The maximum gain will be achieved for a 5  $\mu\text{m}$  layer of ZnO. Even at a very low power dissipation of 15 mW for the device with the 1000 Å charge layer, a gain of 20 dB/cm was predicted. For the 5000 Å charge layer, as much as 120 dB/cm is predicted but the power dissipation would increase.

The ZnO overlays were experimentally investigated. Several quarter wafers were sent out for ZnO deposition as the capability was not available in-house. ZnO layers were grown, with thicknesses ranging from 3 to 6  $\mu\text{m}$ . Some difficulties were experienced with

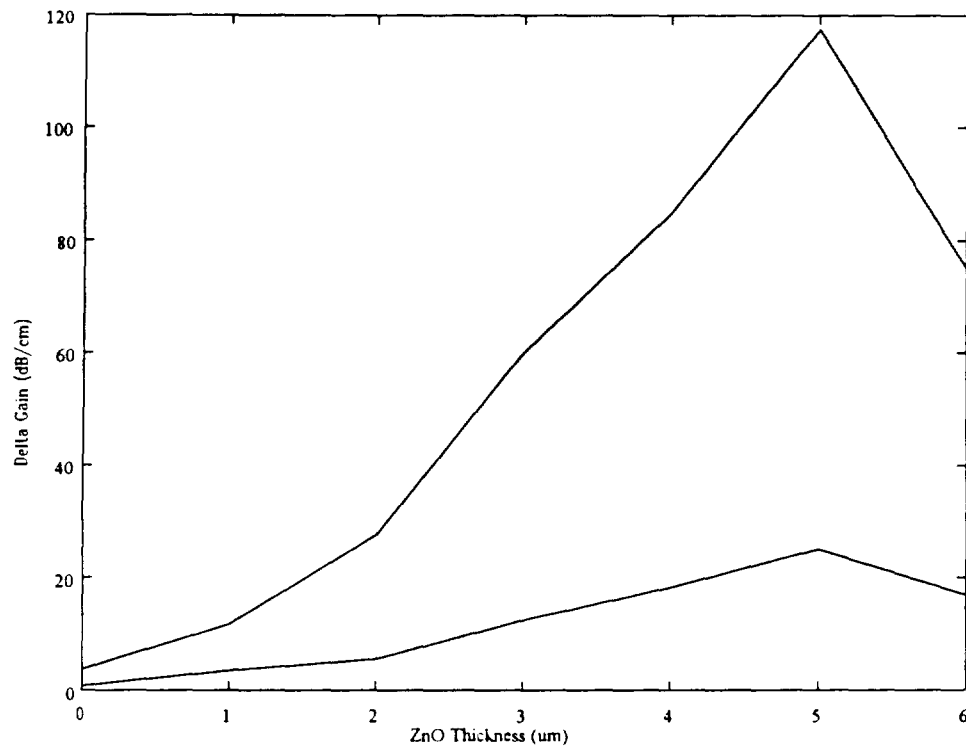


**Figure 4.25:** Peak normalized gain for device for the devices of Figure 4.16 (lower) and 4.19 (upper) versus ZnO thickness.

**Table 4.4:** Value of  $K^2$  for ZnO Layers

ZnO Thickness ( $\mu\text{m}$ )	$K^2$ (%)
0	0.07
1	0.3
2	0.8
3	1
4	1.4
5	1.8
6	2

the deposition. Initially, films were grown using the supplier's standard process. The best quality films are deposited at a temperature in excess of 350 °C, which was found to diffuse the Au in the ohmic contacts into the GaAs. It also had a negative effect on the Al in the IDTs, making the metal highly resistive. The only data which could be gathered from these devices was the center frequency, from S11 measurements. The velocities were approximated from these measurements and were compared to theoretical predictions for an open surface from ASIMM in Figure 4.27. The velocities for all samples were very close to the theoretical values for all samples indicating that the films were of high quality.

The problem was diagnosed by the author as a combination of stress and temperature. The process was changed for subsequent samples lowering, the temperature from to 200°C and attempting thinner films of 1.5 and 2 μm. The lower temperature process produced lower quality films which peeled, so that no devices were obtained

The ZnO experiment were taken no further, however, the critical parameters of the process have been identified. There are approaches which may be taken in the future, given access to the necessary equipment and a dedicated team of material processing personnel. It is thought that the use of a more modern sputtering system, such as an RF magnetron with an ECR or a CVD system, both of which produce lower stress films at lower temperature would make these devices possible. This type of equipment is being used in production lines for TV IF filters using ZnO on glass, so that SAWAMP with a ZnO overlay looks very promising in the future. It is a matter of a focused process development tailored to this structure.

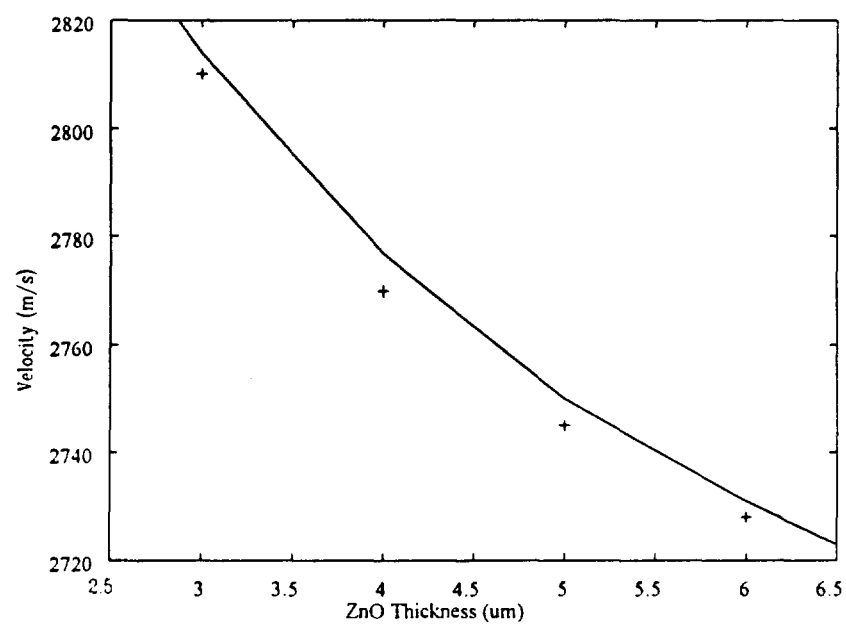


**Figure 4.26:** Measured velocities calculated from center frequency measurements compared to the velocity for an open ZnO/GaAs surface from ASIMM.

### Segmented SAWAMP Summary

In this chapter, the experimental and theoretical exploration of segmented SAWAMPs on an epitaxial layer of GaAs is the first such study ever reported. The author's original hypothesis that low voltage, low power SAWAMPs were possible on a GaAs based structure has been verified. An order of magnitude improvement in both voltage and power requirements over previously reported devices have been experimentally demonstrated here. Devices fabricated and experimentally demonstrated by the author operating at 2 V of applied voltage and dissipating as little as 15 mW are perfectly suited for use in battery operated mobile radio systems. The low voltage requirement was partially due to the small segment lengths reported for the first time in this thesis. The reflections due to these small dimensions has been addressed by the author and these reflections have been minimized in this thesis with the proper choice of ohmic dimensions.

A reduction in the gain was experimentally discovered by the author for devices with charge confinement layers less than 0.5  $\mu\text{m}$ . This effect was theoretically explored by the author by extending the two-dimensional model of Hsu and White, giving good agreement with the observed phenomenon in the positive voltage direction and improved agreement with data in the reverse direction. This model was applied to the case of ZnO overlays to predict the gain for increased  $K^2$ . From these simulations it was evident that the peak gain not only depends on  $K^2$  and the width of the charge confinement layer but

also the position of the layer with respect to the SAW potential. These simulations predicted that as much as 120 db/cm of gain was attainable for a 5  $\mu\text{m}$  layer of ZnO. ZnO overlays were experimentally explored by the author, but process incompatibilities were experienced. However, the author has identified critical process parameters and it is clear that the SAWAMP on ZnO/GaAs can be realized if a process were developed for this device.



## CHAPTER 5

### SLANTED REFLECTION GRATINGS ON GaAs

In the previous chapter, the feasibility of SAWAMPs on GaAs was investigated. The second element necessary for the fully integrated ACT device of Figure 1.1 was an efficient reflector bank, which would enable the SAW to circulate around the loop with a minimum loss. Reflector banks on SAW devices have been well studied and many applications have been derived from the use of both normal and oblique incidence reflectors, including a whole range of low-loss SAW filters and resonators, and reflective array compressors (RACs) to name a few. The filters and resonators were primarily based on normal incidence reflections. RAC devices were based on  $90^\circ$  reflections from a pair of slanted reflector banks, which is the type of device which has been studied here.

As introduced in Chapter 1, an efficient reflector was required to achieve the ring oscillator for the integrated ACT device. The reflector banks not only circulate the energy around the loop, but also define the operating frequency of the oscillator and the bandwidth of the loop. In order to design an efficient loop, it was first necessary to understand the operation of slanted  $90^\circ$  reflectors on GaAs. Although  $90^\circ$  reflectors have

been well studied for the more common piezoelectric substrates such as quartz and  $\text{LiNbO}_3$  [32], there existed no previous experimental study on the behavior of slanted reflectors on GaAs. A theoretical treatment was presented by Danicki and et al [33], with regards to the generation of spurious bulk modes from slanted reflectors on GaAs, and a triple bounce reflector was proposed in order to minimize the SAW conversion to these bulk modes. However, it has been demonstrated here, that the generation of bulk modes using grooves on GaAs appears to be nonexistent, and low loss reflectors have been experimentally demonstrated.

The chapter begins with the theory of slanted reflectors and approximations have been developed which enabled the reflection coefficients for single steps to be experimentally determined. The test structures used here are briefly described and the experiments to determine the reflection coefficients have been described including some second order effects due to multi-reflections. As a result, the reflection coefficients for a single step discontinuity for an Al stripe or a groove have been experimentally determined.

### Theory of Slanted Reflectors

The operation of slanted reflector gratings has been illustrated in Figure 5.1. The SAW is launched by the IDT at the top left. The SAW is partially reflected by each stripe through  $90^\circ$  to the bottom track where the same process takes place to direct the SAW to the IDT at the bottom left. The predominant factors of the array are the stripe period,  $p_z$  and the stripe width,  $a_z$ , and the height of the step,  $h$ . These values not only set

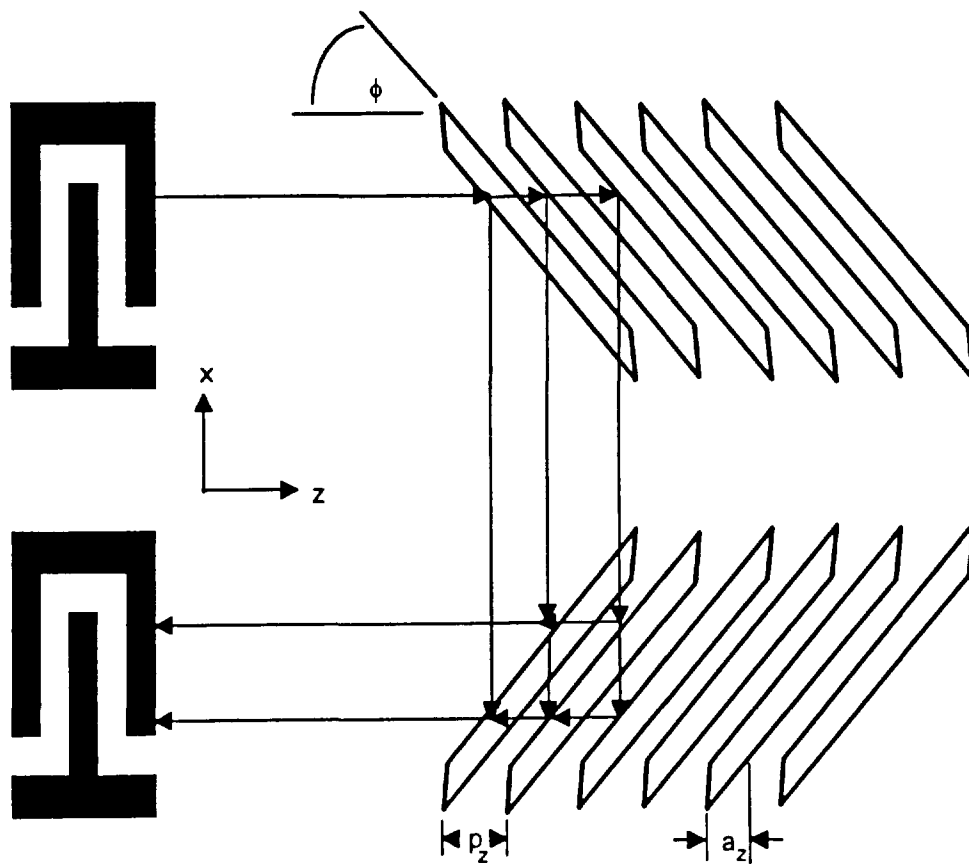


**Figure 5.1:** Schematic illustration of a two slanted reflective arrays.

the synchronous frequency of the array, but also the efficiency of the reflection process.

The angle  $\phi$  must be set individually for a given cut of a material to reflect the waves at 90 degrees. For anisotropic substrates  $\phi$  is generally not  $45^\circ$ . From simple phase matching conditions, the angle  $\phi$  for a given substrate is [34]

$$\phi = \tan^{-1}\left(\frac{v_x}{v_z}\right) \quad (5.1)$$

where  $v_x$  and  $v_z$  are the velocities along the respective axes of the material. For completeness it has been noted here that the velocities along different axes generally do not have the same temperature coefficients, which adds a further complication to the design of reflective array devices. This however is not of concern here as GaAs is a cubic material, so the velocity along any  $\langle 110 \rangle$  direction is identical. This also simplifies the design of the reflectors as it makes  $\phi = 45^\circ$ .

The reflection of a plane wave of amplitude  $A$  on a single groove has been illustrated in Figure 5.2. The reflection coefficients for an up step  $\Gamma_u$ , a down step  $\Gamma_d$  and the transmission coefficient  $\tau$ , for either step are from [32]

$$\Gamma_u = r - j\frac{\hat{B}}{2} \quad (5.2)$$

$$\Gamma_d = -r - j\frac{\hat{B}}{2} \quad (5.3)$$

$$\tau = 1 - \frac{r^2}{2} - j\frac{\hat{B}}{2} \quad (5.4)$$

where  $r$  has been defined as the impedance discontinuity, which is proportional to the step height:

$$r = C\frac{h}{\lambda}, \quad (5.5)$$

$\hat{B}$  is the energy storage term proportional to  $h^2$  :

$$\frac{\hat{B}}{2} = C'\left(\frac{h}{\lambda}\right)^2, \quad (5.6)$$

$\lambda$  is the acoustic wavelength, and  $C$  and  $C'$  are the first and second order coefficients of mechanical reflection to be determined experimentally.

The reflection coefficient for a groove,  $\Gamma_g$  has been derived by following the path of the wave as illustrated in Figure 5.2 and using equations (5.2), (5.3) and (5.4). When the terms of order  $(h/\lambda)^2$  were neglected, then  $\Gamma_g$  was expressed as [32]

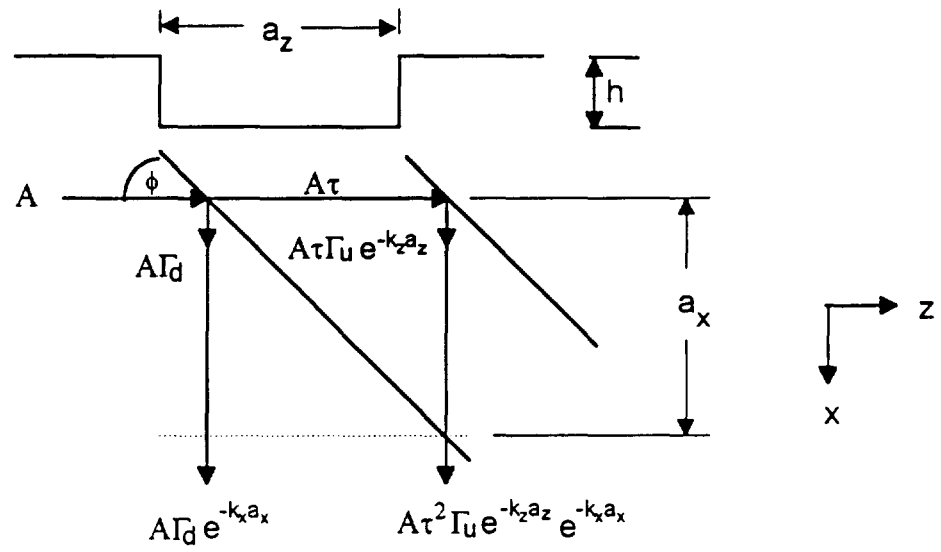
$$\Gamma_g = -2je^{-j\theta}\left(r \sin \theta + \frac{\hat{B}}{2} \cos \theta\right) \quad (5.7)$$

where

$$\theta = \frac{ka_z}{2} + \frac{\hat{B}}{2} \quad (5.8)$$

and  $k$  is the wavenumber in the  $z$  direction.

**Figure 5.2:** Reflection of a SAW from a single groove.



Now in this case  $a_z = \lambda/2$ , so  $\theta$  becomes:

$$\theta = \frac{\pi}{2} + \frac{\hat{B}}{2} \quad (5.9)$$

Now, for the metal thickness under consideration ( $h/\lambda < 0.04$ ), it can be assumed that

$\frac{\hat{B}}{2} \ll \frac{\pi}{2}$ , so  $\theta$  is taken as  $\pi/2$ , making the magnitude of  $\Gamma_g$

$$|\Gamma_g| = 2r \quad (5.10)$$

In the case where  $a_z = \lambda$ , then  $\theta = \pi$ , which leads to

$$|\Gamma_g| = \hat{B} \quad (5.11)$$

Equations (5.10) and (5.11) allow approximate values of  $C$  and  $C'$  to be determined experimentally by using gratings with widths of  $\lambda/2$  and  $\lambda$  respectively. This experiment, conducted for grooves on Y-Z LiNbO<sub>3</sub> by Melngailis and Li [35] showed a significant difference in constants for normal and oblique incidence. Hence, the values theoretically calculated for normal incidence cannot generally be applied to the oblique case, which supports the findings in this thesis.

## Experimental Determination of the Acoustic Impedance Mismatch from Stripes and Grooves on GaAs

### Test Structure

Because the maximum reflection from an oblique grating is attained from  $a_z = \lambda/2$  [31], it was set about to determine the value of the impedance mismatch,  $r$  for both 45 degree grooves and Al stripes on GaAs. A number of devices were designed with as illustrated in Figure 5.3. The test structure consisted of three IDTs and two reflector banks in between. The SAW was launched by the IDT at the upper left. The transmission through the reflector (T31) was measured by the IDT at the right, and the reflection from the pair of reflector banks (T21) was measured by the IDT at the bottom left. An alternative technique would have been to have only one reflector bank and a large IDT rotated 90 degrees on the bottom. However, this structure more closely matches the reflector structure used in the ring oscillator, and provided more useful information in this case. Due to reciprocity, it was assumed that the responses of the gratings were identical, allowing the reflection coefficient of a single reflector bank to be deduced from the measurement.

Ten different test structures were included on mask set AE3. These are documented in Table 5.1 The IDTs on these devices were split finger IDTs with a finger width on 1.5  $\mu\text{m}$ , designed to operate at about 238.5 MHz. The split finger IDT was



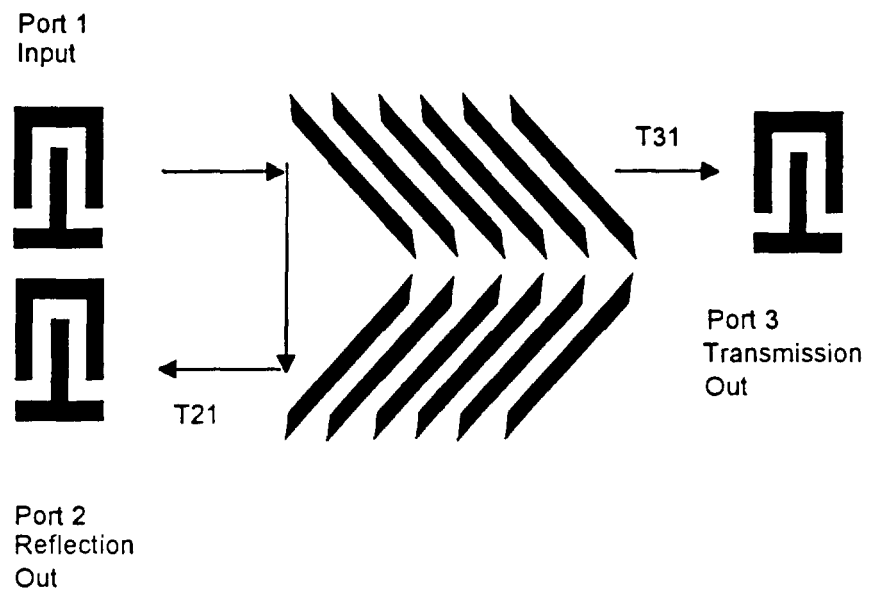


**Figure 5.3:** Reflection test structure.

chosen because it would not interfere with the measurement of the grating. The reflector banks all had a stripe and gap width of  $6\mu\text{m}$  in the direction of propagation, corresponding to  $a_z = \lambda/2$ .

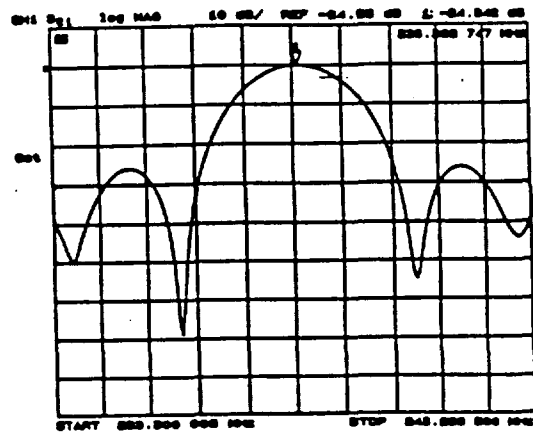
All stripes were inclined  $45^\circ$ . There were two sets of 5 reflectors with lengths varying from 200 to 1000 stripes, one set with open stripes and one set with all the stripes shorted. The IDTs and reflectors were laid out on two different plates, so that the metal thickness of the two structures was independent, and so grooves could be investigated.

#### Experimental Measurements of the Grating Reflection Coefficient for Al Stripes

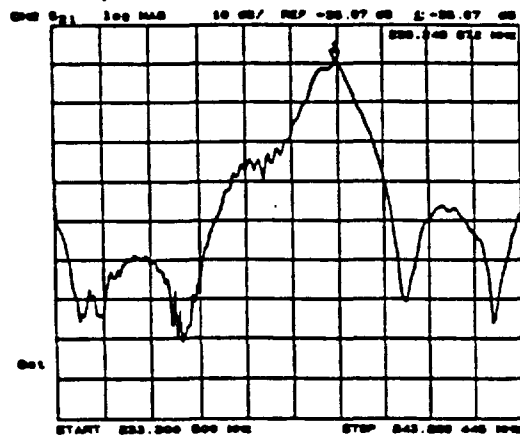
Several wafers of devices were fabricated for this experiment on 2 inch Si {001}-cut,  $\langle 110 \rangle$  propagating GaAs. The first experiment performed by the author was on Al stripes with a  $100 \text{ \AA}$  Cr adhesion layer. Stripes were investigated first as it was hoped that an oscillator device could be simplified by having a single metallization layer for both IDTs and reflectors. Three Al thicknesses were deposited using a filament evaporator. The metal was subsequently measured using the DECTAK 3030 auto profiling system to the nearest  $100 \text{ \AA}$ . In this experiment the thickness of the Cr was neglected as the ratio of Al to Cr is large for all three cases. A sample measurement has been compiled in Figure 5.4, for the transmission T31 without a reflector as a calibration, and T21 and T31 for a 600 stripe shorted reflector with  $3800 \text{ \AA}$  of Al. The IDT-IDT

**Table 5.1** Reflector test structure parameters for Mask AE3

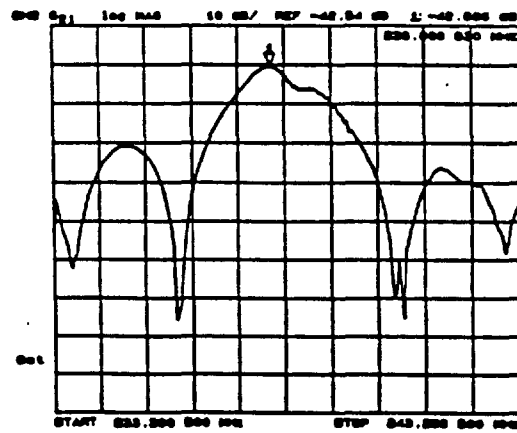
Device	Open/ Short	Number of Stripes	Stripe Width ( $\mu\text{m}$ )	Stripe Spacing ( $\mu\text{m}$ )	Angle
AE301	Short	200	6	6	45
AE302	Short	400	6	6	45
AE303	Short	600	6	6	45
AE304	Short	800	6	6	45
AE305	Short	1000	6	6	45
AE306	Open	200	6	6	45
AE307	Open	400	6	6	45
AE308	Open	600	6	6	45
AE309	Open	800	6	6	45
AE310	Open	1000	6	6	45



(a)



(b)



(c)

Figure 5.4: S21 measurements of (a) IDT-IDT response, (b) T21, (c) T21.

response was a measurement made between two IDTs with no reflectors as a benchmark on each wafer. The other two measurements made by the author were T21 and T31, to evaluate the reflection and transmission coefficients of the grating. The reflection coefficient of a single grating, which was of most interest here, was calculated from the magnitude of the S21 measurement of T21,

$$|\Gamma_{\text{grat}}| = \sqrt{10^{\frac{|T21|}{20}}} \quad (5.12)$$

The author assumed that each grating is identical and contributes equally to the net reflection coefficient.

From the transmission matrix model of Datta [14], the reflection coefficient of a grating, whether slanted or normal was considered, was approximated from the impedance mismatch  $\Delta z/z$  simply as

$$|\Gamma_{\text{grat}}| = \tanh(N_g \frac{\Delta z}{z}) \quad (5.13)$$

where, to equate terminology,  $\Gamma_g$  used here is equivalent to Datta's  $\Delta z/z$  if piezoelectric shorting is ignored.

From (5.13), it was then straightforward to compute an approximation to the reflection coefficient of a single step,  $r$ , from the measured data as

**Table 5.2:** Values of  $|\Gamma_{\text{grat}}|$  calculated for Al stripes from measured data.

$N_{\text{grat}}$	Metal		
	Thickness		
	1,500	3,800	5,800
200 Open	0.42	0.47	0.56
200 Short	0.43	0.46	0.54
400 Open	0.5	0.53	0.65
400 Short	0.48	0.52	0.62
600 Open	0.56	0.56	0.7
600 Short	0.54	0.54	0.71
800 Open	0.56	0.57	0.63
800 Short	0.55	0.54	0.65
1000 Open	0.57	0.42	0.51
1000 Short	0.52	0.41	0.5

$$|r| = \frac{1}{2N_{\text{grat}}} \tanh^{-1} |\Gamma_{\text{grat}}| \quad (5.14)$$

Calculated values  $|\Gamma_{\text{grat}}|$  for each of the devices in the experiment have been compiled in Table 5.2 from the measurement of  $|T_{21}|$ . There are some interesting trends which are observed from the data in this table. First of all, the value of  $|\Gamma_{\text{grat}}|$  generally increases with metal thickness as expected. No conclusive difference was observed between open and shorted stripes as could be expected because of the low value of  $K^2$ . The most interesting trend is the decrease in  $|\Gamma_{\text{grat}}|$  for the long gratings, particularly for the thickest metal. This phenomenon, which is contrary to the expected behavior has been attributed by the author to re-reflections in the grating.

### Multiple Reflections

By examining the paths of triply-reflected waves, it was observed that at the resonant frequency of the grating these waves are  $180^\circ$  out of phase with the singly-reflected waves [34]. In Figure 5.5, which has been borrowed from [30], the effect of triply-reflected waves on the time response of the T21 has been sketched. For the case of only singly-reflected waves, the time response would be a simple rectangular pulse train. The triply-reflected waves produce a triangular shaped pulse train. The net time response, then, is the convolution of the two pulse trains, resulting in a non-rectangular pulse train twice as long as would be expected with no multiple reflections. The principle

effects of the multiple reflections are a narrowing of bandwidth of the frequency response and a decrease in the magnitude of the reflection coefficient of the grating.

The multiple reflections model, explains precisely what was observed in the experimental data for the slanted Al gratings. A time domain response for a 600 stripe grating with an Al thickness of 3800 Å has been plotted in Figure 5.6. As may be seen, the impulse response of T21 follows the behavior just described. This leads to two insights into the design of Al gratings. Longer gratings are not necessarily more efficient and thicker metal does not necessarily produce a higher net reflection coefficient for the grating.

#### Calculation of the First Order Mechanical Reflection Coefficient for Al Stripes

Given the multi-reflections in the longer IDT, only the 200 stripe reflector bank was used in this thesis to approximate a value of  $C$  for Al stripes. Using equation (5.14), the value of  $|r|$  was calculated by the author for the three metal thicknesses for a reflector bank with 200 open stripes. This data is plotted in Figure 5.7 along with a linear approximation which was fitted to the data to approximate the slope of the line. The linear approximation was described by  $0.0009 + 0.014 h/\lambda$ . It was not possible to match a linear curve to the data without the constant term. From the work of Datta [14], this constant has been attributed to the reflection due to piezoelectric shorting. This value was determined by Datta for normal incidence gratings, but no previous value has been reported for oblique incidence gratings. For normal incidence gratings, this value has been



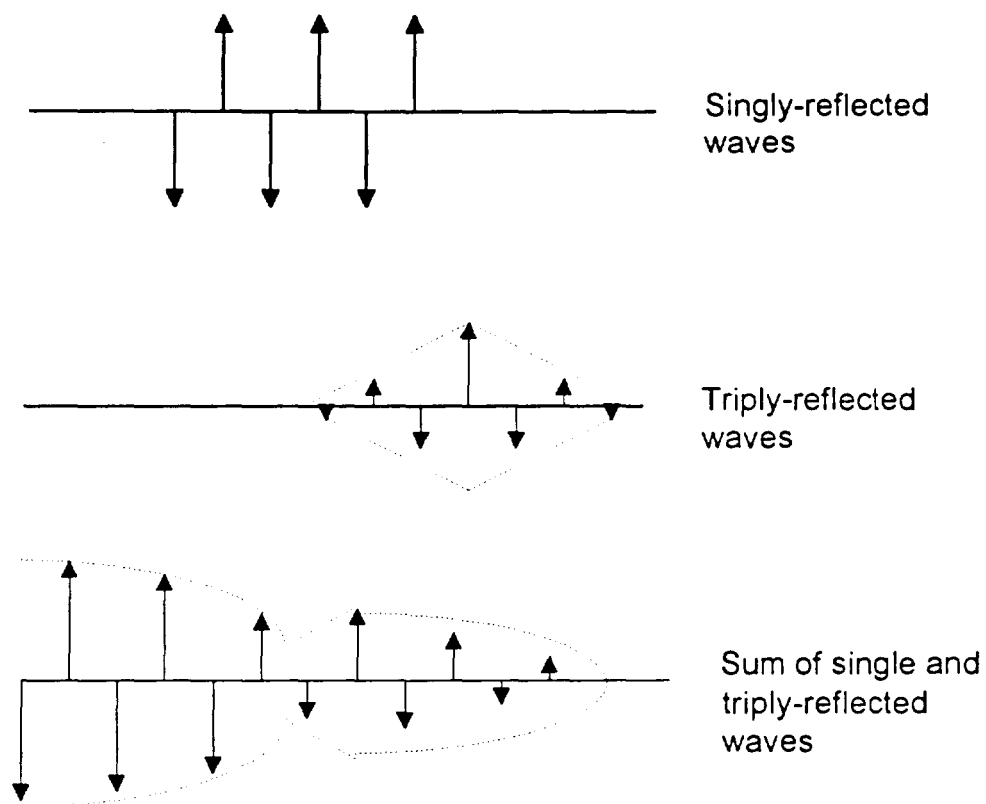


**Figure 5.5:** Sketch of the effects of multiple reflections on the time response of T21.

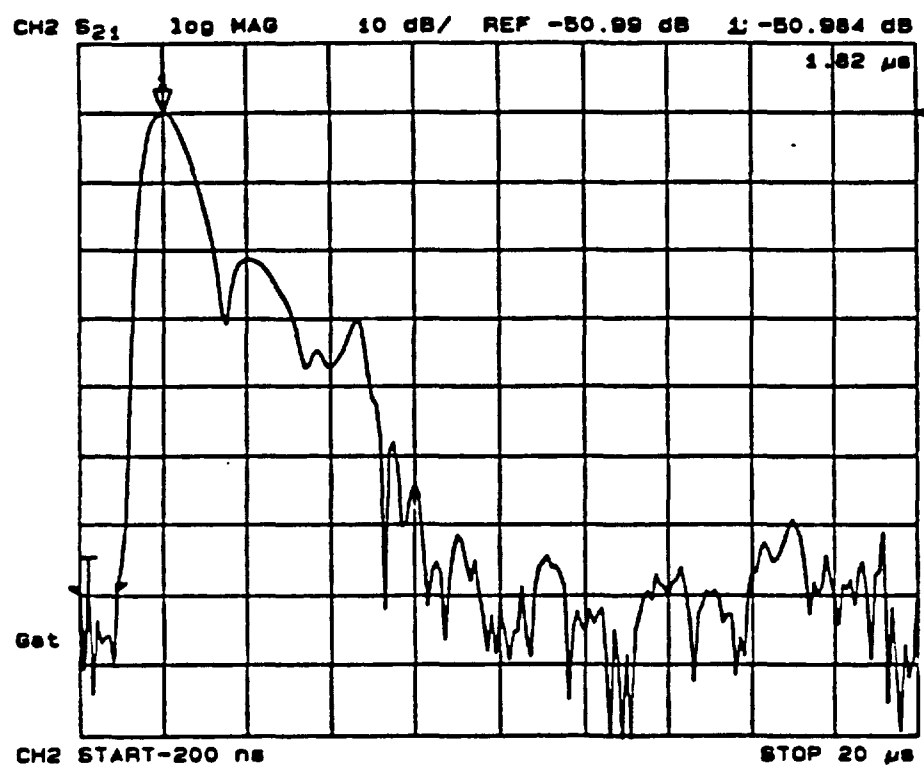


**Figure 5.6** Time response of T21 for a 600 stripe open grating with an Al thickness of 3800 Å.

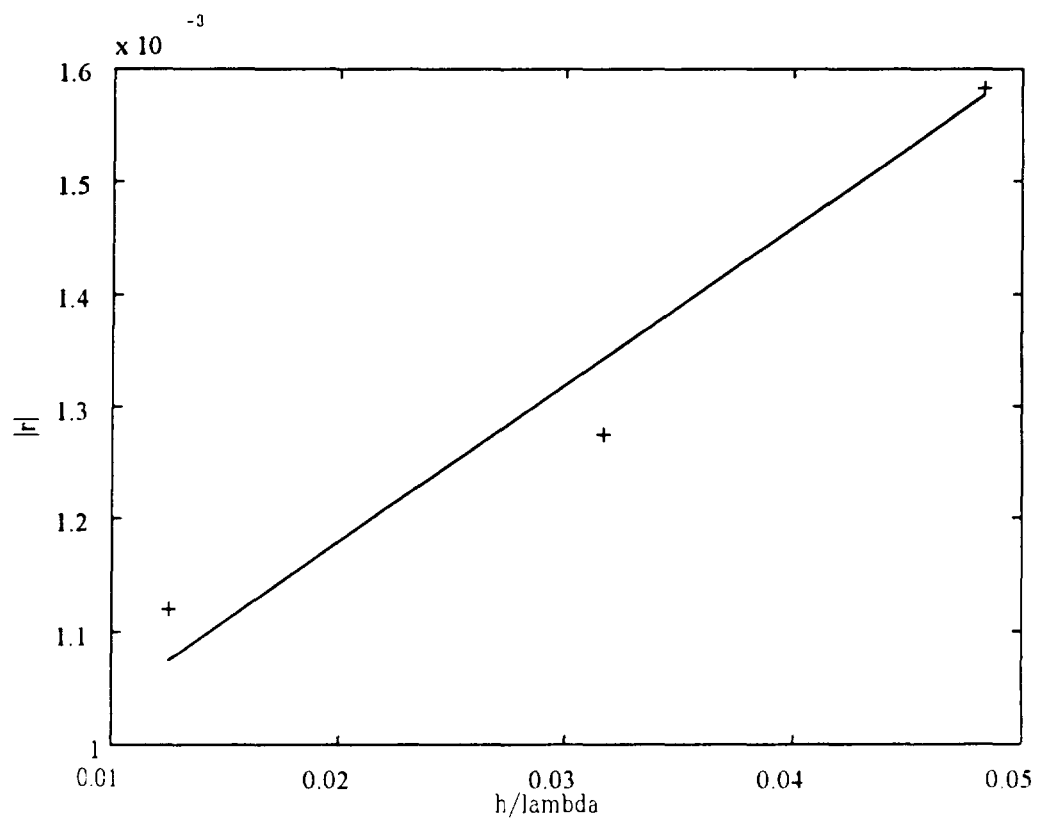


**Figure 5.7:** Reflection coefficient of a single step,  $|r|$ , calculated from measured data for 200 Al stripes versus  $h/\lambda$  (+) and the fit curve used to calculate  $C$  (solid).

calculated as  $-0.7 \cdot K^2/2$ , which calculates to a value of 0.00049. This is on the same order as the constant determined by the author, but no other correlation has been developed here.

The value of  $C$  for shorted Al stripes has been approximated by the author as  $C = 0.014$ , which is a low value compared to that for normal incidence, which from Datta was 0.9. Using this value of  $C=0.014$ , in equation (5.14) it was approximated by the author that a metal thickness of  $4.6 \mu\text{m}$  would be necessary to obtain  $|\Gamma_{\text{grat}}| = 0.99$  for  $N_{\text{grat}} = 200$ . A value of only  $0.34 \mu\text{m}$  was calculated for  $N_{\text{grat}} = 1000$ , but from the experimental data this was obviously not the case, due to the high level of loss caused by the multi-reflections in the grating.

From this exercise, it was concluded by the author that the desired efficiency could not be achieved using a grating with Al stripes. No other metal was considered for further investigation but it is possible that a different metal such as Au or a combination of metals as demonstrated by Hunt for normal incidence gratings [37], could provide better performance, if a greater acoustic impedance mismatch could be achieved. To summarize the performance of Al gratings, the reflection coefficient from single step has been found by the author to be small, which leads to the need for either excessively thick metal layers or very long reflector banks. The necessary Al thickness is not practical for SAW device processing and the high loss introduced by multi-reflections in long gratings makes this an undesirable approach. It was opted instead by the author to investigate grooves.

### Calculation of the First Order Mechanical Reflection Coefficient for Grooves

Similar experiments were conducted by the author on grooves as those previously described for stripes. The sample wafers were processed in the same manner as the wafers used for stripes up to the point where the stripes were patterned with the photoresist. At this point the wafers grooves were etched using the same  $\text{H}_3\text{PO}_4/\text{H}_2\text{O}_2/\text{H}_2\text{O}$  etch as described in Chapter 3 for thinning the epitaxial layer. The etch was performed at room temperature ( $\sim 22^\circ\text{C}$ ). The etch rate was measured by the author to be approximately 800 Å per minute and the only peculiarity of the etch was that patterns with the shorting bar along the edge were reproducible, whereas the open strip patterns etched sporadically and could not be relied on to give a uniformly etched grating. Given the small dimensions of the grooves, the thickness could only be measured in the large busbar region. It was observed using a scanning electron microscope the etch was of uniform depth from the large busbar region into the smaller grooves so that this measurement gave a valid representation of the groove depth. The SEM pictures of the grooves in Figure 5.8 show that the profile of the sidewall was inclined approximately 45 degrees. It may be possible that a different etch could have produced straight sidewalls, but this profile produced a strong reflection coefficient, so no further investigation was performed.

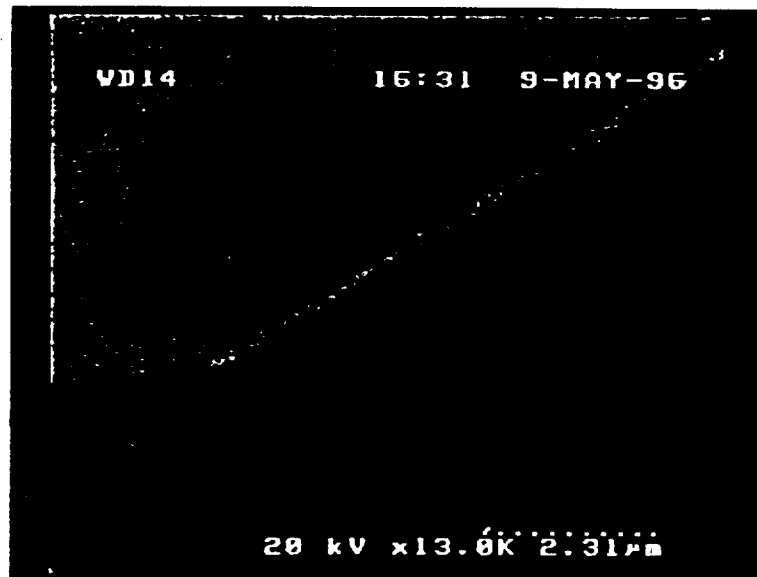
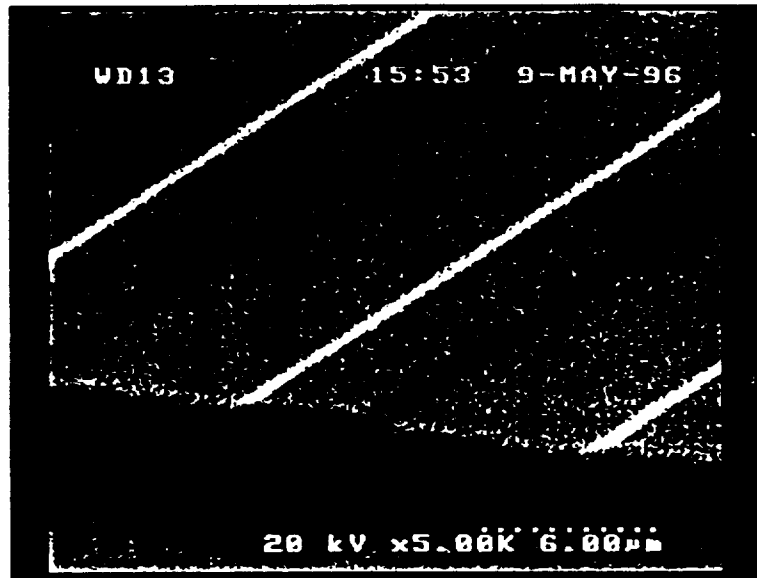


Figure 5.8: SEM photographs of the 4300 Å grooves.

The same measurements and data analysis were performed by the author on the grooves as previously described for the Al stripes. Five samples were fabricated with groove depths ranging from 1000 Å to 4300 Å. The calculated values of  $|\Gamma_{\text{grat}}|$  have been tabulated in Table 5.3. It was immediately obvious from the data that grooves provided a much higher reflection coefficient than did the Al stripes. It was initially concluded by the author, that stripes were less susceptible to the effects of multi-reflections, than were the stripes as the reflection coefficient did not drop off as dramatically for the long grating arrays. However, further analysis contradicted this conclusion, supported by the observation that because of the high reflectivity of the grooves, the wave penetration was much less than in the stripe arrays. Hence, the effects of multi-reflections are not as apparent as in the stripe arrays.

The wave penetration was further investigated by the author using the knife-edge laser probe to establish the effective length of the gratings, in order to calculate the value of  $r$ , from the data. In the Al stripes, this was not an issue, as the reflection coefficient was weak. For the thick grooves, it was necessary to establish an effective length,  $N_{\text{eff}}$  in order to approximate the value of  $|r|$ , as it was found that the SAW did not penetrate the full 200 grooves. The method used by the author was to scan along the direction of propagation with the laser spot centered transversely in the grating. The magnitude of the SAW was measured at several points to establish the penetration depth. The measured data for a 200 groove grating with 4300 Å groove depth has been plotted in Figure 5.9. It was observed from this measurement that the SAW amplitude dropped off quickly, indicative of a strong

**Table 5.3:** Values of  $|\Gamma_{\text{grat}}|$  calculated for grooves from measured data

$N_{\text{grat}}$	Groove Depth (Å)				
	1,000	1,500	2,700	3,700	4,300
200	0.65	0.71	0.86	0.91	0.92
400	0.72	0.78	0.97	0.98	0.95
600	0.72	0.83	0.96	0.97	0.87
800	0.75	0.87	0.95	0.95	0.84
1000	0.76	0.8	0.95	0.93	0.76



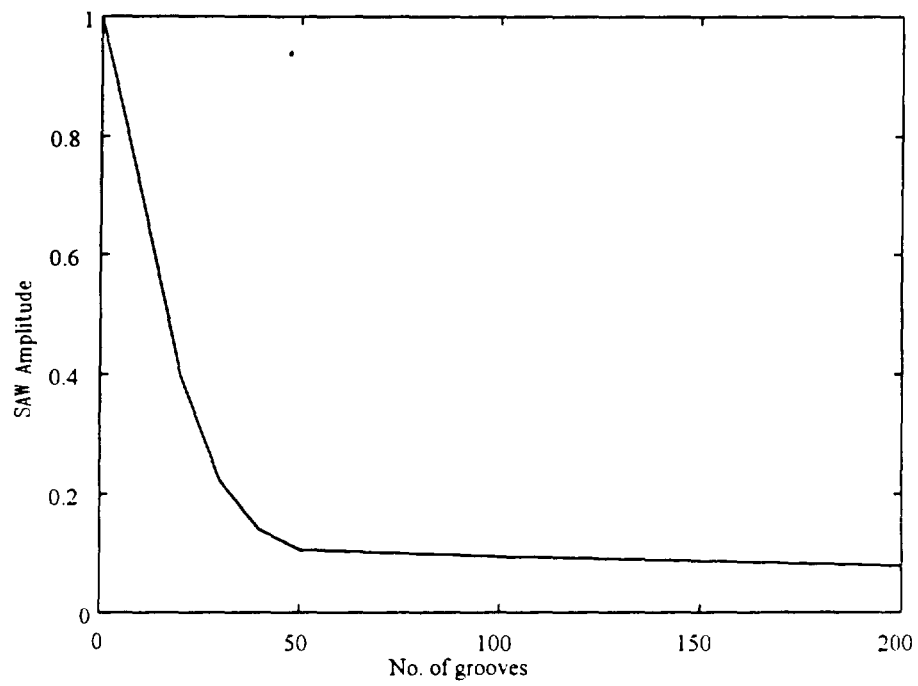


**Figure 5.9:** Normalized SAW amplitude versus depth into the grating as measured using the laser probe.

reflection coefficient. The effective grating length was taken at the point where the amplitude dropped to one tenth of the incident SAW amplitude, which in this case was estimated to be  $N_{\text{eff}} = 70$ .

Using this data, combined with the measured value of  $|\Gamma_{\text{grat}}|$ , the value of  $|r|$  was approximated as before. The experimentally calculated values of  $|r|$  have been plotted against normalized groove depth in Figure 5.10 along with the linear curve fit. In this case, the slope of the curve was approximated at 0.29 and no constant was necessary to obtain a good fit. This supports the earlier hypothesis that the constant was needed to account piezoelectric shorting, which does not exist for unmetallized grooves.

### Summary of Grating Measurements

The thorough examination of both Al stripes and grooves on GaAs by the author unveiled previously unknown information about the behavior of slanted gratings on {100}-cut GaAs. Although it was initially hoped that the Al stripes would have made efficient gratings, this did not turn out to be the case. It was however, discovered by the author that etched grooves provided a strong reflection coefficient. Previously unreported values for mechanical reflection coefficients have been approximated in this thesis from measured data. Although the experiments were affected somewhat by multiple reflections, these constants provide a good first order design rule for the design of slanted gratings on GaAs.

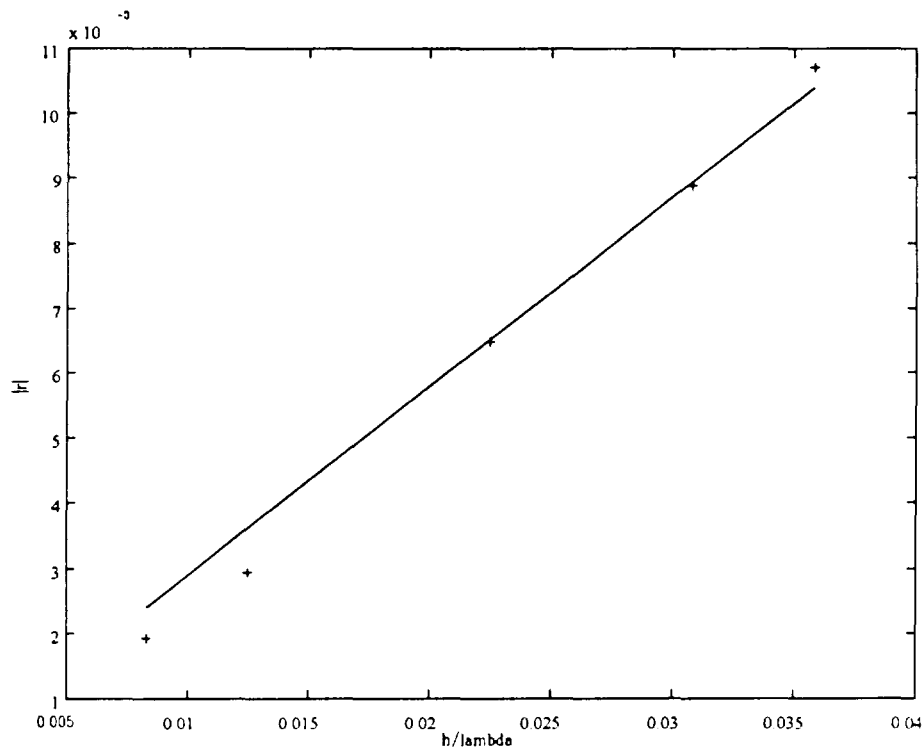


**Figure 5.10:** Reflection coefficient of a single step,  $|r|$ , calculated from measured data for 200 grooves versus  $h/\lambda$  (+) and the fit curve used to calculate  $C$  (solid).

## **CHAPTER 6**

# **INVESTIGATION OF THE INTEGRATED SAW OSCILLATOR**

As discussed in Chapter 1, it was envisioned by the author, that given a SAWAMP and an efficient reflector bank, it would be possible to create a SAW delay line oscillator on a single die. In the preceding chapters, both of these components have been developed and characterized experimentally. In this chapter, the integration of these components into the ring oscillator of Figure 1.1 has been investigated by the author and the requirements for a working device have been identified. The investigation of the oscillator proceeded in two stages. In the first stage, the loop was examined without the SAWAMP to determine the loss around the loop for different gratings. In the second stage an oscillator was tested with the SAWAMP in place to determine the necessary gain for oscillation and if the oscillator could operate given the low gain which was available without an additional piezoelectric layer.

### Investigation of the Loop Delay Line

On the AE3 mask set, some loop delay structures were included for determining the loss around a loop consisting of two IDTs and two pairs of reflector banks as illustrated in Figure 6.1. On each test device there were launching and receiving IDTs between two pairs of reflector gratings. The IDT separation was approximately 3 mm and the distance between reflector banks was 5 mm. Each IDT had 100 split finger pairs and the reflector banks had 500 stripes. Because an IDT is bi-directional, there were two possible paths by which the signal could travel from the input to output IDT, labeled as direct path and double bounce in Figure 6.1. If only the two paths were considered, then it would be expected that two pulses could be observed arriving at the output IDT at different times depending on the delay of the path traveled. In this were a lossless loop, these pulses would pass through the IDTs and continue to circulate so that pairs of pulses would repeat infinitely in time spaced by the delay of the loop. In actual fact, because of the losses in the reflectors and other SAW propagation losses such as diffraction, the amplitude of the pulses should decay over time.

### Experimental Characterization of the Loop

The loss around the loop was measured by the author for each of the Al stripe and grooved samples described in Chapter 5. The loss around the loop was determined using the time domain feature of the HP8753 network analyzer. Figure 6.2 shows the measured

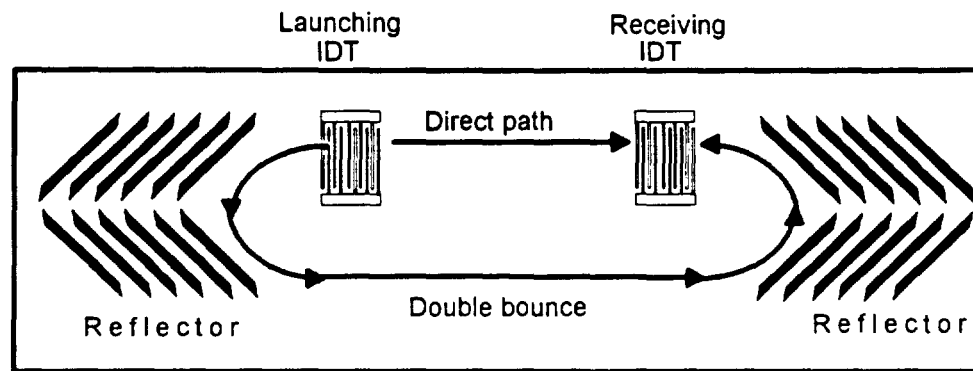


**Figure 6.1:** Schematic illustration of delay line loop with multiple paths between IDTs.

frequency response between the two IDTs for the sample with 4300 Å grooves. Very little information was gathered from this measurement other than there appeared to be a large interfering signal delayed in time from the main path. Transforming this into the time domain yielded much more information about the signals arriving at the output IDT as shown in Figure 6.3. The first pulse arriving was identified by the author as the main path signal between the two IDTs and used as a reference to determine the loss of the subsequent arrivals. The second pulse, which was delayed 2.8  $\mu\text{s}$  from the main path was the double bounce signal. The amplitude difference between these two pulses represents the loss from the reflectors and any associated losses such as diffraction. For this sample the loss was 4.2 dB. The next pulse to arrive was the signal launched by the input IDT, passing through the output IDT, traveling around the loop, back through the main path to the output IDT. It was paired by another pulse from the counter-propagating wave, which was the original double-bounce signal which had completed another full trip around the loop. This pattern was observed to continue out to 40  $\mu\text{s}$ , indicating that a low-loss loop had been created. It was interesting to note that if the reflector loss was the only loss mechanism, the second and third pulses should have been at equal levels. There is an additional loss in the third pulse of 2.3 dB, a small amount, 0.5 dB which was attributed to IDT loading. The rest was attributed to the loss was attributed to the spreading of the beam front outside of the IDT. The comparison between the first and third pulses indicated that a total loop gain of 8 dB would be sufficient to sustain oscillation.

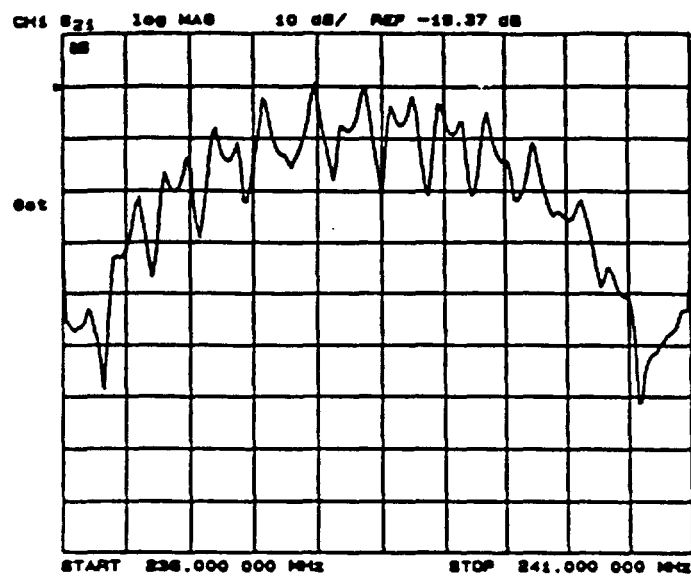


Figure 6.2: Measured frequency response between the two IDTs .

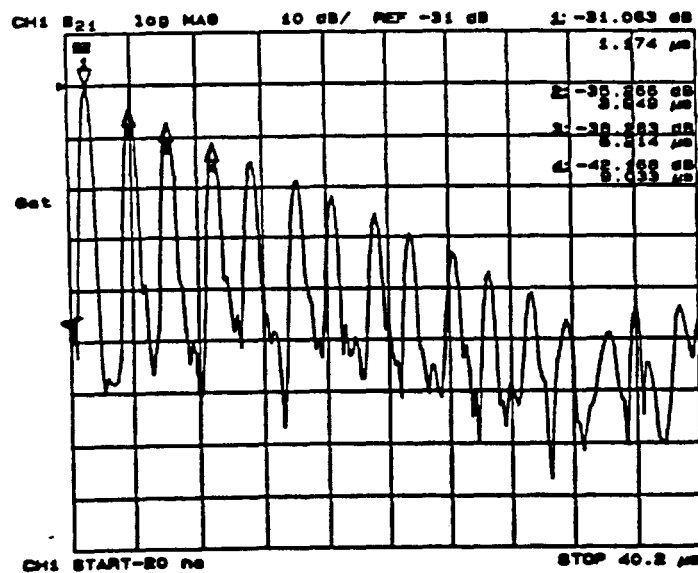
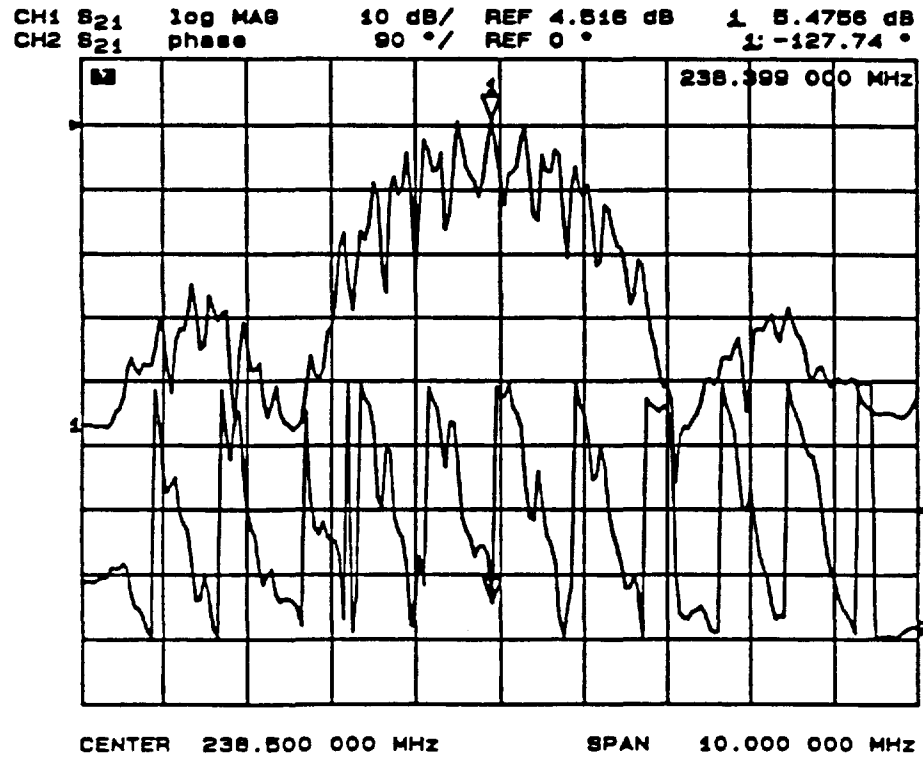


Figure 6.3: Time domain response between the two IDTs



A test was conducted by the author on the loop with external amplifiers to observe the conditions necessary for oscillation. Although this experiment does not directly mimic the integrated oscillator, this was a good approximation, before inserting the SAWAMP. Two MAR-1 amplifiers were placed in series between the output IDT and the network analyzer. The measure magnitude and phase responses are shown in Figure 6.4. It is possible for oscillation to occur at any frequency point where the phase is a multiple of  $2\pi$  and the magnitude is greater than 0 dB. It appeared from this plot that oscillation could possibly occur at several points in the passband. The network analyzer was removed from the loop and the output of the MAR-1 amplifiers was connected to the input IDT as shown in Figure 6.5. An oscillation was measured on the HP8591A spectrum analyzer at 238.1 MHz as plotted in Figure 6.6. The oscillation was clean so long as the excess loop gain was less than 2 dB. When the gain was increased, there was enough gain at other frequencies to maintain an oscillation as shown on Figure 6.7. These frequencies correspond to the peaks in the frequency response where the conditions are favorable for oscillation.

This test provided useful information about the loop oscillator. First, given that interfering waves would exist due to reflections and the non-symmetric gain curve of the SAWAMP, then the oscillation frequency would be controlled by the ripples in the passband of the loop. It was initially thought that the center frequency would be set only by the reflectors, which would necessitate the use of a long reflector bank to achieve a



**Figure 6.4:** Measured frequency response between IDTs with MAR-1 amplifiers in cascade.

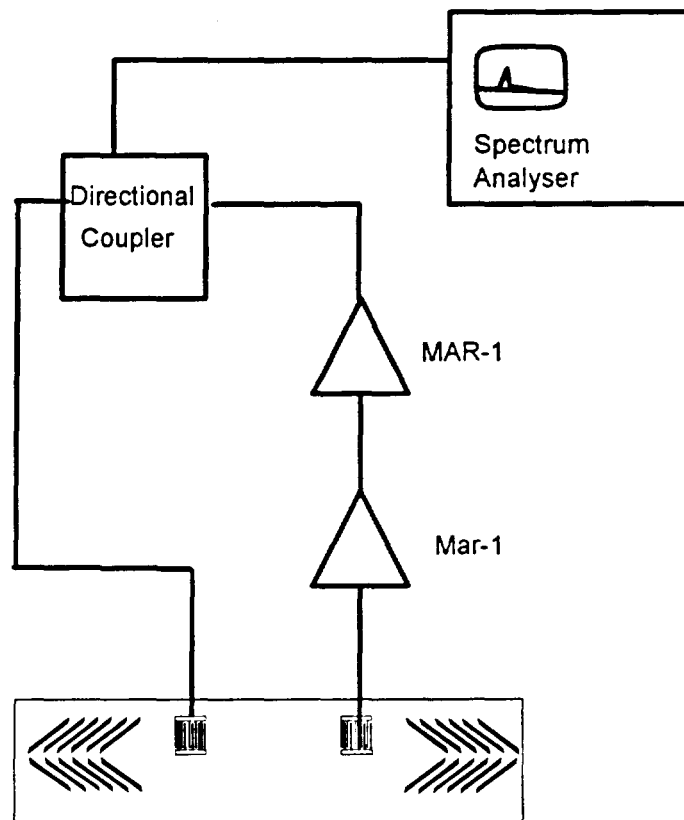


**Figure 6.5:** Oscillator test circuit with external amplifiers.

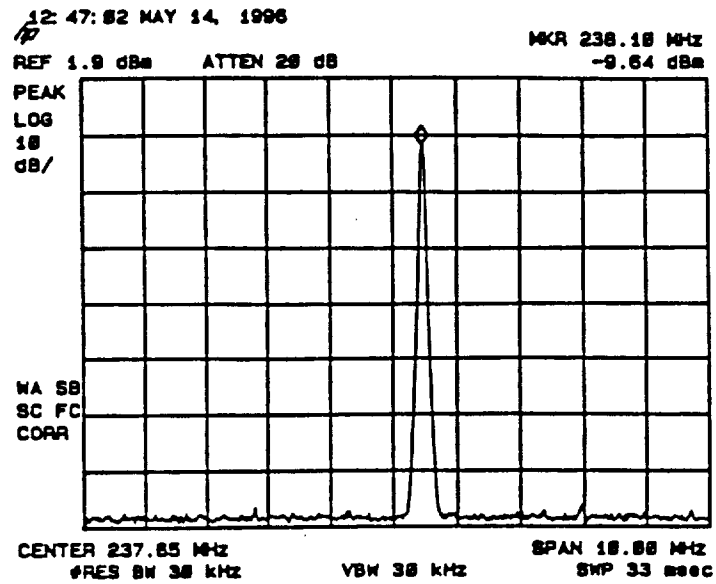


Figure 6.6: Oscillation frequency measured on spectrum analyzer.

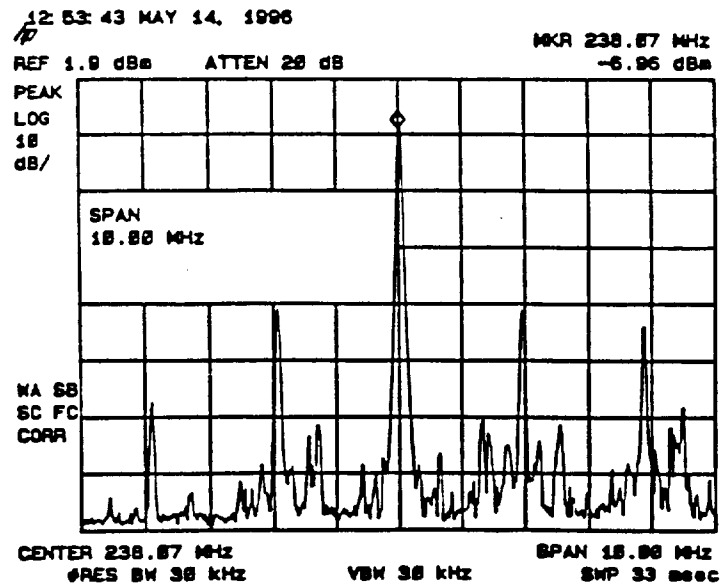


Figure 6.7: Multiple oscillations due to excess gain in the loop.

narrow operating bandwidth. On the contrary, it appeared from this test, that, given a large enough interference pattern in frequency, a controlled oscillation can be maintained as long as the loop gain is not excessive. The frequency of oscillation may then be modified by the loop phase. The disadvantage of this technique is that the frequency of oscillation will hop, rather than change smoothly, because of the ripples in the frequency response.

#### Integration of the SAWAMP into the Loop

A structure was designed in which the SAWAMP was integrated into the loop. In fact, because of the low gain of the SAWAMP on GaAs, two SAWAMPs were designed into the loop as shown in the layout of Figure 6.8. This drawing is taken from EESOF, the layout tool used to design the masks in this thesis. The circuit operation the same as described earlier. There are two 50 split finger IDTs with 400  $\mu\text{m}$  apertures. There were reflector banks on either end and two SAWAMPs, one on each track of the loop to ensure that sufficient gain could be attained. The parameters are listed in Table 6.1. The SAWAMPs were designed to provide the required 8 dB of gain based on predictions from the two-dimensional model. The SAWAMPs were extremely long, but it was the only way to get sufficient gain on GaAs.

Although it is difficult to see in Figure 6.8, the SAWAMPs were placed on a mesa, so that the doped region was confined only to that area of the die.

**Table 6.1:** Ring resonator design parameters

Device	No. of Reflectors	Ohmic Width ( $\mu\text{m}$ )	L1 ( $\mu\text{m}$ )	L2 ( $\mu\text{m}$ )	No. of Segments on Top Track	No. of Segments on Bottom Track
AE426	100	1.5	73.5	7.5	110	160
AE427	100	1.5	121.5	7.5	70	95
AE428	100	6	102	6	85	105
AE429	100	7.5	79.5	7.5	100	125
AE430	100	7.5	127.5	7.5	65	85

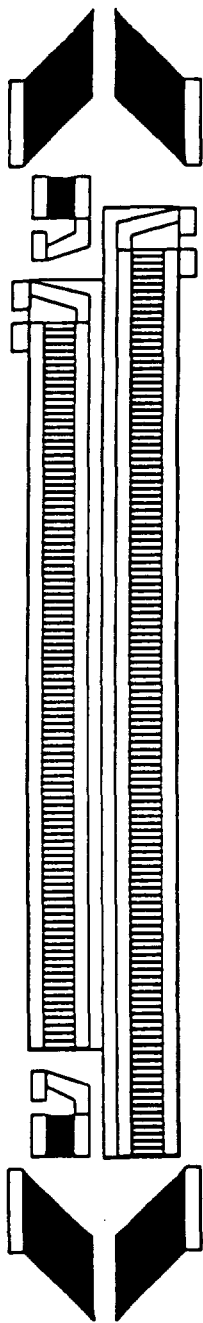


**Figure 6.8:** Ring oscillator layout.

A side view of the structure has been sketched in Figure 6.9. The process was similar to that previously described for the SAWAMPs. The wafer was etched to achieve the desired resistivity. Ohmics were deposited, and annealed, followed by a mesa etch. The mesa etch, which was added in order to minimize the acoustoelectric attenuation outside the SAWAMP region, added complications to the device fabrication, as it was difficult to achieve a good exposure of the  $1.5\text{ }\mu\text{m}$  fingers after the mesa had been etched. After some trial runs, it was determined that a mesa height of approximately  $2000\text{ }\text{\AA}$  was the maximum which could be tolerated to achieve a reasonable yield. This was sufficient to avoid shorting in the IDT region and enabled devices to be fabricated for testing. The reflectors were etched as described earlier as a final step. No problems were encountered with the photolithography because of the wider  $6\text{ }\mu\text{m}$  line widths. On all samples the groove depth was maintained at approximately  $4000\text{ }\text{\AA}$  to ensure a strong reflection coefficient.

Three quarter wafer samples were fabricated. Several devices were yielded and packaged in 14 pin metal DIPs for testing. The response between the two IDTs was measured as for the loop without the SAWAMP. The two SAWAMPs on the top and bottom tracks were controlled independently. The measured time domain response of device AE426 is shown in Figure 6.10. A high insertion loss was measured on all of the samples. Three samples of this device were measured and all were very similar. The first two pulses correspond to the direct path and the double bounce path as before. The



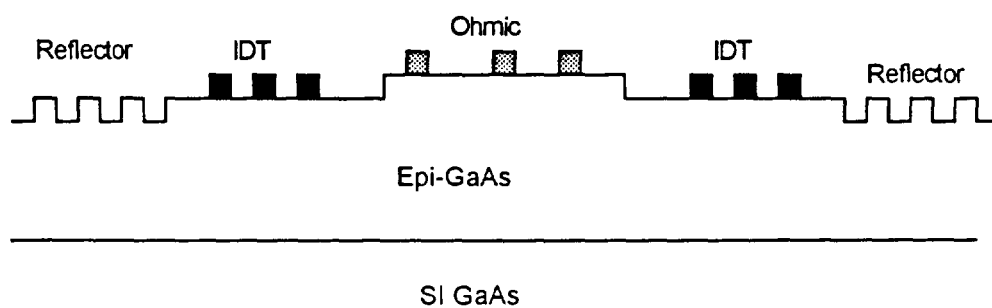


**Figure 6.9:** Profile of ring resonator structure.

difference between these two signals is about 6 dB which indicates that the reflectors are as efficient as before. The difference comes with the second pair of pulses, which in this case were severely attenuated. About 8 dB of loss was expected due to the reflections in the ohmic grating but the loss here turned out to be on the order of 30 dB which was an unexpected turn of events. After further analysis, the obvious explanation for this phenomenon was diffraction. Although the long SAWAMP was the only way to achieve sufficient gain, it was much too long and the wavefront had spread outside of the narrow IDT, which accounted for the excess loss.

The time domain response of the first two pulses of AE430 is shown in Figure 6.11 with the gain from the SAWAMP on the top track overlaid. A greater loss was expected based on the reflection measurements in Chapter 4 for the  $5/8 \lambda$  gratings, but the SAWAMPs displayed the most gain on this device. The gain was observed in the time domain responses of Figure 6.11 and 6.12 for each track. In Figure 6.11, the dashed line was the initial response stored in memory. The solid line is the response of the device with +7V applied to the SAWAMP in the upper track. A maximum gain of approximately 2 dB was measured. It is interesting to observe that the overlap of the two pulses, indicated by the loss measured in the second pulse and varied gain over the length of the first pulse. The same effect was observed by applying 7 V to the bottom track as shown in Figure 6.12. Here, approximately 4 dB of gain was measured, which was expected due to the increased length of the SAWAMP.

From these measurements, it appeared that the integrated oscillator concept was valid, even though no oscillation was demonstrated. An attempt was made to use external amplifiers to aid the internal SAWAMPS, but the extreme loss of the circuit was not conducive to oscillation at the SAW frequency.

### Ring Oscillator Performance Prediction with a ZnO Overlay

Given a ZnO overlay, the diffraction problems experienced here would not be an issue. From the experiments performed by the author, it appears that the distance inside the reflectors should not exceed 5 mm, which is in this case  $400 \lambda$ . This would indicate that a gain of 16 dB/cm would be necessary to achieve oscillation. If some loss due to reflections are taken into account, a total gain of 20 dB/cm would be a reasonable target.

It appears from the author's calculations of Chapter 5 for the ZnO overlay, it would be possible to achieve this ring oscillator using the 5  $\mu\text{m}$  film thickness and a thin charge confinement layer. This would produce an oscillator with an applied voltage of 1.5 V and a power dissipation of on the order of 10 mW. Alternatively, if more gain were required, or if a shorter SAWAMP were desired, the charge layer could be increased to as much as 0.5  $\mu\text{m}$ , by trading off power dissipation with performance. If we consider the 0.5  $\mu\text{m}$  charge layer, approximately 120 dB/cm is possible, so the SAWAMP would be 1.67 mm in length with a power dissipation on the order of 100 mW. The total length of this device could be as small as 3 mm, if 100 grooves were used on each end.

### Summary

The loop delay has been characterized by the author with and without a SAWAMP and the critical issues have been identified which will lead to a working ring oscillator. First of all, it was concluded from the loop measurements that a gain as low as 8 dB could maintain an oscillation in a short loop. In addition, a critical, yet unexpected issue identified by the author was the maximum length of the loop. It appeared that the initial test loop displayed small diffraction related losses, but in the longer loop, this was quite obvious. The loop must be less than 5 mm in length to maintain reasonable diffraction losses. From this exercise it has been concluded that the ring oscillator requires a ZnO overlay to operate, but with the ZnO overlay, the overall length of the device could be as small as 3 mm at the operating frequency of 240 MHz. This represents a size reduction of 2 over the conventional ACT devices presently being investigated by the Microelectronics Group of Georgia Tech at this time. The power reduction predicted by the author is at least an order of magnitude less than conventional ACT devices.

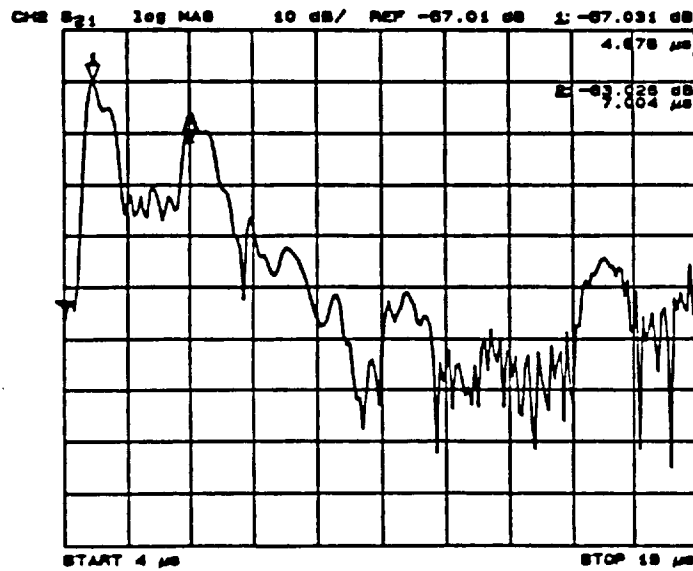


Figure 6.10: Time domain response between the two IDTs of AE426

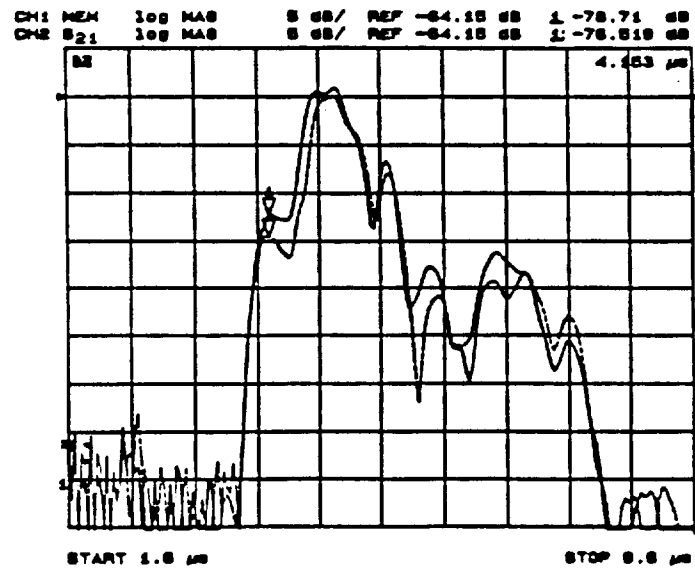


Figure 6.11: Time domain response demonstrating gain on the direct path of AE430

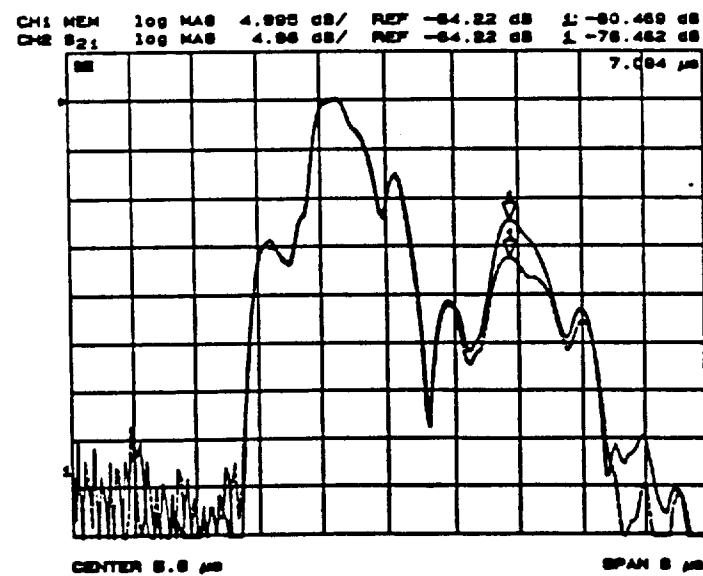


Figure 6.12: Time domain response demonstrating gain on the double bounce of AE430

## **CHAPTER 7**

### **SUMMARY AND CONCLUSION**

In the introduction, the concept of a novel ACT architecture was proposed by the author, which would be instrumental in moving ACT from a laboratory curiosity to a viable technology. Throughout this thesis great strides have been made by the author toward this goal through experimental and theoretical investigation. The main elements of the proposed architecture were a low-voltage, low-power SAWAMP and a efficient bank slanted reflectors. A thorough study of both of these areas by the author has resulted in an in-depth understanding of the aforementioned elements, producing previously unknown data for many aspects of both SAWAMPs and reflectors on GaAs. This was the first such study ever carried out to determine the feasibility of the novel ACT architecture. From this research, the many critical parameters of the components of the ACT device have been identified and a clear path towards a fully functional device has been proposed.

#### Summary of Results

Many contributions toward a deeper understanding of SAWAMPs have resulted from this thesis, both from experimental measurements and theoretical explanations of observed phenomena. The author's original hypothesis that low voltage, low power

SAWAMPs were possible on a GaAs based structure have been verified. A GaAs based material system has been developed by the author, which provided both the required high mobility and high resistivity necessary to achieve a practical device. In addition, the segmented SAWAMP on GaAs was explored both experimentally and theoretically by the author, with and without a ZnO overlay. An order of magnitude improvement in both voltage and power requirements over previously reported devices have been experimentally demonstrated in this thesis. The low voltage requirement was partially due to the small segment lengths used in this thesis, an approach which had not been previously attempted. The reflections due to these small dimensions has been addressed by the author and the reflections have been minimized in this thesis with the proper choice of ohmic dimensions.

A reduction in the gain was experimentally discovered by the author for devices with charge confinement layers less than  $0.5\ \mu\text{m}$ . This effect was theoretically explored by the author, by extending the two-dimensional model of Hsu and White, giving good agreement with the observed phenomenon in the positive voltage direction and improved agreement with data in the reverse direction over the simple model. This two-dimensional model was applied to the case of ZnO overlays to predict the gain for increased  $K^2$ . From these simulations it was conclude by the author, that the peak gain not only depends on  $K^2$  and the width of the charge confinement layer but also the position of the layer with respect to the SAW potential. These simulations predicted that as much as 120 db/cm of gain was attainable for a  $5\ \mu\text{m}$  layer of ZnO. ZnO overlays were experimentally explored,



but process incompatibilities were experienced. However, critical process parameters were identified by the author and it is clear the SAWAMP on ZnO/GaAs can be realized if a process were developed for this device.

The thorough examination of both Al stripes and grooves on GaAs by the author unveiled previously unknown information about the behavior of slanted gratings on {100}-cut GaAs. Although it was initially hoped that the Al stripes would have made efficient gratings, this did not turn out to be the case. It was however, discovered by the author that etched grooves provided a strong reflection coefficient. Previously unreported values for mechanical reflection coefficients have been approximated in this thesis from measured data. Although the experiments were affected somewhat by multiple reflections, these constants provide a good first order design rule for the design of slanted gratings on GaAs. From this study it was approximated that the proposed ACT device could be developed with as few as 100 grooves which greatly reduces the size of the device.

An attempt was made by the author to integrate the SAWAMP and reflectors in a ring oscillator. The loop was tested with and without a SAWAMP in place. The loop characterization with no SAWAMP predicted that as little as 10 dB of internal loop gain would be sufficient to sustain oscillation. It also demonstrated that frequency selectivity could be performed using the ripples in the frequency response due to the interaction of counter-propagating waves, which reduces the need for long narrowband reflectors. A device was attempted with an integrated SAWAMP. Because of the low  $K^2$  of GaAs, the it was necessary to make the device very long. The device turned out to be lossy due to

diffraction. No working ring oscillators were achieved but the critical length of the device has been identified. It was concluded by the author, that given a ZnO overlay a working device could be achieved and parameters have been provided in this thesis which will lead to this end.

### Recommended Future Work

Although the SAWAMP device has for the first time been demonstrated by the author to operate at voltage and power levels conducive to practical application, it remains necessary to increase the  $K^2$  with some type of piezoelectric layer. ZnO was attempted here, but because of the limited resources available, a compatible process was not developed. A device which could be applicable to telecommunications products could be easily attained given the resources to develop a ZnO overlay for this GaAs based structure. There are systems which deposit good quality films at 100 ° C. It is a matter of putting the resource and personnel in place to develop this technology.

Another improvement recommended by the author, over the architecture developed here is the use of an ion implant to define the gain sections of the SAWAMP. Not only would this result in substantial cost reduction over the MBE grown material, but it also simplifies the processing of the device.

Finally it is recommended by the author that a physical study of the interdigitated ohmic contacts be performed to continue the work which has been started in this thesis.

Issues to be addressed, are the balancing of the ohmic process with the ZnO deposition and the effect of ohmic composition on SAW reflections.

## References

- [1] A.R Hutson, J.H. McFee, and D.L. White, "Ultrasonic Amplification in CdS", Phys. Rev. Lett, vol. 7, no.7, 1961, pp. 237-239.
- [2] K. M. Lakin and H.J. Shaw, " Surface Wave Delay Line Amplifiers", IEEE Trans. Microwave Theory Tech., vol. MTT-17, pp. 912-920, Nov. 1969.
- [3] Yu. V., Gulyaev, I.M., Kotelyansky, A.V.Medved, and R.A. Mishkinis, "SAW Monolithic Acoustoelectric Oscillator", Elect. Lett., vol. 16, no. 4, Feb 14, 1980, pp. 114-115.
- [4] R.H. Parmentor, Phys. Rev. 89, 990 (1953).
- [5] J.H. McFee, in: Physical Acoustics, ed. W.P. Mason, vol. IV A, Academic Press, 1966, pp.1-69.
- [6] H. Kuzmany, "Acoustoelectric Interaction in Semiconductors", Phys. Stat. Sol., vol. 25, no. 9, 1974, pp. 9-67.
- [7] R. Adler, "Simple Theory of Acoustic Amplification", IEEE Trans. Sonics and Ultrason.,vol. Su-18, no.3, July 1971, pp115-118.
- [8] J.Henaff, M. Le Contellac, and C. Rudelle, "Amplification of Elastic Surface Waves", L'Echo des Recherches, Special Issue June 1975, pp 72-83.
- [9] T. Grudkowski, "Carrier Concentration Controlled Surface Acoustic Wave Variable Delay Lines", US Patent 4,233,573, Nov. 11, 1980.
- [10] G. Kino, "Acoustoelectric Interactions in Acoustic-Surface-Wave Devices", Proc. IEEE, vol. 64, no. 5, May 1976, pp. 724-748.
- [11] L.A. Coldren and G.S. Kino, "The InSb on a Piezoelectric Rayleigh Wave Amplifier", IEEE. Trans. Electron. Devices, vol. ED-21, pp. 421-427, July 1974.
- [12] E. Yablonovitch, D.M. Hwang, T.J. Gmitter, L.T. Florez and J.P. Harbison, "Van der Waals Bonding of GaAs Epitaxial Liftoff Films onto Arbitrary Substrates", Appl. Phys. Lett., vol. 56, no. 24., 11 June 1990.

- [13] U. Tarakci and R.M. White, "Layered Media Active Microwave Acoustic Delay Lines", Proc. 1972 IEEE Ultrasonics Symp., Boston Mass. 1972, pp. 440-445.
- [14] S. Datta, Surface Acoustic Wave Devices, Prentice-Hall, Englewood Cliffs, N.J., 1986, p. 184.
- [15] Y.V. Gulyaev, S.N. Invanov, I.M. Kotelyanskiy and G.D. Mansfeld, "The Possibility of Building an Electro-Acoustic Amplifier Employing a GaAs n-n<sup>+</sup> Epitaxial Structure", Radio Engineering and Electronic Physics, vol. 22 no. 4, April 1977, pp 105 - 108.
- [16] A.Y. Cho and J.R. Arthur, "Molecular Beam Epitaxy", Prog. in Solid State Chem., vol. 10, part 3, pp 157-191, Pergamon Press, 1975.
- [17] Copyright I.B.M Corp.
- [18] C. W. Turner, A. Shomon and R.M. White, "Reduced-Voltage Operation of a Surface -Elastic-Wave Amplifier", Electronic Letters, vol 5 , pp. 244-245, May 1969.
- [19] G. Cambon, C. Roustan and M. Rouzeyre, "Segmented Surface-Wave Amplifier Exhibiting Gain at 86 MHz", Appl. Phys. Lett., vol. 21, no. 11, pp. 525-527, Dec. 1972.
- [20] S.V. Boritiko, Yu.V. Gulyaev, and G.D. Mansfel'd, "Acousto-Electronic Interaction in Piezoelectric-Semiconductor Film Layered Structure with a Periodic Array of Contacts", Sov. Journ. of Comm. Tech. and Elec. vol. 30, no. 3, March 1984, pp 51-56.
- [21] T.W. Grudkowski, G.K. Montress, M. Gilden and J.F. Black, "Integrated Circuit Compatible Surface Acoustic Wave Devices on Gallium Arsenide", IEEE Trans on Micro. Th. and Tech, Vol 29, 1981, pp 1348-1356.
- [22] P. Gueret, "Simple Theory of Acoustic Surface-Wave Amplification Using Very Thin Semiconductor Layers", J. Appl. Phys., vol. 42, no. 8, July 1971, pp 3040-3042.
- [23] T. H. Hsu and R.M. White, "Two-Dimensional Layered Analysis of a Surface Elastic Wave Amplifier Having a Segmented Drift Structure", IEEE Trans. Sonics and Ultrason., vol. SU-20, no. 1, Jan. 1973, pp 2-6.
- [24] S.G. Joshi and R.M. White, "Excitation and Detection of Surface Elastic Waves in Piezoelectric Crystals", J. Acoust. Soc. Amer. ,vol. 46, pp. 17- 27, July 1969.

- [25] S Datta and B.J. Hunsinger, "Analysis of Surface Waves using Orthogonal Functions", J. Appl. Phys., vol. 49, no. 2, Feb 1978, pp 475-479.
- [26] Y. Kim and W.D. Hunt, "Acoustic Fields and Velocities for Surface-Acoustic-Wave Propagation in Multilayered Structures: An Extension of the Laguerre Polynomial Approach", J. Appl. Phys. vol. 68, no. 15, Nov. 1990, pp 4993-4997.
- [27] S. T. Hsu, "Effects of a Nonuniform Electric Field on Ultrasonic Amplifications in Solids", IEEE Trans. Sonics and Ultrason., vol. SU-20, no. 1, Jan. 1973, pp 6-8.
- [28] I. Uchida, T. Ishigoro, Y. Iwasaki, and T. Suzuki, "Effects of Trapping of Free Carriers in CdS Ultrasonic Amplifiers", Japan J. Phys. Soc., vol.19, pp674-680, May 1964.
- [29] D.L. White, Proc. 4th Intern. Congr. Acoustics, Copenhagen, 1962.
- [30] F. Hickernell, "Piezoelectric Thin-Film Materials", Proc. Int Symp. SAW Devices for Mobile. Comm., 1992, pp-31-38.
- [31] K. Yamanouchi and F. Kadosawa, "An Electroacoustic Surface-Wave Convolver Fabricated From a Thin Piezoelectric Film and a Semiconductor", Elec. Comm. Jap., Part 2, vol.75, no. 12, 1992.
- [32] J. Melngailis, R.C. Williamson, J. Holtham and R.C. Li, "Design of Reflective-Array Surface Wave Devices", Wave Elec., vol 2, 1976, pp 177-198.
- [34] E. Danicki and W.D. Hunt, "On Spurious Bulk Wave Excitation in SAW Grating Reflectors on GaAs (001) (110)", Arch. Acoust., vol. 20, no. 2, 1995, pp 171-175.
- [34] D. Morgan, "Surface Acoustic Wave Devices for Signal Processing", Elsevier, Oxford, 1985.
- [35] J Melngailis and R.C. Li, "Measurement of Impedance Mismatch and Stored Energy for Right-Angle reflection of Rayleigh Waves from Grooves on Y Cut LiNbO<sub>3</sub>", Proc. 1975 IEEE Ultrason. Symp, pp 426-429.
- [36] R.C. Williams, "Reflection-grating devices", Chapter 9 in Surface Wave Devices, H.E. Matthews, Ed., J. Wiley.
- [37] W.D. Hunt, "Propagation of leaky Waves in Free Surfaces and Grating Structures on {100}-Cut Gallium Arsenide", PhD Dissertation, Univ. of Illinois, Urbana, 1987.

## VITA

Thomas Cameron was born on [REDACTED] in [REDACTED]. He received the Bachelor of Science degree with first class honors from Wilfrid Laurier University in Waterloo, Ontario in 1984 and the Masters on Engineering degree from Carleton University in Ottawa, Ontario in 1988. He was employed by Bell-Northern Research (BNR) in Ottawa, Ontario in 1986 as a member of the scientific staff in the Radio Systems Development Group where he was involved in the design modems for Terrestrial Microwave Radio Systems, in particular, the research and design of surface acoustic wave (devices). In 1993, Mr. Cameron was awarded a BNR bursary to pursue his doctorate in Electrical Engineering at the Georgia Institute of Technology. As a Ph.D. candidate, he was a member of the Microelectronic Acoustics Group, and his research was concerned with surface acoustic wave amplification on gallium arsenide. Mr. Cameron has authored a journal paper, and 8 conference papers, including an invited paper at the IEEE 1993 Ultrasonics Symposium in Baltimore, Maryland. In addition he is co-inventor on 3 patents.

